UNIVERSITÀ DEGLI STUDI DI PADOVA

Dipartimento di Ingegneria Industriale DII

Corso di Laurea Magistrale in Ingegneria dell'Energia Elettrica

Design of a five-phase multilayer winding motor drive for a fault-tolerant test bench environment

Relatore
Nicola Bianchi

Co-relatore
Michael Mangles

Studente
Lorenzo Lovato
2061940

Anno Accademico 2023/2024

Contents

List of Figures **III**

List of Tables **V**

1 Introduction **3**
- 1.1 Thesis objective . . . 3
- 1.2 Thesis structure . . . 4

2 Multiphase machines **5**
- 2.1 Types of multiphase machines . . . 5
- 2.2 Advantages and disadvantages of multiphase machines . . . 6
- 2.3 Selection of the number of phase . . . 8

3 Theoretical background **9**
- 3.1 Theory of Fractional slots concentrated winding . . . 9
  - 3.1.1 Analysis of MMF distribution in FSCW Stators . . . 10
  - 3.1.2 Winding factor . . . 13
  - 3.1.3 Single-layer winding . . . 15
  - 3.1.4 Double-layer winding . . . 17
  - 3.1.5 Four-layer winding . . . 19
  - 3.1.6 Winding feasibility . . . 20
  - 3.1.7 Cogging torque . . . 21
- 3.2 Optimal slot-pole number combination . . . 22
  - 3.2.1 Winding Performance Index . . . 22

4 Design **27**
- 4.1 Idealized electric machine . . . 27
  - 4.1.1 Electromagnetic force density . . . 28
  - 4.1.2 Electromagnetic torque . . . 29
- 4.2 Design specifications . . . 30
  - 4.2.1 Preliminary calculations . . . 30
  - 4.2.2 Considerations on the permanent magnet . . . 30
  - 4.2.3 Sizing estimation . . . 33
  - 4.2.4 Stator design . . . 34
  - 4.2.5 Concentrated winding design . . . 37

5 Modeling and control **39**
- 5.1 Modeling . . . 39
- 5.2 Five-phase machine modeling . . . 40
  - 5.2.1 Transformation . . . 42

5.3 Fault modeling 45
5.3.1 One-phase open-circuit fault 46
5.3.2 Open-circuit fault of two nonadjacent phases 48
5.3.3 Open-circuit fault of two adjacent phases 50
5.4 Control 52
5.4.1 Third harmonic injection 52

6 Simulation **55**
6.1 Simulation steps 55
6.1.1 Computation on the solved structure 57
6.1.2 No load simulation 60
6.1.3 Harmonic content in the air gap 64
6.1.4 Mapping 67
6.1.5 Results under MTPA 68
6.1.6 Results under THI 69
6.1.7 Results under faulty conditions 71
6.2 Losses 72
6.2.1 Copper losses 72
6.2.2 Core losses 74
6.2.3 Core loss data 76
6.2.4 Total losses and performances 79

7 Conclusion **81**
7.1 Possible further development 82

8 Acknowledgements **83**

A Appendix **i**
A.1 Fractional slot concentrated winding factor i
A.1.1 Winding factor table for three-phase winding system i
A.1.2 Winding factor table for five-phase winding system ii
A.1.3 Winding factor table for seven-phase winding system iii
A.2 Sintered neodymium magnets v

Bibliography **vii**

List of Figures

3.1 MMF distribution of a single coil. . . . 11
3.2 MMF distribution of a coil pair with same polarity 12
3.3 MMF distribution of a coil pair with opposite polarity. . . . 13
3.4 Analytical distribution of MMF for a 20-slots, 18-poles, 4-layer, five-phase machine 14
3.5 Star of slot of a 3-phase, 9 slots and 8 poles winding with a double-layer. . . 14
3.6 Star of slot for 20-slot 4-pole, five-phase machine 15
3.7 Star of slot for 12-slot 10-pole, three-phase machine 17
3.8 20-slot 18-pole, 2-layer winding, five-phase machine 19
3.9 20-slot 18-pole, 4-layer winding, five-phase machine 20
3.10 Winding layout, 20-slot 18-pole, 4-layer winding, five-phase machine 21
3.11 Flux density distribution 23
3.12 Comparison of single-layer (1L), double-layer (2L) and four-layer winding (4L) for 20-slots, 18-poles, five-phase machine 25

4.1 20-slot 18-pole, 4-layer winding, five-phase machine 27
4.2 Flux density ratio $B_\mathrm{g}/B_\mathrm{rem}$ as a function of the magnet width $t_\mathrm{m}/(\mu_\mathrm{rec} g'')$ . . 32
4.3 Slot of FSCW machine 36

5.1 Simplified five-phase machine model 40
5.2 $\alpha - \beta$ and $\mathrm{d} - \mathrm{q}$ reference frame 42
5.3 Current in healthy case 44
5.4 Fault types in a five-phase drive [20] 45
5.5 Open-circuit fault in phase-a 46
5.6 Open-circuit fault in phase-a 48
5.7 Open-circuit fault in phase-b and phase-e 49
5.8 Open-circuit fault in phase-b and phase-e 50
5.9 Open-circuit fault in phase-c and phase-d 50
5.10 Open-circuit fault in phase-c and phase-d 51
5.11 Current under THI rms mode 53
5.12 Current under THI peak mode 53

6.1 Motor geometry 56
6.2 Mesh density 57
6.3 *B-H* curve *M-19 Steel* 60
6.4 No load simulation flux lines for different five-phase machines 61
6.5 No load simulation results 62
6.6 No load simulation results 62
6.7 No load simulation results 62
6.8 No load simulation results 63
6.9 Stator flux lines for different five-phase machines under 1st harmonic 63

6.10 Stator flux lines for different five-phase machines under 3rd harmonic 64
6.11 Harmonic content in the air gap, 1st harmonic current 64
6.12 No load simulation results, 1st harmonic current 65
6.13 No load analytical results, 3rd harmonic current 65
6.14 No load simulation results, 3rd harmonic current 65
6.15 No load analytical results, 3rd harmonic current 66
6.16 No load simulation results, 3rd harmonic current 66
6.17 Mapping of the Torque 67
6.18 MTPA simulation flux lines for different five-phase machines 68
6.19 MTPA simulation results 68
6.20 Torque of FSCW machine with different number of layers 69
6.21 Torque under THI 70
6.22 Torque under healthy and faulty cases 71
6.23 Rotating losses as a function of the mechanical speed 79
6.24 Total losses comparison 79
6.25 Rotating losses as a function of the mechanical speed 80

List of Tables

2.1 Reduction in stator Joule loss by increasing the number of phases m 8

3.1 Optimal slot/pole combination for 5-phase 4-layer winding 24

4.1 Design specifications 30
4.2 Permanent magnet specification 31
4.3 Dimensions of the slot 36
4.4 Variables summary for FSCW 20-slot 18-pole, five-phase motor 37
4.5 Variables summary for concentrated winding 20-slot 4-pole, five-phase motor 38

6.1 Comparison of torque and torque ripple results with different winding configurations 69
6.2 Torque comparison under THI 71
6.3 Torque comparison under faulty conditions 72

A.1 Winding factor $k_{w,p}$ for three-phase with double-layer i
A.2 Winding factor $k_{w,p}$ for three-phase with 4-layer i
A.3 Winding factor $k_{w,p}$ for five-phase with double-layer ii
A.4 Winding factor $k_{w,3p}$ for five-phase with double-layer ii
A.5 Winding factor $k_{w,p}$ for five-phase with 4-layer ii
A.6 Winding factor $k_{w,3p}$ for five-phase with 4-layer ii
A.7 Winding factor $k_{w,p}$ for seven-phase with double-layer iii
A.8 Winding factor $k_{w,3p}$ for seven-phase with double-layer iii
A.9 Winding factor $k_{w,5p}$ for seven-phase with double-layer iii
A.10 Winding factor $k_{w,p}$ for seven-phase with 4-layer iii
A.11 Winding factor $k_{w,3p}$ for seven-phase with 4-layer iv
A.12 Winding factor $k_{w,5p}$ for seven-phase with 4-layer iv

Abstract

La tesi si focalizza sul progetto e sull'analisi di un motore sincrono a magneti permanenti (PM) a cinque fasi, caratterizzato da 20 cave e 18 poli. Nel design del motor è stata utilizzata una configurazione ad avvolgimento concentrato a cave frazionarie (FSCW) con quattro strati, al fine di mitigare le armoniche indesiderate della forza magnetomotrice (MMF) e ottenere un motore con bassa oscillazione di coppia ($\Delta\tau = 1.31\%$).

Il focus principale della tesi è la progettazione di un motore adatto per applicazioni *fault-tolerant*. Sono stati studiati tre tipi distinti di guasti - circuito aperto di una fase, circuito aperto di due fasi non adiacenti e circuito aperto di due fasi adiacenti - attraverso simulazioni e analisi. I risultati sperimentali rivelano un deterioramento delle prestazioni del motore all'aumentare della gravità del guasto, come ad esempio un significativo incremento dell'oscillazione di coppia dovuta all'assenza di una o più fasi. Nonostante il deterioramento delle prestazioni, il motore dimostra di poter funzionare continuamente in condizioni di guasto. Tuttavia, sono necessari miglioramenti significativi sia nel design che nelle strategie di controllo per ulteriori miglioramenti delle prestazioni.

La ricerca esamina anche le prestazioni del motore sotto l'iniezione di terza armonica di corrente (THI) e analizza gli impatti dei vari scenari di guasto. I risultati mostrano un aumento della coppia del $+0.6\%$ per la modalità rms e del $+15.2\%$ in modalità picco con THI. Tuttavia, l'aumento della coppia è bilanciato da un aumento del $+15.9\%$ nelle perdite joule. Il confronto con un motore ad avvolgimento concentrato con 20 cave, 4 poli e cinque fasi rivela una prestazione superiore del motore FSCW in condizioni nominali, con una coppia media più elevata e una minore oscillazione di coppia. Tuttavia, il motore ad avvolgimento concentrato possiede prestazioni migliori del motore FSCW in funzionamento con THI.

In generale, anche se l'avvolgimento concentrato offre una migliore prestazione con THI, l'aumento della coppia ottenibile non è sostanziale. Pertanto, il FSCW emerge come una soluzione valida per applicazioni multifase e *fault-tolerant*, con una densità di coppia superiore a quattro volte quella della macchina con avvolgimento concentrato.

1 Introduction

Electric motors play a pivotal role across diverse domains, including industrial, commercial, and residential sectors, by efficiently converting electrical energy into mechanical power through electromagnetic field interactions. Within the realm of electric motors, a diverse range of types and configurations exits in order to meet the specific needs and performance demands. Common types of electric motors include both DC motors, divided into brushed and brushless variants, and AC motors, which include induction and synchronous motors, with synchronous motors incorporating externally excited configurations or non-excited configurations, such as permanent magnet or reluctance motor.

Traditionally, AC motors have been categorized based on the number of phases, with single-phase and three-phase configurations being prevalent. However, the widespread adoption of power electronic converters has elevated three-phase AC motors as the predominant solution for variable-speed applications. Nonetheless, in the last decades the potential of multiphase machines has emerged as a promising alternative [34].

Multiphase motors represent a significant advancement in electric motor technology, offering enhanced performance and versatility compared to traditional single-phase or three-phase motors. These motors utilize more than three phases of electrical power, enabling to achieve superior performance compared to their single-phase or three-phase counterparts. Their ability to distribute power across multiple phases allows for smoother operation, reduced harmonic content, and improved control, making them well-suited for a wide range of applications, including aerospace, automotive, renewable energy, and industrial automation [7, 15].

In recent years, advancements in semiconductor technology, control algorithms, and motor design have further bolstered the performance and applicability of multiphase motors. These advancements have enabled multiphase motors to deliver higher torque output, smoother operation, and superior fault tolerance, making them an attractive choice for demanding applications where reliability and performance are crucial [20].

1.1 Thesis objective

The objective of this thesis is to design, analyze, and simulate a multiphase motor for a fault-tolerant test bench. Specifically, the primary aim is to assess the fault-tolerant capability of the motor under three different scenarios: one-phase open-circuit fault, open-circuit fault of two nonadjacent phases and open circuit of two adjacent phases. To achieve the primary objective of the thesis, an exhaustive analysis of various motor typologies is conducted, encompassing considerations such as the number of phases and winding configuration.

In addition, to ensure an effective and simple control strategy, the machine modeling for each of these fault scenarios has to be carried out.

Furthermore, the thesis aims to simulate and validate torque enhancement through third harmonic injection. A significant emphasis is also placed on comparing different types of machine windings in order to evaluate their respective performances. This comparative analysis, conducted using specialized electromagnetic simulation software, aims to determine which winding configuration offers superior performance in terms of efficiency, torque, and fault tolerance.

1.2 Thesis structure

The thesis is organized into several distinct sections, each focusing on a specific aspect of the motor analysis.

Initially, the thesis provides an introduction to multiphase machines, offering an in-depth exploration of their advantages, drawbacks, and diverse topologies.

Following this introduction, the thesis undertakes a rigorous investigation into the fundamental theoretical aspects of a specific type of machine, namely the fractional slot concentrated winding machine (FSCW). Subsequently, it delves into the analysis and formulation of optimization criteria during the pre-design process, aiming to maximize performance and efficiency.

After establishing the theoretical background, the machine modeling is carried out, wherein a mathematical approach is utilised in order to construct an accurate representations of the motor. The objective of the machine modeling is to enable a robust control strategy that can effectively manage the machine's operation, including fault conditions, while also ensuring simplicity of implementation.

Subsequently, the thesis advances to the development of the machine's design. Utilizing representative empirical formulas that capture internal phenomena, it conducts an approximate preliminary sizing of the machine.

Finally, the thesis culminates with the simulation and analysis of results, where the efficacy and validity of the proposed solutions are rigorously evaluated, including comparisons with theoretical results.

2 Multiphase machines

The origins of multiphase variable-speed drives can be traced back to the late 1960s, with the introduction of inverter-fed AC drives. At that time, the operation of three-phase inverters in a six-step mode led to the challenge of low-frequency torque ripple. Therefore, increasing the number of machine phases emerged as a viable solution to mitigate this issue, leading to significant advancements in the development of five-phase and six-phase variable-speed drives supplied by both voltage source and current source inverters. Indeed, the increase in the number of phases of the machine appeared as the best solution to the problem, as the lowest frequency torque ripple harmonic in an m-phase machine is caused by the time harmonics of the supply of the order $2m \pm 1$ and its frequency is $2m$ times higher than the supply frequency [34].

While the significance of multiphase machines in addressing torque ripple has somewhat diminished with the advent of pulse-width modulation (PWM) techniques in voltage-source inverters, other historical advantages remain relevant, such as improved fault tolerance and more effective power distribution across the phases [34].

2.1 Types of multiphase machines

Multiphase machines share fundamental characteristics with their three-phase counterparts. The types of multiphase machines parallel those of three-phase machines, including induction and synchronous variants. Typically, three-phase machines employ a distributed stator winding to achieve near-sinusoidal MMF distribution and are powered by sinusoidal currents. Despite efforts to achieve sinusoidal MMF distribution, some spatial harmonics are unavoidable even in multiphase machines [34].

In terms of stator winding design, multiphase machines offer greater flexibility. This versatility allows for either near-sinusoidal or quasi-rectangular MMF distributions through the use of distributed or concentrated windings across all types of AC machines. However, achieving a near-sinusoidal MMF distribution becomes progressively challenging as the number of phases increases. Indeed near-sinusoidal MMF distribution requires use of more than one slot per pole per phase ($q > 1$). For instance, a five-phase four-pole machine requires a minimum of 40 slots, while a seven-phase four-pole machine needs at least 56 slots. Machines attempting to achieve near-sinusoidal MMF distribution by adjusting the number of slots are referred to as machines with sinusoidal MMF [34].

Both concentrated and distributed stator winding designs exhibit strong magnetic coupling between stator phases. In permanent magnet synchronous machines, a concentrated winding design ($q = 1$) yields behavior similar to the one of brushless DC machines. In addition to the two previously mentioned stator winding designs, a third type has emerged as a viable option in the last decade, the so-called modular or fractional-slot concentrated-winding (FSCW) design, mainly used in conjunction with PM machines. Modular or FSCW designs aim to minimize stator phase coupling, enhancing fault tolerance. Spatial flux distribution in these machines, including brushless DC machines, is shaped by magnets, requiring stator current supply to match spatial flux distribution for optimal performance.

In designing the stator winding of an m-phase machine, a symmetrical multiphase system is achieved when the spatial displacement between any two consecutive stator phases equals $\alpha = 2\pi/m$. This symmetry is always present when the number of phases is an odd prime number. However, when the number of phases is an even number or an odd number that is not a prime number, a different approach to stator winding is necessary. This involves creating k windings, each with a subphases, where $m = a \cdot k$. Typically, a equals 3 (although 5 is also possible) and $k = \{2{,}3{,}4{,}5 \ldots\}$. In such cases, the spatial displacement between the first phases of the two consecutive subphase windings is $\alpha = \pi/m$, resulting in an asymmetrical distribution of magnetic winding axes in the machine's cross-section, leading to what are known as asymmetrical multiphase machines. In such multiphase machines, there are k neutral points, typically isolated for operational reasons [34].

2.2 Advantages and disadvantages of multiphase machines

The advantages of multiphase machines over their three-phase counterparts vary depending on the stator winding design. However, some benefits apply universally across all stator winding configurations [34]:

- lower per phase current compared to the three-phase counterpart. Indeed, by distributing power across a greater number of inverter legs, a lower-rated semiconductor switches can be utilised for a given machine's output power;
- enhanced fault tolerance capability due to the larger number of phases, ensuring independent flux and torque control;
- despite the number of phases, only two currents are required for the flux/torque control of an AC machine;
- low torque ripple due to increase of number of phases m.

On the other hand, multiphase machines necessitate the utilization of customized m-phase inverters tailored for variable-speed applications. While these inverters play a crucial role in driving multiphase motors efficiently, the integration of power electronics introduces additional complexity, limited standardization, and higher costs.

Additionally, there is limited standardization in the design and implementation of multiphase motors compared to more established single-phase and three-phase motor technologies.

Furthermore, machines with sinusoidal winding distribution offer additional advantages, including lower harmonic content of the MMF leading to reduction in noise emitted by the machine and improved efficiency compared to a three-phase machine and the independent control of multimotor multiphase drive systems using a single power electronic converter supply [34].

Regarding FSCW (Fractional-Slot Concentrated Winding) machines, notable benefits in choosing this design configuration are:

- high power density and elevated efficiency;
- reduced end-winding lengths, leading to a decrease in the axial length of the machine and copper losses. This reduction occurs because the coil pitch y_q is set to unity [36];
- reduced mutual coupling between phases;
- even lower torque ripple thanks to a low periodicity between the number of slots and the pole pairs;
- high slot fill factor can be achieved with specific coil winding technology;
- improved flux-weakening capabilities;

However, their benefits come at a cost of the generation of excessive rotor losses, particularly during high-speed operation, due to large spatial harmonic components [7].

2.3 Selection of the number of phase

Given the advantages described in Section 2.2, namely high power density, lower torque ripple, and superior fault-tolerant capabilities observed in FSCW motors compared to counterparts with concentrated and distributed windings, the FSCW configuration has been considered as a viable configuration to be analyzed in this work. Additionally, the concentrated winding motor has been chosen as a comparative model to evaluate the performance of the FSCW configuration.

When selecting the number of phases, it is crucial to emphasize that an increase in the number of phases results in a substantial reduction of torque ripple, thereby enhancing motor performance [24, 25]. Furthermore, due to the improved distribution of winding, joule losses decrease proportionally with the increase in the number of phases [49], as depicted in Table 2.1. However, even though the magnetic motive force (MMF) space harmonic content of a five-or seven-phase winding is lower than that of a three-phase winding, the rotor loss reduction achieved by increasing the number of phases is lower than expected [27].

In addition, it is essential to acknowledge that this comes with an increase in the complexity of the machine and, despite the fact that the space harmonic content of the MMF is lower in a five-phase or seven-phase winding compared to a three-phase winding, the reduction in rotor losses achieved by increasing the number of phases in a FSCW configuration is not significantly lower [27]. Hence, a decision has been made to opt for a five-phase motor configuration, as it guarantees a good balance between simplicity and improved performance compared to its three-phase counterpart.

Table 2.1 – Reduction in stator Joule loss by increasing the number of phases m

Phase number m	5	6	9	12	15	∞
Joule loss reduction (%)	5.6	6.7	7.9	8.3	8.5	8.8

Table 2.1 presents the reductions in stator joule losses achievable with multiphase windings compared to an equivalent machine wound with a three-phase winding of the same pitch. The reduction in Joule losses is attributed to the fact that machines with an increasing number of phases benefit from the reduction in the amplitude of higher harmonic orders, thereby decreasing the joule losses in the stator.

3 Theoretical background

This chapter provides a comprehensive examination of the MMF distribution for a Fractional-Slot Concentrated Winding. Additionally, it elaborates the methodology for evaluating the winding factor and delineates the necessary requirements for a feasible winding configuration.

3.1 Theory of Fractional slots concentrated winding

Fractional slot winding occurs when the number of slots per pole and per phase q is not equal to a whole number and therefore it can be expressed as a fraction between two non divisible natural numbers [14]:

$$q = \frac{Q}{2p \cdot m} = \frac{z}{n} \tag{3.1}$$

Two types of fractional slot winding exist, one where $q > 1$ and the other where $q < 1$. The former generally leads to a distributed winding with short-pitch coils, and as such it will not be viewed in more detail in this work. When $q < 1$, if the coil pitch calculated in terms of the number of slots is $y_\mathrm{q} = Q/2p$ is close to unity, meaning that $q \approx 1/m$, this results in tooth coils spanning precisely one tooth between two slots. Consequently, this type of tooth coil winding is named fractional slot concentrated winding (FSCW) and is often used in machines with a Permanent Magnet Rotor [14, 38].

It's important to emphasize that when $q < 1$ and $q \not\approx 1/m$, this results in distributed winding systems, instead of fractional slot concentrated winding systems. For instance, in a winding with $m = 7$, $Q = 21$ and $2p = 4$, the number of slots per pole and per phase $q = 3/4$ leads to a double-layer fractional distributed slot distributed winding, while, in a winding with $m = 7$, $Q = 7$ and $2p = 6$, the number of slots per pole and per phase is equal to $q = 1/6 \approx 1/m = 1/7$ and therefore this leads to a double-layer fractional slot concentrated winding [14].

In general fractional slot concentrated winding can be design with a single-layer or a double-layer, although more advanced designs exist [5, 18]. Single-layer fractional slot concentrated winding translates in having only one coil in each slot, while double-layer fractional slot concentrated winding translates in having two coils in each slot. It is always possible to achieve double-layer winding once the winding feasibility is met. Conversely, single-layer winding is only possible according to the some constraints [26].

Certain fractional slots concentrated winding configurations, like $q = z/m$ or $q = 1/m$, where the denominator n is an integer multiple of m, are less common due to resulting asymmetries in the magnetic field. This asymmetry leads to varying impedance and current consumption in each phase of a symmetric multi-phase system [14].

In fractional slot concentrated winding, the fundamental harmonic that is able to couple with the flux generated by the permanent magnets of the rotor and therefore is producing a torque, is the synchronous or main harmonic. Conversely from distributed winding, the synchronous harmonic is equal to the number of pole pairs $\nu' = p$. In FSCW, specific numbers of harmonics are present based on the winding system. Both even and odd harmonics can exist due to the unique geometric arrangement and distribution of slots and coils [38].

3.1.1 Analysis of MMF distribution in FSCW Stators

In FSCW machine the harmonic wave contained in the field excitation curve with the longest wavelength is generally not the working harmonic and is therefore often referred not as the fundamental harmonic wave but as the longest sub-harmonic wave. In order to generate a constant torque, the pole number and the speed of the working harmonic must match the pole number and the speed of the rotor field. All harmonics that do not have the same pole number and speed of the rotor field are responsible for producing iron losses and cogging torque. The harmonic waves faster than the working harmonic $\nu < p$ are called 'sub-harmonic waves', while the harmonic waves with shorter wavelengths $\nu > p$ are called 'harmonics'. Generally the sub-harmonic waves are the predominant cause of high iron losses in FSCW machine. [14]

The velocity, or in better word the spinning frequency, of a generic MMF harmonic wave is directly proportional to the order of the harmonic. Consequently, sub-harmonics exhibit lower frequencies compared to the main harmonic, although their amplitudes increase as the order of the sub-harmonic decreases, leading to higher rotor losses [43]. This is due to the fact that the amplitude of the MMF is inversely proportional to the harmonic order. For instance, in the case of a three-phase FSCW machine with a 9-slot 8-pole configuration and a double-layer winding, the sub-harmonics present are the 1st and the 2nd, while the main harmonic is the 4th. The MMF amplitude of the 1st harmonic is divided by 1, and that of the 2nd by 2, while the 4th is divided by 4. Therefore, when everything is normalized with respect to the main harmonic (4th), and the winding factor is the same for all harmonics, the amplitude of the first sub-harmonic is four times higher than the main one. The sub-harmonics typically have lower winding factors than the main harmonic, which partially mitigates the issue.

In FSCW, each coil of the stator is wound around a single tooth, resulting in a winding span of $\frac{2\pi}{Q}$. When considering only a single coil of the machine winding, it can be demonstrated that the spatial MMF distribution assumes the shape of a square pulse with a width equal to $2\pi/Q$ mechanical radians. This distribution, depicted in Fig. 3.1, varies over time and space and can be represented by the following equation:

$$M(\theta_\mathrm{s},t) = \begin{cases} \left(1 - \frac{1}{Q}\right) n_\mathrm{c} i_j & \text{under the tooth} \\ -\frac{1}{Q} n_\mathrm{c} i_j & \text{elsewhere} \end{cases} \tag{3.2}$$

Where M represents the Magnetomotive Force in Ampere-turns, θ_s denotes the stator peripheral angle in mechanical radians, n_c is the number of turns in the coil, and i_j represents the instantaneous current in Ampere flowing through the phase j winding where the coil is located [22]. The spatial MMF distribution of a single coil is depicted in Fig. 3.1 and the symbol $\odot$ indicates a flow of current into the paper, while the symbol $\otimes$ indicates a flow of current out of the paper.

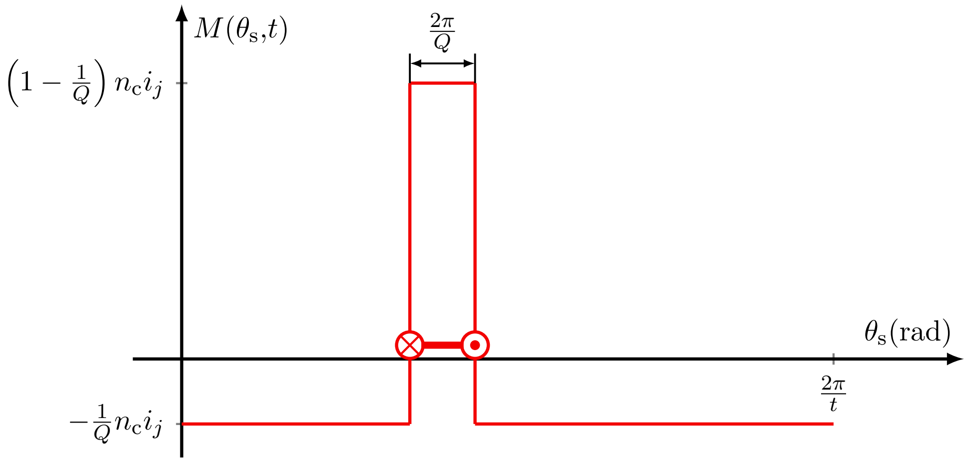

Figure 3.1 – MMF distribution of a single coil.

The spatial distribution of Magnetomotive Force (MMF) for a phase winding is determined by superimposing the Magnetomotive Forces of all its coils. Because of the periodic nature of winding, the MMF for each phase winding consists of periodic square pulses and can be represented by a Fourier series of harmonics [22].

Every winding system is composed of t primary windings, where the periodicity of the winding system is determined by the greatest common divisor of Q and p, denoted as:

$$t = \mathrm{GCD}(Q,p) \tag{3.3}$$

Each set of t identical sub-windings encompasses $Q' = Q/t$ slots and $p' = p/t$ pole pairs. However, in fractional-slot windings, this is not always holds true. There may be instances where the sequence of the number of coils per coil group within the primary winding repeats twice, but with opposite directions of rotation[38]. For instance, considering a FSCW three-phase machine with a 12-slot and 10-pole configuration, utilizing a double-layer winding. In this case, since $t = 1$, it is possible to demonstrate there is only one primary winding. However, there are two identical sub-windings with different coil polarity.

Since the primary winding spans $2\pi/t$ mechanical radians within the stator, a coil pair in the primary winding is defined as two coils displaced by π/t within the stator. The polarities of the coils determines the resultant Magnetomotive Force of the coil pair. Indeed, if the coils have the same polarity, the spatial MMF distribution of the coil pair has only odd number harmonics and is the same as the one depicted in Fig. 3.2. The Fourier series describing this spatial MMF distribution contains only sinusoidal waves, because it is an odd function and is represented solely by sine functions in the Fourier series expansion:

$$M_{\mathrm{coil}}(\theta_s,t) = \sum_{\nu=1,3,5,\ldots}^{\infty} \frac{4n_c i_j}{\nu\pi} \sin\left(\frac{\nu\pi}{Q}\right) \cos(\nu\theta_s - \omega t) \tag{3.4}$$

The magnitude of the MMF a generic harmonic order ν for a single coil pair is equal to:

$$\hat{M}_{\mathrm{coil},\nu} = \frac{4n_c i_j}{\nu\pi} \sin\left(\frac{\nu\pi}{Q}\right) \tag{3.5}$$

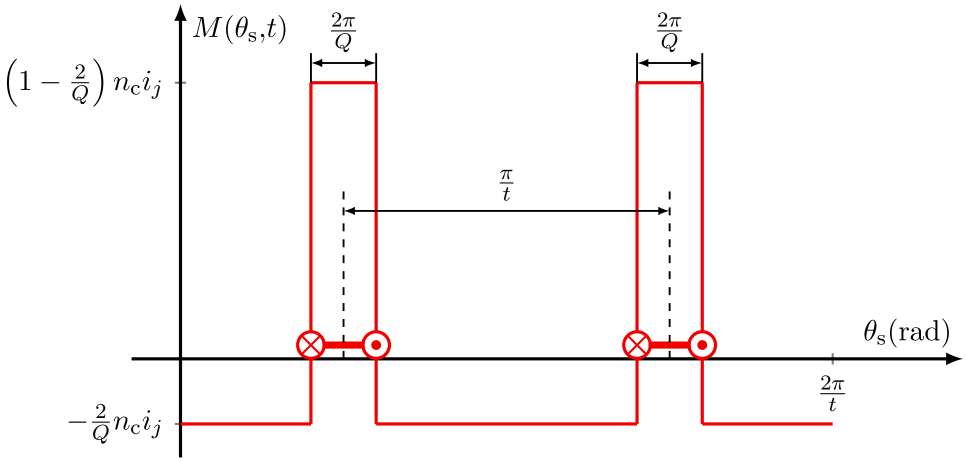

Figure 3.2 – MMF distribution of a coil pair with same polarity

Conversely, if the polarities of the coils are opposite, the MMF produced by the coil pair is the same as represented in Fig. 3.3. The Fourier series describing the MMF of coils with opposite polarities consists of cosine waves. However, its representation is not straightforward. Therefore an analytical equation is not provided.

It is possible to evaluate the harmonic content of a the MMF produced by a m-phase motor with FSCW and Q number of slots and $2p$ number of poles [23]. For instance, by superimposing the effects of each coil in a winding system with 20 slots, 18 poles, 4 layers, and five phases, it is possible to evaluate the distribution of the MMF produced by the winding itself, as depicted in Fig. 6.15a. After that, it's possible to analyze the signal via Fourier transformation.

It is important to note that analytical formulas are available for specific groups of FSCW machines, based on the fraction number (3.1) discussed previously [22].

It is therefore possible to obtain the analytical description of the MMF distribution as a function of spatial coordinate θ_s and time t, thus it is possible to write:

$$M_{\text{winding}}(\theta_s, t) = \sum_{\nu=1}^{\infty} \hat{M}_{\text{winding},\nu} \cos(\nu\theta_s)\cos(\omega t) \tag{3.6}$$

Where $\hat{M}_{\text{winding},\nu}$ is the amplitude of the ν-th harmonic in the Fourier series and it is equal to:

$$\hat{M}_{\text{winding},\nu} = \frac{2\sqrt{2}}{\pi}\frac{NI}{\nu}k_{\text{w},\nu} \tag{3.7}$$

The amplitude of the ν-th harmonic depends on the rms value of the injected current in the stator winding I. The total sum of the MMF wave produced by a m-phase system for a generic harmonic order ν is:

$$M_{\nu}(\theta_s,t) = \sum_{\nu=1}^{\infty} \frac{\sqrt{2}m}{\pi}\frac{NI}{\nu}k_{\text{w},\nu}\cos(\nu\theta_s - \omega t) \tag{3.8}$$

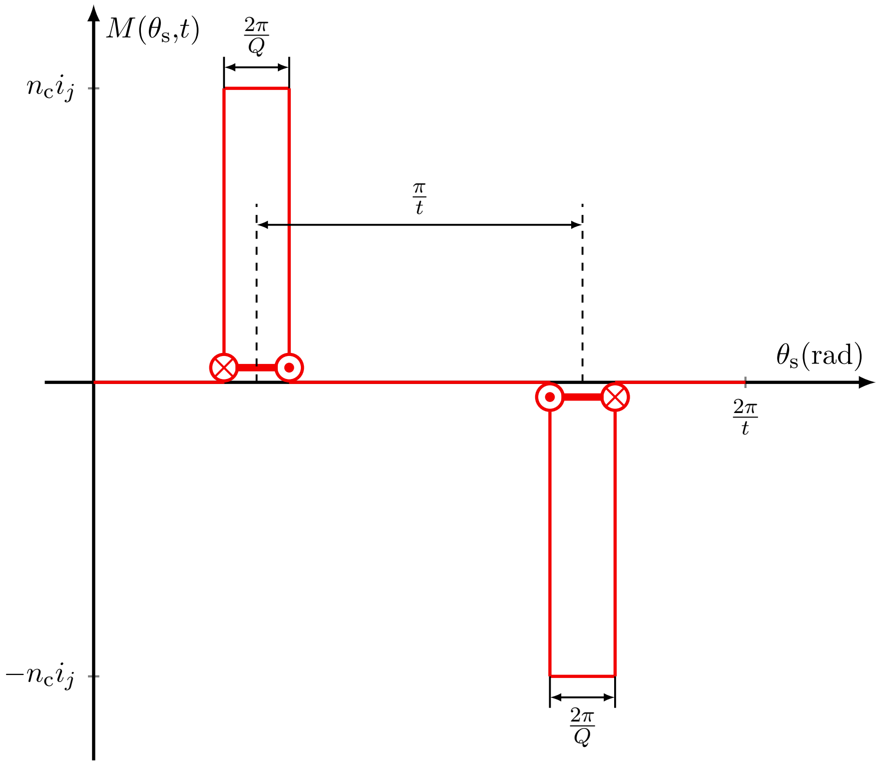

Figure 3.3 – MMF distribution of a coil pair with opposite polarity.

The amplitude of the resultant MMF is:

$$\hat{M}_\nu = \frac{\sqrt{2}m}{\pi}\frac{NI}{\nu}k_{\mathrm{w},\nu} \tag{3.9}$$

3.1.2 Winding factor

The winding factor k_w of a winding system is the ratio between the magnitude of the vector of the electromotive force (EMF) of the analyzed machine and the magnitude of the vector in the case concentrated winding, therefore with a full-pitch winding and $q = 1$. The winding factor converts a winding originally distributed along the circumference with N_s turns into a concentrated winding with $k_w N_s$ effective turns [14]. Several methods exist in order the evaluate the winding factor. For instance, it is possible to draw the star of slot of the winding and evaluate the winding factor as the ratio of the vector sum of the EMF, produced by the fed-in current coils, and the sum of the magnitude of the vectors [10]. Another viable method is to evaluate the winding factor via Fourier analysis of the Magneto motive force. Additionally, a novel matrix-based technique can be employed to evaluate the winding factor. A detailed explanation of this method is provided subsequently.

The electromotive force and torque produced by a machine are intricately linked to the winding factor. Consequently, a primary objective during the design phase is to maximize the winding factor value, in order to ensures high performance of the machine.

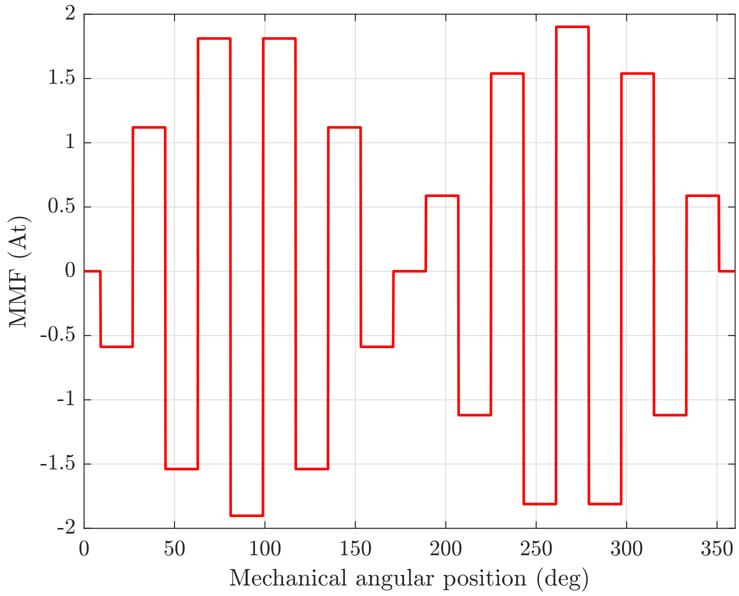

Figure 3.4 – Analytical distribution of MMF for a 20-slots, 18-poles, 4-layer, five-phase machine

Star of slot

The star of slot serves as a powerful tool for visualizing and analyzing the winding system of electric motors. It is a graphical representation used to depict the phasors of the main harmonic of the electromotive force (EMF) induced in each individual conductor or coil side within the stator slots of an electric motor. Utilizing the star of slots enables the selection of the optimal coil pitch and the determination of factors such as the distribution factor and pitch factor [12].

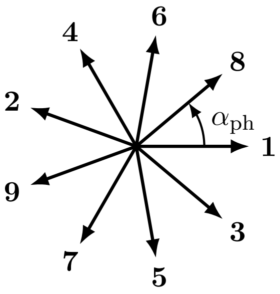

Figure 3.5 – Star of slot of a 3-phase, 9 slots and 8 poles winding with a double-layer.

The star of slot is characterized by Q/t spokes, each formed by t phasors, where Q is the number of slots and t is the electrical periodicity of the machine. The angle between EMF phasors of two slots is given by $\alpha_{\mathrm{s}}^{\mathrm{e}} = p\alpha_{\mathrm{s}}$, where α_{s} represents the slot angle in mechanical radians. Additionally, the angle between two adjacent spokes is equal to:

$$\alpha_{\mathrm{ph}} = \frac{2\pi t}{Q} \tag{3.10}$$

Once the graphical representation of the star of slots is created, it is possible to divide the entire circumference into different sectors. The number of sectors depends on the value of

m, accounting for both positive and negative sectors of a phase. Thus, the total number of sectors equals $2m$. Between each positive and negative phase sector there is an angle of 180°. Once the sectors are delineated on the star of slots, it becomes feasible to position a phase coil within a specific slot based on whether the spoke falls within the range of the phase sector.

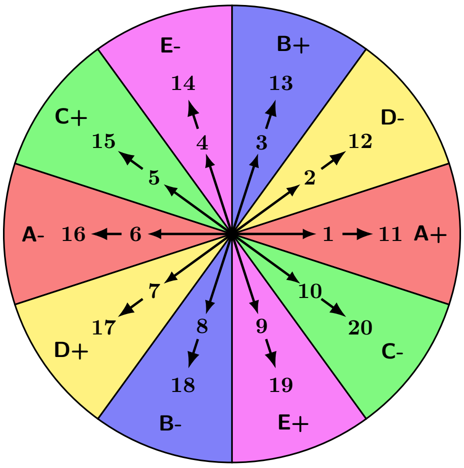

Figure 3.6 – Star of slot for 20-slot 4-pole, five-phase machine

For instance, the star of slots of a 20-slot 4-pole, five-phase machine is depicted in Fig. 3.6. Here, it is evident that in slots 1 and 11, the positive coils of phase-a are placed, while in slots 6 and 16, the positive coils of phase-a are located. By employing this method and applying it to all phase sectors, the complete winding arrangement of the machine is derived. It is noteworthy to mention that while the aforementioned method holds true for distributed and concentrated windings, it is not the case for Fractional Slot Concentrated Windings FSCW. With FSCW, the allocation of the coils remains the same, but it is necessary to return the coil after one slot, since the coil pitch is equal to one. Therefore, if the positive phase coil of phase-a is placed in slot 1, its return must be placed in slot 2. Conversely, if the negative phase coil of phase-a is placed in slot 6, its return must be placed in slot 7.

3.1.3 Single-layer winding

The single-layer winding is a special sub-case of the double-layer winding. It is feasible to convert a double-layer to a single-layer winding. When the following criteria are fulfilled:

- the coil pitch y_q has to be odd;
- if the machine periodicity t is even, the transformation is always possible. However, when the machine periodicity t is odd, the transformation is feasible only if the number of spokes Q/t is even [10].

With even periodicity, it can be demonstrated that there are t phasors per spoke, alternating between even and odd numbers. Consequently, one phasor per spoke (e.g., the even-numbered phasor) can be removed, while the other (e.g., the odd-numbered phasor) is doubled. This adjustment results in a new star of slots configuration along with the final winding arrangement. Despite the changes, the winding factor of the main harmonic remains unchanged from the double-layer winding, while the machine's periodicity, corresponding to the number of phasors per spoke, is halved.

On the other hand, when the winding has odd periodicity and an even number of spokes Q/t, each phase possesses an even number of spokes, ensuring an equal distribution of phasors over the North and South poles. In this configuration, it can be demonstrated that adjacent phasors are alternately odd-numbered and even-numbered. By removing the even-numbered phasors, each phase remains balanced thereby achieving the single-layer winding configuration. In this case, the main winding factor of the single-layer winding increases compared to that of the double-layer winding, as each phase exhibit a lower number of phasors out of phase. Despite this change, the machine periodicity remains unchanged [10].

For a single-layer winding system, evaluating the winding factor is not straightforward, as there is no existing analytical equation to perform this evaluation. It is therefore necessary to use a different approach. In [39] a general method to calculate the winding factor by only considering stator parameters has been developed. The method is based on the matrix representation of a winding and requires the knowledge of the number of slots Q, phases m and layers n_{layer}. Additionally, it requires knowledge of the spatial distribution of a single phase, which refers to how the coils of that phase are arranged within the stator winding.

In order to utilize the approach described in [39], the connection matrix $\mathbf{D}_w$ with dimension of $m \times Q \cdot n_{\text{layer}}$ has to be calculated.

$$\mathbf{D}_w = \frac{1}{n_{\text{layer}}} \times \begin{bmatrix} D_{w_k}^{1,1} & D_{w_k}^{1,2} & \dots & D_{w_k}^{1,Q_s} \\ D_{w_k}^{2,1} & D_{w_k}^{2,2} & \dots & D_{w_k}^{2,Q_s} \\ \vdots & \vdots & \ddots & \vdots \\ D_{w_k}^{m,1} & D_{w_k}^{m,2} & \dots & D_{w_k}^{m,Q_s} \end{bmatrix} \tag{3.11}$$

The single element $D_{w_k}^{i,u}$ represents the connection status between phase i and u-th slot, where $i = \{1, \dots, m\}$, $u = \{1, \dots, Q\}$ and $k = \{1, \dots, n_{\text{layer}}\}$. The value of each element $D_{w_k}^{i,u}$ is equal to:

- 0 if there is no conductor of phase i in the u-th slot and k-th layer;
- $+1$ if there is a forward conductor of phase i in the u-th slot and k-th layer ($\odot$);
- -1 if there is a return conductor of phase i in the u-th slot and k-th layer ($\otimes$).

In the matrix-based approach, only the first row is considered of $\mathbf{D_w}$, therefore a simplified matrix of a generic phase is used, since the phases are balanced.

The connecting matrix can be constructed using the corresponding star of slots, and the entire process can be automated.

For instance, the star of slot for the main harmonic of a 3-phase 12 slots and 10 poles winding with single-layer is displayed in Fig. 3.5. By observing which number of spokes are contained in the phase sectors, it is possible to allocate the right value to the element in the connection matrix.

$$\mathbf{D}_w = \frac{1}{1} \times \begin{bmatrix} 1 & -1 & 0 & 0 & 0 & 0 & -1 & 1 & 0 & 0 & 0 & 0 \\ 0 & 0 & -1 & 1 & 0 & 0 & 0 & 0 & 1 & -1 & 0 & 0 \\ 0 & 0 & 0 & 0 & 1 & -1 & 0 & 0 & 0 & 0 & -1 & 1 \end{bmatrix} \tag{3.12}$$

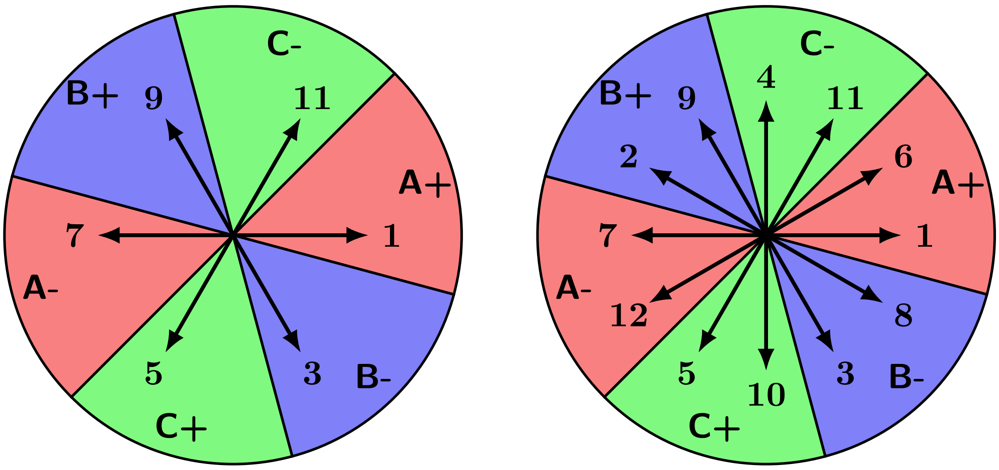

(a) 1-layer winding **(b)** 2-layer winding

Figure 3.7 – Star of slot for 12-slot 10-pole, three-phase machine

Conversely, the connection matrix in the case of a double-layer winding is as follows:

$$\begin{gathered} \mathbf{D}_w = \frac{1}{2} \times \left[\begin{array}{cccccccccccc} 1&1&-1&0&0&0&0&0&0&0&0&1\\ 0&0&0&1&-1&-1&1&0&0&0&0&0\\ 0&0&0&0&0&0&0&-1&1&1&-1&0 \end{array} \right. \\ \left. \begin{array}{cccccccccccc} -1&-1&1&0&0&0&0&0&0&0&0&-1\\ 0&0&0&-1&1&1&-1&0&0&0&0&0\\ 0&0&0&0&0&0&0&-1&1&1&-1&0 \end{array} \right] \end{gathered} \tag{3.13}$$

Afterwards, the winding factor is computed following the steps described in [39].

3.1.4 Double-layer winding

For a double-layer winding, both the matrix-based approach described previously and existing analytical equations are viable methods for calculating the winding factor [38].

In a FSCW system with double-layer, it is possible to evaluate the total winding factor as the product of the pitch factor $k_{p,\nu}$ and the distribution factor $k_{d,\nu}$. The general formula for evaluating the winding factor is as follows [38]:

$$k_{\mathrm{w},\nu} = k_{p,\nu} k_{d,\nu} = \sin\left(\frac{\nu}{p}\frac{y_q}{y_p}\frac{\pi}{2}\right) \frac{\sin\left(\frac{\nu}{\nu^*} q_a \tilde{g} \frac{\pi}{Q'}\right) - \cos\left(\frac{\nu}{\nu^*}\tilde{g}\pi\right) \sin\left(\frac{\nu}{\nu^*} q_b \tilde{g} \frac{\pi}{Q'}\right)}{\frac{Q'}{m} \sin\left(\frac{\nu}{\nu^*}\tilde{g}\frac{\pi}{Q'}\right)} \tag{3.14}$$

Where:

- $y_p = Q/2p$ is the pole pitch computed in number of slots and y_q is the coil pitch, also computed in number of slots. Usually it is equal to the unity in FSCW.
- $t = G.C.D.\,(Q, p)$ is the periodicity of the machine.

- $Q' = Q/t$ and $p' = p/t$ are the numbers of slots and poles of the primary winding, respectively.
- g^* is the smallest natural number for which the following expression is equal to an integer number.

$$\tilde{g} = \frac{1 + g^* Q'}{p'} \tag{3.15}$$

- q_a and q_b are the integers that are adjacent to the value of $Q'/2m$.
- $\nu^* = t$ which is the smallest order number of the harmonics generated by or induced within a single phase.

If ν/p is an odd number the formula (3.14) can be simplified in (3.16).

$$k_{\mathrm{w},\nu} = \sin\left(\frac{\nu}{p}\frac{y}{y_p}\frac{\pi}{2}\right)\frac{\sin\left(\frac{\nu q \pi}{p y_p 2}\right)}{nq\sin\left(\frac{\nu\pi}{pny_p2}\right)} \tag{3.16}$$

As previously mentioned in 3.1, when considering FSCW, only specific numbers of harmonic can be present. The following formula (3.17) evaluates the number of harmonics for a m-phase fractional slot concentrated winding:

$$\tilde{\nu} = p\left(1 + \frac{2mg}{n}\right) \tag{3.17}$$

Where n is the denominator of the equation (3.1) while g is an integer number equal to $g = \{0, \pm 1, \pm 2, \pm 3, \ldots\}$.

3.1.5 Four-layer winding

Increasing the number of layers in a slot from 2 to 4 to achieve a four-layer winding is always feasible. However, the adoption of a four-layer winding may not be advantageous for every combination of slots and poles. In order to be convenient, it is necessary that each phase includes at least two spokes within a single sector of the star of slots. Since the number of spokes per phase is $Q/(mt)$ and each phase has two sectors, the adoption of a four-layer winding becomes both feasible and convenient when:

$$\frac{Q}{2mt} > 1 \tag{3.18}$$

When the formula 3.18 is not satisfied, the adoption of the 4-layer winding is unfavorable. This is due to the reduction of the main winding factor and the absence of mitigation of sub-harmonic waves.

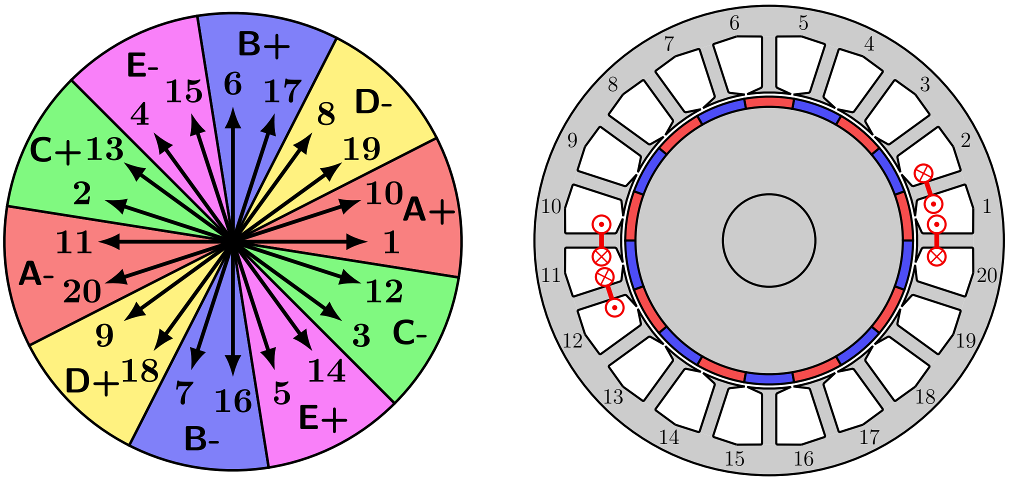

(a) Star of slots **(b)** Winding layout of phase A

Figure 3.8 – 20-slot 18-pole, 2-layer winding, five-phase machine

In the star of slot for the 4-layer winding, the phases sectors are double the ones of the star of slot for the double-layer, as depicted in Fig. 3.9a. The first positive and negative sectors are denoted by (+) and (−), respectively, while the second positive and negative sectors are denoted by (++) and (−−), respectively. The second sector is shifted of the angle α_{sh4}. In order to maximize the winding factor of the main harmonic $\nu' = p$, the shifting angle α_{sh4} has to minimized [5].

Two different approaches are present when choosing the shifting angle α_{sh4}, based on whether Q/t is even or odd:

- Q/t *even*: when the ratio Q/t is an even number, the number of spokes in the positive and negative sectors is the same and therefore all positive and negative sectors of all phases contain the same number of spokes. In order to maximize the winding factor the shift angle has to be equal to the angle between two spokes, therefore $\alpha_{\text{sh4}} = \alpha_{\text{ph}}$.
- Q/t *odd*: when Q/t is an odd number, the number of spokes in the positive sectors differs by 1 with respect to the spokes number in the negative sector. Therefore it is

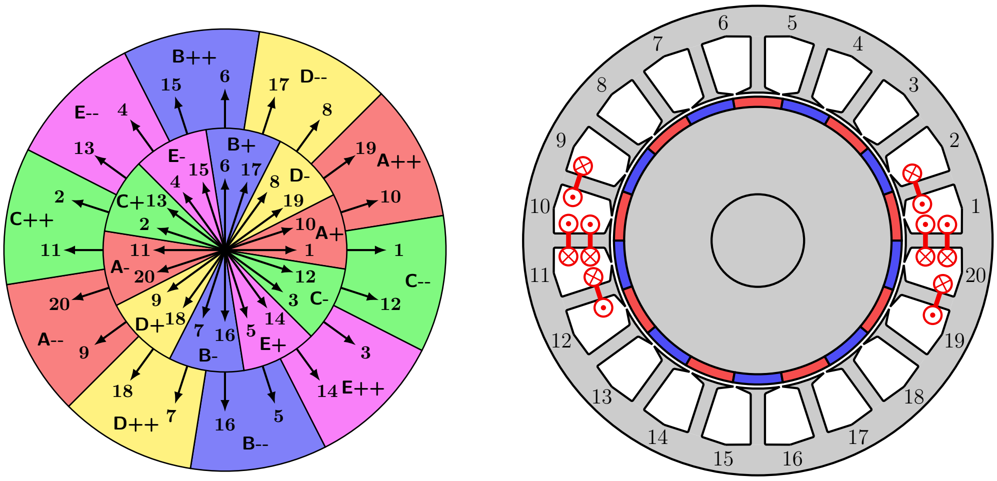

(a) Star of slots **(b)** Winding layout of phase A

Figure 3.9 – 20-slot 18-pole, 4-layer winding, five-phase machine

possible to have two different shifting angles. The first possibility is to have a shifting angle equal to the angle between two spokes, hence $\alpha_{\text{sh4}} = \alpha_{\text{ph}}$. With this configuration the number of spokes in the first positive sector (+) is equal to the number of spokes in the second positive sector (++). The same is true also for the two negative sectors of the same phase.
On the other hand, it is possible to have a shifting angle equal to half the angle between two spokes, hence $\alpha_{\text{sh4}} = \alpha_{\text{ph}}/2$. Conversely, with this configuration the number of spokes in the first positive sector (+) is not equal to the number of spokes in second positive sector (++). The same is true also for the two negative sectors of the same phase. Compared to the first one, this second case maximize the winding factor of the main harmonic $\nu' = p$, since the spokes of the coils connected in series are closer respect to the previous case.

For a 4-layer winding, the formula express in (3.14) is no longer capable of evaluating the winding factor, since it is valid only for a 2-layer winding. It is therefore necessary to use the matrix-based approach described in Sec. 3.1.3.

In Fig. 3.10 the full winding layout for 20-slot 18-pole, 4-layer winding, five-phase machine is depicted.

3.1.6 Winding feasibility

In a FSCW m-phase winding only certain combinations of slots Q and poles $2p$ are feasible. In order to obtain a symmetric fractional slot concentrated winding system, n must not be divisible by the number of phases m, as previously discussed in Section 3.1. Therefore the following expression can be obtained [30]:

$$\frac{2p}{n} = \text{integer}, \quad \text{with } n \neq \{m, 2m, 3m, ...\} \tag{3.19}$$

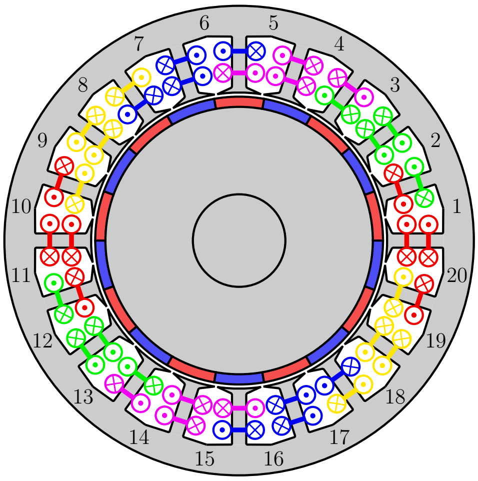

Figure 3.10 – Winding layout, 20-slot 18-pole, 4-layer winding, five-phase machine

3.1.7 Cogging torque

In PMs motor the interaction between the permanent magnets of the rotor and the anisotropy, due to the presence of the teeth of the slotting, generate an undesired torque, named cogging torque. The selection of a specific combination of slots and poles has a direct impact on the cogging torque. It is possible to evaluate the number of periods of the cogging torque waveform during a rotation of a slot pitch via the following formula:

$$N_p = \frac{2p}{\mathrm{GCD}\,(Q, 2p)} \tag{3.20}$$

By maximizing N_p its is possible to minimize the cogging torque [8].

Magnetic pull

In electrical machines, radial forces along the air gap arise from interactions between magnets, coils current, and steel in the stator and rotor. Uneven distribution of these forces can lead to unbalanced rotating magnetic pulling forces, leading to the formation of noise and vibration in the machine. In order to address this, machines can be designed with force asymmetry. Alternatively, a simpler approach involves selecting pole and slot combinations with periodicities in the winding layout. This compensates opposing forces, preventing a net radial force. The machine winding periodicity $t = \mathrm{GCD}(Q,p)$ evaluates the number of repeated pattern in the winding. When $t > 1$ a balanced distribution of magnetic forces is achieved [22]. Nevertheless, not all winding with a winding periodicity equal to the unit have unbalanced distribution of magnetic forces. Indeed, it is possible to achieve a machine without an unbalanced magnetic pull if the phase disposition of the winding is symmetrical $t' = \mathrm{GCD}(Q,p) > 1$. In other words, the winding has to have symmetries of the coil arrangements without considering the current sign.
For instance, with a three-phase motor having 12 slots and 10 poles, the winding periodicity is equal to $t = \mathrm{GCD}(Q,p) = 1$. However the phase disposition is symmetrical since $t' = \mathrm{GCD}(Q,p) = 2$, therefore the radial forces form both halves of the motor compensate each other.

3.2 Optimal slot-pole number combination

In order to obtain a high performing winding system, the winding factor of the main harmonic has to be sufficiently high. It is possible to achieve a high winding factor if the coil span is as close as possible to the pole pitch $y_p = 2\pi/2p$. In fractional slot concentrated winding the coil span is equal to the coil pitch $y_q = 2\pi/Q$, therefore the following expression can be derived [30]:

$$Q \approx 2p \tag{3.21}$$

By rearranging the expression (3.21) it is possible to obtain that $q \approx 1/m$, as previously described in Section 3.1.

It is possible to identify the optimal number of slots and poles combinations by evaluating the winding factor $k_{\mathrm{w},\nu}$ for the synchronous main harmonic ($\nu' = p$) and by selecting only the winding-systems with $q \approx 1/m$.

3.2.1 Winding Performance Index

In a m-phase motor, with $m > 5$, it is possible to enhance the torque via stator Harmonic Current Injection (HCI) [7, 34]. Therefore, when selecting the optimal slot-pole number combination it is essential also to evaluate the winding factor $k_{\mathrm{w},\nu}$ of the third main harmonic $\nu = 3\nu' = 3p$.

In order to identify the optimal winding configuration, it is essential to introduce the Winding Performance Index (WPI) [22]. The WPI serves as an evaluative measure for determining the most efficient winding layout in relation to its torque density. In three-phase machines, optimal torque production is achieved by selecting the winding layout characterized by the highest main harmonic winding factor $k_{\mathrm{w},p}$. However, this optimization process becomes considerably more intricate in multiphase machines employing the stator Harmonic Current Injection technique for torque enhancement. The average torque for a m-phase, $2p$ poles PM synchronous symmetrical machine, with m odd prime number, operating under the HCI technique is equal to:

$$T_{\mathrm{dq}} = \frac{m}{2} p \sum_{\nu} i_{\mathrm{q},\nu} \lambda_{\mathrm{pm},\nu} \tag{3.22}$$

where the harmonic order is $\nu = 1,3,\ldots$ and $\nu < m$, while the harmonic current of ν-th order in the q-axis is $i_{\mathrm{q},\nu}$. The magnitude ratio of the ν-th harmonic current to the fundamental is typically equal to the corresponding ratio of the phase-to-neutral back-EMF harmonics. Therefore:

$$\frac{i_{\mathrm{q},\nu}}{i_{\mathrm{q},1}} = \frac{e_\nu}{e_1} \propto \frac{k_{\mathrm{w},\nu p} B_{\mathrm{g},\nu}}{k_{\mathrm{w},p} B_{\mathrm{g},1}} \tag{3.23}$$

The distribution of PM flux density in the air-gap is directly influenced by the rotor topology. In this work, only machines with surface-mounted permanent magnets are analyzed, therefore the PM flux density exhibits a square wave form. Assuming a slot-less stator, the rectangular

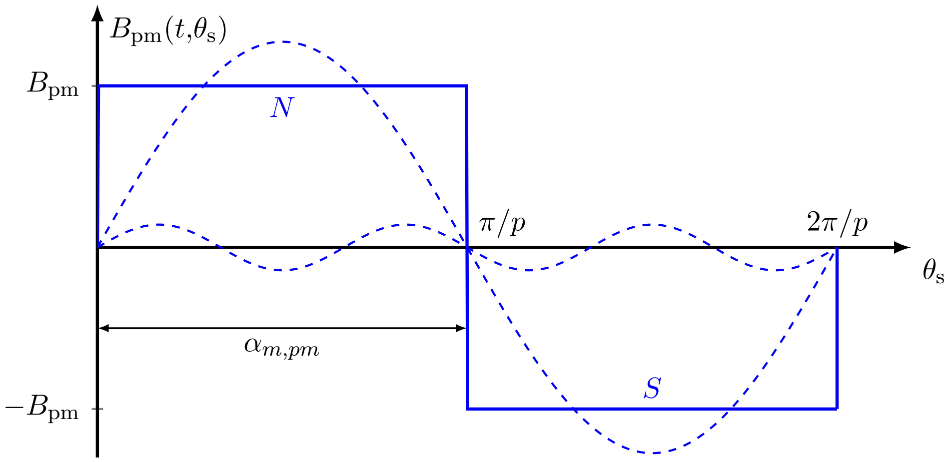

Figure 3.11 – Flux density distribution

PM flux density depicted in Fig. 3.11 can be mathematically represented using a Fourier series as:

$$B_{\mathrm{pm}}(t,\theta_{\mathrm{s}}) = \sum_{\nu=1,3,5\ldots}^{\infty} \hat{B}_{\mathrm{pm},\nu}\cos(\nu\theta_{\mathrm{s}} - \omega t) \tag{3.24}$$

where $\hat{B}_{\mathrm{pm},\nu}$ is the magnitude of the ν-th spatial harmonic component of the PM flux density, given by:

$$\hat{B}_{\mathrm{pm},\nu} = \frac{4B_{\mathrm{pm}}}{\nu\pi}\sin\left(\nu\alpha_{\mathrm{m}}^{\mathrm{e}}\right) \tag{3.25}$$

An electrical angle of the magnet of $2\alpha_{\mathrm{m}}^{\mathrm{e}} = 180°$ has been assumed to maximize both the fundamental and the third harmonic, for HCI operation. Therefore, the ratio of the third harmonic flux density to the fundamental flux is equal to:

$$\frac{\hat{B}_{\mathrm{pm},3}}{\hat{B}_{\mathrm{pm},1}} = \frac{\frac{4B_{\mathrm{pm}}}{\pi}\sin\left(3\alpha_{\mathrm{m}}^{\mathrm{e}}\right)}{\frac{4B_{\mathrm{pm}}}{3\pi}\sin\left(\alpha_{\mathrm{m}}^{\mathrm{e}}\right)} = \frac{1}{3} \tag{3.26}$$

Since the flux linkage of the ν-th harmonic $\hat{\lambda}_{\nu}$ is also proportional to the winding factor $k_{\mathrm{w},\nu}$ and to the peak flux density $\hat{B}_{\mathrm{pm},\nu}$, the winding performance index can be defined as:

$$\mathrm{WPI} = \sum_{\nu=1}^{m-2}\left(\frac{k_{\mathrm{w},\nu p}}{k_{\mathrm{w},p}}\frac{B_{\mathrm{max},\nu}}{B_{\mathrm{max},1}}\right)^{2} \tag{3.27}$$

An investigation is conducted to determine the best slot-pole configurations for 5-phase machines with 4-layer winding. Specifically, configurations with a number of slots $Q < 25$ and with a number of poles $2p < 28$ are investigated. The performance of the winding is quantified by the Winding Performance Index, hence it relies on the values of the winding factors of the first and third harmonics.

In [1, 42] a comparative analysis of different slot and pole combinations for a five-phase FSCW machine suggests that increasing the number of rotor poles positively influences the efficiency and torque density of the machine. However, this is achieved at the expense of an increase in the dc-link voltage requirement. Notably, the 20-slot/14-pole combination demonstrates superior flux distribution and lower core losses. Conversely, the 20-slot/18-pole combination exhibits lower torque ripple, both under healthy operating conditions and in fault scenarios.

Table 3.1 – Optimal slot/pole combination for 5-phase 4-layer winding

2p	Q	q	t	t′	N_p	$k_{w,p}$	$k_{w,3p}$	WPI
4	5	1/4	1	1	4	0.559	0.559	0.3472
6	5	1/6	1	1	6	0.559	0.559	0.3472
8	10	1/4	2	2	4	0.559	0.559	0.3472
12	10	1/6	2	2	6	0.559	0.559	0.3472
	15	1/4	3	3	4	0.559	0.559	0.3472
14	15	3/14	1	1	14	0.9321	0.4878	0.8952
16	15	3/16	1	1	16	0.9321	0.4878	0.8952
	20	1/4	4	4	4	0.559	0.559	0.3472
18	15	1/6	3	3	6	0.559	0.559	0.3472
	20	2/9	1	2	9	0.9635	0.7074	0.9839
20	25	1/4	5	5	4	0.559	0.559	0.3472
22	20	2/11	1	2	11	0.9635	0.7074	0.9839
	25	5/22	1	1	22	0.9497	0.6156	0.944
24	20	1/6	4	4	6	0.559	0.559	0.3472
	25	5/24	1	1	24	0.9649	0.7162	0.988
26	20	2/13	1	2	13	0.8692	0.1242	0.7572
	25	5/26	1	1	26	0.9649	0.7162	0.988
28	25	5/28	1	1	28	0.9497	0.6156	0.944

From the Table 3.1, it is possible to demonstrate that for a 5-phase FSCW system with 4 layers, two optimal configurations exist: 20 slots and 18 poles, and 20 slots and 22 poles. Both configurations are feasible and exhibit balanced distribution of magnetic forces, as well as very high values of the winding factor for the first and third harmonics.

It is possible to compare the harmonic content of the MMF and the winding factor of the 20-slot and 18-pole configuration, as depicted in Fig. 3.12a and Fig. 3.12b. From the results, it is evident that as the number of layers increases, so does the performance of the machine, as indicated by the lower harmonic content in the MMF. However, it is worth noting that there is a slight decrease in the winding factor of the main harmonic with the increase in the number of layers. Nevertheless, this decrease is counterbalanced by an even higher decrease in the winding factor for sub-harmonic and non-main harmonic waves.

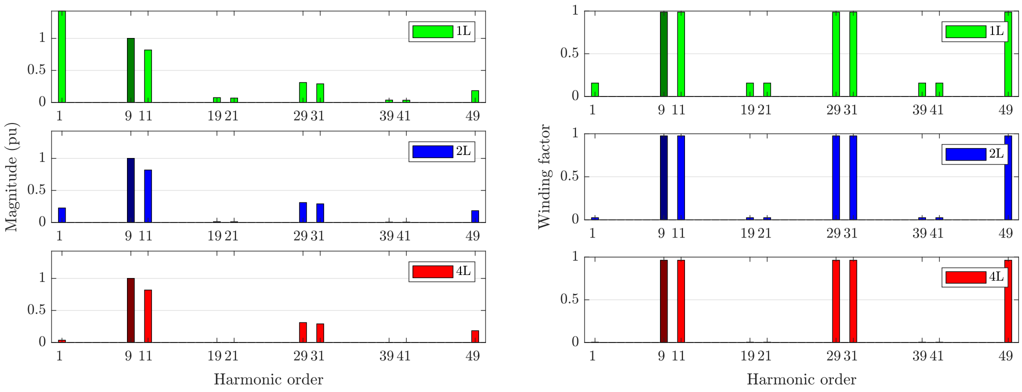

(a) MMF magnitude **(b)** Winding factor

Figure 3.12 – Comparison of single-layer (1L), double-layer (2L) and four-layer winding (4L) for 20-slots, 18-poles, five-phase machine

In the appendix, tables containing values of the winding factor for three-phase, five-phase and seven-phase windings with double and 4-layer winding are provided.

4 Design

In this chapter, the desing process of a general machine is outlined. Subsequently, a specific design approach is undertaken for two distinct configurations: firstly, the design of a FSCW five-phase machine with a 4-layer winding, with 20 slots and 18 poles; and secondly, the design of a concentrated winding machine with 20 slots and 4 poles.

4.1 Idealized electric machine

In order to perform a preliminary design of the machine some simplification have to be made. The real electric machine is therefore schematized with a simplified model, where the anisotropies, the non-linearities of the ferromagnetic material, and all the parameters not strictly necessary disappear, as depicted in Fig. 4.1b. For instance, the permeability of the iron is considered equal to $\mu_{\mathrm{Fe}} = \infty$ [12].

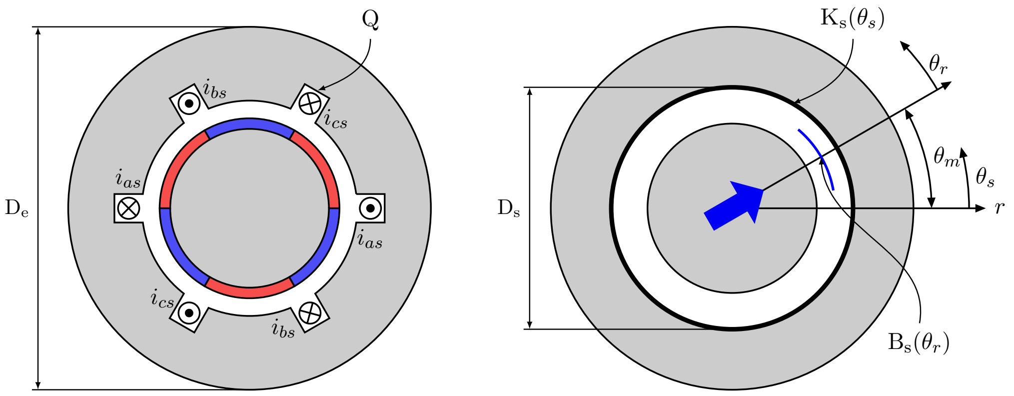

(a) Real machine

(b) Idealized machine

Figure 4.1 – 20-slot 18-pole, 4-layer winding, five-phase machine

The rotor becomes a simple cylinder for which the air gap is smooth. The angular position of the rotor relative to the stator is indicated by θ_{m}. The angular coordinate referred to the stator axis is indicated by θ_{s}. The angular coordinate referred to the rotor axis is indicated by θ_{r}.

The rotor is tasked with producing a magnetic induction field in the air gap. The rotor is responsible for generating a magnetic flux in the air gap. A sinusoidal distribution of flux in the air gap, centered on the rotor axis, is assumed, where:

$$B_{\mathrm{g}}(\theta_{\mathrm{r}}) = \hat{B}_{\mathrm{g}} \cos(\theta_{\mathrm{r}}) \tag{4.1}$$

The distribution has radial direction, positive value when the induction vector points from the rotor to the stator.

The total current in the stator winding is schematized by a linear distribution of current on the inner circumference of the stator. This distribution is also referred to as electrical load. In the stator reference frame, it is indicated by:

$$K_{\mathrm{s}}(\theta_{\mathrm{s}}) = \hat{K}_{\mathrm{s}} \cos(\theta_{\mathrm{s}} - \alpha_i) \tag{4.2}$$

The angle α_i represents the phase of the current. The positive sign indicates current from the sheet towards the reader $\odot$, while negative sing indicates current from the reader towards the sheet $\otimes$.

The peak electric load is given by:

$$\hat{K}_{\mathrm{s}} = \frac{m k_{\mathrm{w}} N_{\mathrm{s}} \hat{I}_{\mathrm{s}}}{\pi D_{\mathrm{s}}} \tag{4.3}$$

where m is the number of phase, k_s the winding factor, N_{s} the number of conductors per phase, D_{s} the inner stator diameter while $\hat{I}_{\mathrm{s}}$ is the peak stator current.

It is possible to refer both the flux distribution and the electric distribution to the same reference frame, therefore obtaining:

$$B_{\mathrm{g}}(\theta_{\mathrm{s}}) = \hat{B}_{\mathrm{g}} \cos(\theta_{\mathrm{s}} - \theta_{\mathrm{m}}) \tag{4.4}$$

with $\theta_{\mathrm{s}} = \theta_{\mathrm{r}} + \theta_{\mathrm{m}}$.

4.1.1 Electromagnetic force density

The current density $K_{\mathrm{s}}(\theta_{\mathrm{s}})$ and the magnetic flux density $B_{\mathrm{g}}(\theta_{\mathrm{s}})$ are perpendicular to each other. Applying the Lorentz force, the electromagnetic force density $f_{\mathrm{em}}(\theta_{\mathrm{s}})$ is obtained, with units of $\mathrm{N/m^2}$.

$$\begin{aligned}
f_{\mathrm{em}}(\theta_{\mathrm{s}}) &= K_{\mathrm{s}}(\theta_{\mathrm{s}}) B_{\mathrm{g}}(\theta_{\mathrm{s}}) && (4.5)\\
&= \hat{K}_{\mathrm{s}} \cos(\theta_{\mathrm{s}} - \alpha_i) \hat{B}_{\mathrm{g}} \cos(\theta_{\mathrm{s}} - \theta_{\mathrm{m}}) && (4.6)\\
&= \hat{K}_{\mathrm{s}} \hat{B}_{\mathrm{g}} \left[\cos(\theta_{\mathrm{s}} - \alpha_i) \cos(\theta_{\mathrm{s}} - \theta_{\mathrm{m}})\right] && (4.7)\\
&= \frac{\hat{K}_{\mathrm{s}} \hat{B}_{\mathrm{g}}}{2} \left[\cos(2\theta_{\mathrm{s}} - \alpha_i - \theta_{\mathrm{m}}) + \cos(\theta_{\mathrm{m}} - \alpha_i)\right] && (4.8)
\end{aligned}$$

The developed average force density is given by:

$$\begin{aligned}
< f_{\mathrm{em}} > &= \frac{1}{2\pi} \int_0^{2\pi} f(\theta_{\mathrm{s}}) d\theta_{\mathrm{s}}\\
&= \frac{\hat{K}_{\mathrm{s}} \hat{B}_{\mathrm{g}}}{4\pi} \int_0^{2\pi} \left[\cos(2\theta_{\mathrm{s}} - \alpha_i - \theta_{\mathrm{m}}) + \cos(\theta_{\mathrm{m}} - \alpha_i)\right] d\theta_{\mathrm{s}}
\end{aligned}$$

The first term in the integral is a periodic quantity, so its average value is zero. The second term is a constant with respect to the integration variable and can be taken out of the integral sign. Therefore the following value is obtained:

$$< f_{\mathrm{em}} >= \frac{\hat{K}_{\mathrm{s}}\hat{B}_{\mathrm{g}}}{2}\cos(\theta_{\mathrm{m}} - \alpha_i)$$

The maximum value of the force density is found when $\cos(\theta_{\mathrm{m}} - \alpha_i) = 1$, or when $\theta_{\mathrm{m}} = \alpha_i$. With the notation adopted, this corresponds to having the electrical load distribution produced by the stator superimposed on the magnetic induction distribution produced by the rotor [12].

4.1.2 Electromagnetic torque

The electromagnetic torque is obtained by multiplying the force density by the air-gap surface area, and then by the inner radius of the stator, resulting in:

$$T_{\mathrm{em}} = \frac{\pi}{4}D_{\mathrm{s}}^2 L_{\mathrm{stk}}\hat{K}_{\mathrm{s}}\hat{B}_{\mathrm{g}} \tag{4.9}$$

where L_{stk} is the axial length of the machine.

The equation (4.9) is the fundamental relationship for the design of rotating electrical machines. It relates:

- the electromechanical torque of the machine, which is usually a design specification;
- the required volume, measured at the air gap, where the electromagnetic conversion takes place;
- the two loads of the machine: the magnetic load $\hat{B}_{\mathrm{g}}$ and the electrical load $\hat{K}_{\mathrm{s}}$.

It is observed that the dimensions of the machine are dependent on the torque it must generate. There is no dependency on the rotational speed, and consequently, not on the power either. Machines with the same power rating may exhibit vastly different sizes if they operate at different speeds.

Furthermore, it is observed that the machine's dimensions become smaller as the magnetic and electrical loads increase. However, an increase in these loads is accompanied by higher losses, necessitating an improvement in the cooling system accordingly [9].

4.2 Design specifications

Since the motor is intended for use in a test bench, a relative low-power motor has been designed to meet general operational requirements. The design parameters have been selected with the aim of achieving efficiency and cost-effectiveness without specific constraints. The design specifications for the PM synchronous motor are arbitrarily chosen and are summarized in Table 4.1.

Description	Symbol	Value	Unit
Power	P_{n}	10	kW
Speed	n	1000	rpm
Frequency	f	150	Hz
Voltage	V_{n}	400	V
Overload current	I_{OL}	$1.25 I_{\mathrm{n}}$	A
Number of phase	m	5	-
Number of slot	Q	20	-
Number of pole	$2p$	18	-

Table 4.1 – Design specifications

4.2.1 Preliminary calculations

The design for a general motor is based on the value of the output nominal torque T_{N}. The nominal speed of the motor in rad/s is equal to:

$$\omega_{\mathrm{m}} = \frac{\omega_{\mathrm{m}}^{\mathrm{e}}}{p} = \frac{2\pi f}{p} = 104.72\,\mathrm{rad/s} \tag{4.10}$$

The nominal torque is equal to:

$$T_{\mathrm{N}} = \frac{P_N}{\omega_{\mathrm{m}}} = 95.5\,\mathrm{Nm} \tag{4.11}$$

Regarding the winding connection, a star connection has been chosen in order to avoid the circulation of 5-th harmonic currents when the motor is fed by the 5-phase inverter. The winding voltage, considering a star voltage of $V = 325\,\mathrm{V}$ and considering a drop voltage of $\Delta V = 5\%$ due to restive component, results in $E = 309\,\mathrm{V}$.

4.2.2 Considerations on the permanent magnet

The magnet used for the PMs is sintered neodymium (NeFeB) magnet N42H. The specification data from the magnet data sheet A.2 are summarized in Table 4.2. The reference temperature is set equal to $T_{\mathrm{ref}} = 20\,^{\circ}\mathrm{C}$.

The relative permeability of the permanent magnet is the ratio of the residual magnetic flux density and the intrinsic coercivity field:

$$\mu_{\mathrm{rec}} = \frac{B_{\mathrm{rem}}^{*}}{\mu_0 H_{\mathrm{cB}}^{*}} = 1.057 \tag{4.12}$$

Description	**Symbol**	**Value**	**Unit**
Residual magnetic flux density	B^*_{rem}	1.3	T
Coercivity Field	H^*_{cB}	979	kA/m
Intrinsic Coercivity Field	H^*_{cJ}	1353	kA/m
Maximum Energy Density	BH^*_{max}	330	kJ/m^3
Temperature Coefficient for B^*_{rem}	$\Delta B_{\mathrm{rem}}/\Delta T$	-0.12	%/K
Temperature Coefficient for H^*_{cJ}	$\Delta H_{\mathrm{cJ}}/\Delta T$	-0.57	%/K
Maximum Temperature	T_{max}	150	°C
Electrical Resistivity	ρ^*_{pm}	0.150	$\Omega\,\mathrm{m}$

Table 4.2 – Permanent magnet specification

For the permanent magnet, data are calculated at the working temperature, which can be cautiously assumed to be close to $T_{\mathrm{w}} = 120°$. Therefore, by defining the thermal gradient as $\Delta T = T_{\mathrm{w}} - T_{\mathrm{ref}}$, it is possible to evaluate the residual magnetic flux density at working temperature T_{w} as:

$$B_{\mathrm{rem}} = B^*_{\mathrm{rem}}\left(1 + \frac{\Delta B_{\mathrm{rem}}}{\Delta T}(T_{\mathrm{w}} - T_{\mathrm{ref}})\right) = 1.144\,\mathrm{T} \tag{4.13}$$

The correspondent coercivity field at the working temperature is therefore equal to:

$$H_{\mathrm{cB}} = \frac{B_{\mathrm{rem}}}{\mu_0 \mu_{\mathrm{rec}}} = 861.3\,\mathrm{kA/m} \tag{4.14}$$

The magnetic field at the knee is estimated from the value of the intrinsic coercivity field H_{cJ} and results in the following:

$$|H_{\mathrm{knee}}| \approx H_{\mathrm{cJ}} = H^*_{\mathrm{cJ}}\left(1 + \frac{\Delta H_{\mathrm{cJ}}}{\Delta T}(T_{\mathrm{w}} - T_{\mathrm{ref}})\right) = 581.8\,\mathrm{kA/m} \tag{4.15}$$

The corresponded flux density at the knee point is:

$$B_{\mathrm{knee}} = B_{\mathrm{rem}} + \mu_{\mathrm{rec}}\mu_0 H_{\mathrm{knee}} = 0.371\,\mathrm{T} \tag{4.16}$$

In order to continue the design process, it is necessary to evaluate the air gap flux density $\hat{B}_{\mathrm{g}}$. The relationship linking the magnetic flux density at the air gap B_{g} and the residual magnetic flux density of the magnet B_{rem} with the geometry of the air gap g'' and the thickness of the magnet t_{m} is as follows:

$$\frac{B_{\mathrm{g}}}{B_{\mathrm{rem}}} = \frac{1}{1 + \frac{\mu_{\mathrm{rec}} g''}{t_{\mathrm{m}}}} \tag{4.17}$$

By observing (4.17), it becomes apparent that excessively increasing the thickness of the magnet t_{m} relative to the air gap g'' offers minimal advantages, as depicted in Fig. 4.2. Beyond a certain ratio, the incremental gain in magnetic flux density is negligible. Therefore, a good approach is to select the air gap flux density with a balance between flux density magnitude B_{g} and magnet thickness t_{m}. This ensures optimal performance without over sizing the magnet.

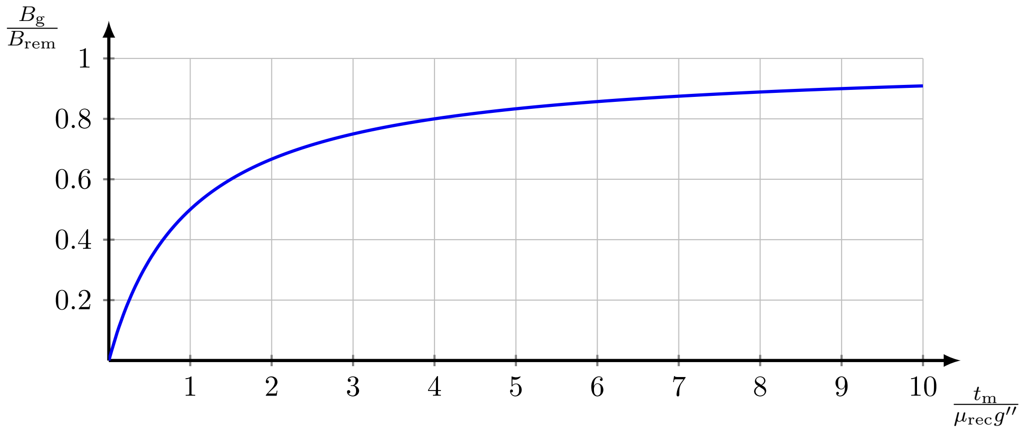

Figure 4.2 – Flux density ratio $B_\mathrm{g}/B_\mathrm{rem}$ as a function of the magnet width $t_\mathrm{m}/(\mu_\mathrm{rec} g'')$

Therefore, is advantageous to adopt an air gap flux density in the follwing range:

$$B_{g0} \approx (0.75 - 0.8) B_\mathrm{rem} \tag{4.18}$$

Since the motor has to be used in conjunction with the third harmonic, a cautionary value of $B_\mathrm{g} = 0.75 \cdot B_\mathrm{rem}$ is chosen. Therefore the air gap flux density is equal to:

$$B_\mathrm{g} = 0.75 \cdot B_\mathrm{rem} = 0.858\,\mathrm{T} \tag{4.19}$$

From the demagnetization curve of the magnet, the flux density corresponds to:

$$H_\mathrm{m} = \frac{B_\mathrm{pm} - B_\mathrm{rem}}{\mu_\mathrm{rec} \mu_0} = -215.3\,\mathrm{kA/m} \tag{4.20}$$

where $B_\mathrm{pm} \approx B_\mathrm{g}$.

In order to avoid irreversible demagnetization of the magnets, it is required to stay away from the the knee of the characteristic of demagnetization, even when the motor is working at the overloaded point. A safety margin of $k_\mathrm{sic} = 2$ is chosen at the nominal operating point, when the motor is supplied with the rated current I_n. When the motor is fed with the overload current I_OL the safety margin is equal to $k'_\mathrm{sic} = 1.25$. It is possible to define ΔH_n as the field variation due to the nominal load, ΔH_OL as the field variation due to the overload, and ΔH_smagn as the magnetic field variation that leads to the demagnetization of the magnet, since the knee of the magnetization characteristic is reached. In other words, the distance between no load operation and irreversible demagnetization is divided into four parts. It is possible to define the margin coefficient as:

$$k_\mathrm{sic} = \frac{\Delta H_\mathrm{smagn}}{\Delta H_\mathrm{n}} \tag{4.21}$$

The field variation that leads to the demagnetization of the magnet is:

$$\Delta H_\mathrm{smagn} = H_\mathrm{knee} - |H_\mathrm{m}| = 366.5\,\mathrm{kA/m} \tag{4.22}$$

Using equation (4.21), it is possible to evaluate the field variation due to the nominal load:

$$\Delta H_{\mathrm{n}} = \frac{\Delta H_{\mathrm{smagn}}}{k_{\mathrm{sic}}} = 146.6\,\mathrm{kA/m} \tag{4.23}$$

At this point is possible to evaluate the flux density variation at the air gap due to the armature reaction.

$$\Delta B = \mu_{\mathrm{rec}}\mu_0 \Delta H_{\mathrm{n}} = 0.195\,\mathrm{T} \tag{4.24}$$

Sizing of the magnet

In this subsection the electric load $\hat{K}_{\mathrm{s}}$, the interior diameter of the stator, and the thickness of the magnet are calculated. The air gap is set to $g = 0.5 + 0.3 = 0.8\,\mathrm{mm}$, considering the teeth to magnets distance and the carbon fiber composite sleeve thickness. Then, precautionary Carter coefficient and no load saturation coefficient are assumed equal to $k_{\mathrm{cart}} = 1.05$ and $k_{\mathrm{sat}} = 1.15$, respectively. Therefore a figurative air gap of $g'' = k_{\mathrm{cart}}k_{\mathrm{sat}}g = 0.966\,\mathrm{mm}$ is obtained. It is possible to evaluate the thickness of the magnet by using the formula in (4.17):

$$t_{\mathrm{m}} = \frac{\mu_{\mathrm{rec}} g''}{\frac{B_{\mathrm{rem}}}{B_{\mathrm{g}}} - 1} = 3.05\,\mathrm{mm} \tag{4.25}$$

In section 3.2.1 the coverage of a single magnet over the pole pitch τ_p has been assumed equal to $2\alpha_m^e = 180°$. Therefore the mechanical angle of the single permanent magnet is $\alpha_m = 180/p = 20°$. Considering only the flux generated by the fundamental harmonic, therefore the magnetic flux density at the air gap is:

$$\hat{B}_{\mathrm{g},1} = \frac{4}{\pi} B_{\mathrm{g}} \sin \alpha_m^e = 1.092\,\mathrm{T} \tag{4.26}$$

The the air gap density of the third harmonic component is equal to:

$$\hat{B}_{\mathrm{g},3} = \frac{4}{3\pi} B_{\mathrm{g}} \sin(3\alpha_m^e) = 0.34\,\mathrm{T} \tag{4.27}$$

4.2.3 Sizing estimation

Utilizing the equation (4.9) it is possible to express the specific torque of a generic motor as a function of the geometrical values D_{s}, L_{stk}, of the peak electric load $\hat{K}_{\mathrm{s}}$ and the peak magnetic flux density at the air gap $\hat{B}_{\mathrm{g}}$.

$$T_{\mathrm{N}} = \frac{\pi}{4} D_{\mathrm{s}}^2 L_{\mathrm{stk}} \hat{B}_{\mathrm{g}} \hat{K}_{\mathrm{s}} \tag{4.28}$$

In FSCW machine it's advantageous to have a larger stator inner diameter D_{s} and a reduced stack length L_{stk}, since it minimizes the length of the winding and therefore the copper losses. By setting the ratio between the inner diameter of the stator D_{s} and the axial length of the stack L_{stk} equal to $L_{\mathrm{stk}}/D_{\mathrm{s}} = 0.4$, and by expressing the variation of magnetic flux density at the air gap due to the armature effect as

$$\Delta B = \mu_0 \frac{\hat{K}_{\mathrm{s}} D_{\mathrm{s}}}{2p} \frac{1}{g'' + \frac{t_{\mathrm{m}}}{\mu_{\mathrm{rec}}}} \tag{4.29}$$

it is possible to build a system of three equations:

$$\begin{cases} T_{\mathrm{N}} = \frac{\pi}{4} D^2 L_{\mathrm{stk}} \hat{B}_{\mathrm{g}} \hat{K}_{\mathrm{s}} \\ \\ \Delta B = \mu_0 \frac{\hat{K}_{\mathrm{s}} D_{\mathrm{s}}}{2p} \frac{1}{g'' + \frac{t_{\mathrm{m}}}{\mu_{\mathrm{rec}}}} \\ \\ \frac{L_{\mathrm{stk}}}{D_{\mathrm{s}}} = 0.4 \end{cases} \tag{4.30}$$

The system final results are:

$$\begin{cases} D_{\mathrm{s}} = 160\,\mathrm{mm} \\ \\ L_{\mathrm{stk}} = 64.5\,\mathrm{mm} \\ \\ \hat{K}_{\mathrm{s}} = 67.4\,\mathrm{kA/m} \end{cases} \tag{4.31}$$

In this specific case, $\hat{K}_{\mathrm{s}}$ has a relative high value but it is still in the suggested range of:

$$\hat{K}_{\mathrm{s}} = 30 - 100\mathrm{kA/m} \tag{4.32}$$

4.2.4 Stator design

Since the number of slots is a fix parameter, it is possible to evaluate the tooth pitch:

$$p_{\mathrm{s}} = \frac{\pi D_{\mathrm{s}}}{Q} = 25.13\,\mathrm{mm} \tag{4.33}$$

The maximum magnetic flux density at the air gap due to the interaction between the nominal current and the permanent magnet is equal to:

$$B_{\mathrm{max}} = B_{\mathrm{g}} + \Delta B = 1.053\,\mathrm{T} \tag{4.34}$$

With a deliberately set value of magnetic flux density in the tooth of $B_{\mathrm{t}} = 1.65\,\mathrm{T}$ and an iron package factor of $k_{\mathrm{pack}} = 0.98$, it is possible with the Gauss theorem to evaluate the tooth width:

$$w_{\mathrm{t}} = p_{\mathrm{s}} \frac{B_{\mathrm{max}}}{B_{\mathrm{t}} k_{\mathrm{pack}}} = 16\,\mathrm{mm} \tag{4.35}$$

The peak fundamental flux per pole is equal to:

$$\hat{\Phi}_{\mathrm{p}} = \hat{B}_{\mathrm{g}} \frac{D_{\mathrm{s}} L_{\mathrm{stk}} k_{\mathrm{pack}}}{p} = 1.252\,\mathrm{mWb} \tag{4.36}$$

Then, since the value of the winding voltage is equal to $E \approx 310\,\mathrm{V}$, it is possible to estimate the number of conductors per phase:

$$N_\mathrm{s} = \frac{E}{\frac{\pi}{\sqrt{2}} k_\mathrm{w} \Phi_p f} \approx 772 \tag{4.37}$$

The number of conductors per phase is set to $N_\mathrm{s} = 768$, in order not to have fractional values. Considering the winding factor equal to $k_\mathrm{w} = 0.9635$, the induced voltage is the equal to:

$$E = \frac{\pi}{\sqrt{2}} k_\mathrm{w} \Phi_p f N_\mathrm{s} = 308.7\,\mathrm{V} \tag{4.38}$$

Therefore it is possible to evaluate the nominal current by using the definition of peak electric loading (4.3).

$$I_\mathrm{n} = \frac{\hat{K}_\mathrm{s}}{\sqrt{2}} \frac{\pi D_\mathrm{s}}{m k_\mathrm{w} N_\mathrm{s}} = 6.48\,\mathrm{A} \tag{4.39}$$

By choosing $n_\mathrm{pp} = 1$ parallel path, the number of effective conductors in a slot is:

$$N_\mathrm{c} = \frac{N_\mathrm{s} m n_\mathrm{pp}}{Q} = 192 \tag{4.40}$$

The number of effective conductors in a slot is defined also as $N_\mathrm{c} = n_\mathrm{layer} n_\mathrm{turn}$, where $n_\mathrm{layer} = 4$ is the number of the layer in the winding and $n_\mathrm{turn} = 48$ is the number of turn in a coil. Assuming a stator current density equal to $J_\mathrm{s} = 5.5\,\mathrm{A/mm^2}$, the section of the conductor is equal to:

$$S_\mathrm{c} = \frac{I_\mathrm{n}/n_\mathrm{pp}}{J_\mathrm{s}} = 1.178\,\mathrm{mm}^2 \tag{4.41}$$

Therefore the section occupied by the copper is:

$$S_\mathrm{Cu} = N_\mathrm{c} S_\mathrm{c} = 226.2\,\mathrm{mm}^2 \tag{4.42}$$

In [3], a novel core structure called *joint-lapped core* is introduced for a permanent magnet motor. This innovative manufacturing method allows the core to be easily deformed into a shape conducive to winding, enabling precise wire alignment and achieving high winding fill factor k_fill. Therefore in FSCW it is possible to achieve winding fill factor of $k_\mathrm{fill} = 0.75$. As a consequence, the utilization of this method enables to reach high efficiency in FSCW.

It is possible then to evaluate the slot area as:

$$S_\mathrm{slot} = \frac{S_\mathrm{Cu}}{k_\mathrm{fill}} = 301.6\,\mathrm{mm}^2 \tag{4.43}$$

The dimensions of the slot can be approximated by considering it as a trapezoid. A general and indicative equation for calculating the height of the trapezoidal surface is utilized:

$$h_\mathrm{s}^2 + \left(D_\mathrm{s} - w_\mathrm{t}\frac{Q}{\pi}\right) h_\mathrm{s} - \left(S_\mathrm{slot}\frac{Q}{\pi}\right) = 0 \tag{4.44}$$

The result of the calculations is $h_\mathrm{s} = 24.25\,\mathrm{mm}$. The slot geometrical results are summarized in Table 4.3.

Table 4.3 – Dimensions of the slot

Description	Symbol	Value	Unit
Slot height	h_s	24.25	mm
Tooth width	w_t	16	mm
Slot opening width	w_so	1.6	mm
Slot opening height	h_so	1.2	mm
Wedge height	h_wed	2.2	mm

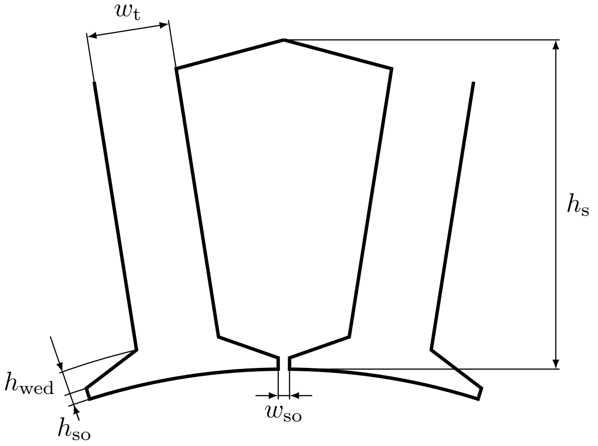

Figure 4.3 – Slot of FSCW machine

The flux per pole at the air gap surface is equal to:

$$\Phi_\mathrm{p} = B_\mathrm{g}\frac{\pi D_\mathrm{s}}{2p}L_\mathrm{stk}k_\mathrm{pack} = 1.514\,\mathrm{mWb} \tag{4.45}$$

The flux in the back iron is equal to half the flux at the air gap surface, therefore $\Phi_\mathrm{bi} = \Phi_\mathrm{p}/2$. By assuming a flux density in the back iron equal to $B_\mathrm{bi} = 1.6\,\mathrm{T}$, the height of the back iron is equal to:

$$h'_\mathrm{bi} = \frac{\Phi_\mathrm{bi}}{B_\mathrm{bi}L_\mathrm{stk}k_\mathrm{pack}} = 7.5\,\mathrm{mm} \tag{4.46}$$

Since he slot of the machine possesses a squared shape [3], the slot height does not maintain a constant value. Therefore the overall distance from the end of the tooth to the outer diameter is $h_{bi} = 9.25\,\mathrm{mm}$. Then it is possible to calculate the stator outer diameter as:

$$D_\mathrm{e} = D_\mathrm{s} + 2h_s + 2h_{bi} = 227\,\mathrm{mm} \tag{4.47}$$

Since the stator current generates a high pole flux density, it is feasible to incorporate iron-free segments in the rotor. This modification not only reduces the amount of iron used in the machine but also optimizes iron utilization, leading to improved efficiency. For simplicity, the part of the motor between the rotor diameter and the iron-free segments is referred to as the circular crown. Essentially, it serves the same purpose as the back iron. The height of the circular crown h_{crown} between the rotor diameter and the iron-free segments is determined by imposing an average flux density of $B_{\mathrm{crown}} = 0.8\,\mathrm{T}$.

$$h_{\mathrm{crown}} = \frac{\Phi_{\mathrm{bi}}}{B_{\mathrm{crown}} L_{\mathrm{stk}} k_{\mathrm{pack}}} = 15\,\mathrm{mm} \tag{4.48}$$

The peak fundamental concatenated flux of the permanent magnet is equal to the peak fundamental flux per pole $\hat{\Phi}_{\mathrm{p}}$ multiplied by the effective number of conductors per phase $k_{\mathrm{w},1} N_{\mathrm{s}}/2$, resulting in:

$$\Lambda_{\mathrm{p}} = \Lambda_{\mathrm{m}} = k_{\mathrm{w},p} \frac{N_{\mathrm{s}}}{2} \hat{\Phi}_{\mathrm{p}} = 0.463\,\mathrm{Vs} \tag{4.49}$$

By evaluating the torque via the $\mathrm{d} - \mathrm{q}$ formula:

$$T = \frac{5}{2} p \Lambda_{\mathrm{pm}} \hat{I}_{\mathrm{N}} = 95.47\,\mathrm{Nm} \tag{4.50}$$

it can be observed that the design of the machine meets the previously determined requirements.

The Table 4.5 is provided in order to summarize the design results obtained for the FSCW motor.

Table 4.4 – Variables summary for FSCW 20-slot 18-pole, five-phase motor

Description	Symbol	Value	Unit
Power	P_{n}	10	kW
Speed	n	1000	rpm
Frequency	f	150	Hz
Voltage	V_{n}	400	V
Nominal current	I_{n}	6.48	A
Number of phase	m	5	-
Number of slot	Q	20	-
Number of pole	$2p$	18	-
Air gap length	g	0.8	mm
Stator inner diameter	D_{s}	160	mm
Stator outer diameter	D_{e}	227	mm
Stack length	L_{stk}	64.5	mm
Slot height	h_{s}	24.25	mm
Tooth width	w_{t}	16	mm
Slot opening width	w_{so}	1.6	mm
Slot opening height	h_{so}	1.2	mm
Wedge height	h_{wed}	2.2	mm

4.2.5 Concentrated winding design

Following the previous design process for the FSCW motor featuring 20 slots and 18 poles described in Section 4.2.3, a motor with 20 slots and 4 poles can be designed. This motor utilizes concentrated winding and maintains identical specifications to its predecessor. Notably, the winding fill factor assumed for calculations deviates from that of the FSCW, adopting a standard value of $k_{\mathrm{fill}} = 0.35$. Presented below is a table summarizing the machine data.

Table 4.5 – Variables summary for concentrated winding 20-slot 4-pole, five-phase motor

Description	**Symbol**	**Value**	**Unit**
Power	P_{n}	10	kW
Speed	n	1000	rpm
Frequency	f	33.333	Hz
Voltage	V_{n}	400	V
Nominal current	I_{n}	6.45	A
Number of phase	m	5	-
Number of slot	Q	20	-
Number of pole	$2p$	4	-
Air gap length	g	0.8	mm
Stator inner diameter	D_{s}	130	mm
Stator outer diameter	D_{e}	237	mm
Stack length	L_{stk}	260	mm
Slot height	h_{s}	27	mm
Tooth width	w_{t}	13	mm
Slot opening width	w_{so}	2.5	mm
Slot opening height	h_{so}	2	mm
Wedge height	h_{wed}	3.75	mm

The power density of the 20-slot, 4-pole machine with concentrated winding is noticeably lower compared to that of the 20-slot, 18-pole FSCW (Fractional Slot Concentrated Winding) machine. Specifically, the power density of the FSCW machine is more than 4 times higher than that of the concentrated winding, to be precise, 4.4 times higher. The notable difference in power density can be attributed to the FSCW design's capability to accommodate a greater number of poles, thereby necessitating a reduced air gap surface to achieve comparable torque output. Furthermore, the diminished flux per pole characteristic of FSCW machines contributes to a reduction in back iron height.

5 Modeling and control

In this chapter, the modeling of the control system is conducted. A generalization of the methodology to model an m-phase machine is performed, covering also faulty cases. Additionally, the control strategies for the machine under normal operating conditions, focusing on Maximum Torque Per Ampere (MTPA) and Third Harmonic Injection (THI), are explored. The latter strategy, Third Harmonic Injection (THI), is specifically aimed at torque enhancement.

5.1 Modeling

When modeling a multiphase machine, a mathematical transformation is applied to the physical model, ensuring that the number of variables remains consistent before and after the transformation. This transformation results in m new stator current components for an m-phase machine.

In machines with sinusoidal-field distribution, standard modeling assumptions are applied, resulting in only the first harmonic of inductance terms existing in the phase-variable model. The Clarke's decoupling transformation produces a set of m equations. Among these equations, the first pair, $\alpha - \beta$, is identical to the corresponding equations for a three-phase machine. The last equation, or the last two equations for even phase numbers, corresponds to the zero-sequence equation, similarly to a three-phase machine. In between, there are $(m-3)/2$ pairs of equations (or $(m-4)/2$ for even number of phases), introducing $(m-3)/2$ pairs of new variables known as $x - y$ components. Conceptually, the form of these $x - y$ equations resembles the zero-sequence component, since the impedance for $x - y$ stator current components essentially reflects the stator winding leakage impedance. Assuming the machine is supplied with purely sinusoidal voltages and the field is sinusoidal as well, no $x - y$ voltage components are present. Consequently, this absence extends to the stator current $x - y$ components as well [34].

Decoupling transformation matrices are available also for asymmetrical multiphase machines, leading to similar results for symmetrical machines. In the unique scenario where an m-phase winding is formed by employing k individual subphase windings, each with k isolated neutral points, the total number of equations and variables decreases to $(m - k)$ after transformation. This reduction occurs since zero-sequence components are unable to flow in any of the star-connected k windings.

For concentrated winding machines, the initial physical-variable model differs, necessitating the inclusion of higher harmonics in the inductance terms. Decoupling transformation results in $(m-1)/2$ pairs of equations, which are then subject to rotational transformation to obtain the final $\mathrm{d} - \mathrm{q}$ model.

Conversely, for FSCW permanent magnet synchronous machines, the modeling closely follows the approach used for machines with sinusoidal field distribution, expect for the absence of mutual inductance terms within the stator winding due to the winding design [34].

5.2 Five-phase machine modeling

In a generic symmetrical m-phase machine, it is always possible to simplify its representation by employing a system of m concentrated windings distributed spatially at intervals of $\gamma = \frac{2\pi}{m}$ radians. In figure 5.1 the simplified model of a five-phase machine is provided, where the displacement between two phases is equal to $\gamma = \frac{2\pi}{5}$.

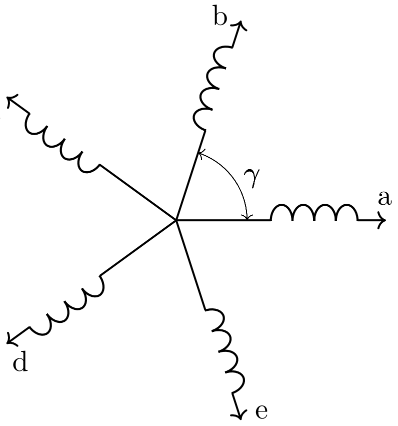

Figure 5.1 – Simplified five-phase machine model

Each simplified phase winding j of the machine can be mathematically expressed as the summation of the voltage drop due to the winding resistance $R_j i_j$ and the rate of change of flux linkage with respect to time $\frac{d\lambda_j}{dt}$, as formulated in equation (5.1).

$$v_j = R_j i_j + \frac{d\lambda_j}{dt} \tag{5.1}$$

Where $\lambda_j(i_j) = L_j(i_j)i_j$ is the flux linkage of the j-th phase winding and the variation of flux with respect to time is the induced emf: $\frac{d\lambda_j}{dt} = e_j$.

Hence, for a five-phase machine, with phase winding spatially shifted of $\gamma = \frac{2\pi}{5}$, it is possible to write the following expression:

$$v_{\text{as}} = R_{\text{as}} i_{\text{as}} + \frac{d\lambda_{\text{as}}}{dt} \tag{5.2}$$

$$v_{\text{bs}} = R_{\text{bs}} i_{\text{bs}} + \frac{d\lambda_{\text{bs}}}{dt} \tag{5.3}$$

$$v_{\text{cs}} = R_{\text{cs}} i_{\text{cs}} + \frac{d\lambda_{\text{cs}}}{dt} \tag{5.4}$$

$$v_{\text{ds}} = R_{\text{ds}} i_{\text{ds}} + \frac{d\lambda_{\text{ds}}}{dt} \tag{5.5}$$

$$v_{\text{es}} = R_{\text{es}} i_{\text{es}} + \frac{d\lambda_{\text{es}}}{dt} \tag{5.6}$$

In permanent magnet synchronous motor, if the effect of the saturation is neglected, the phase flux λ_j can alternatively be expressed as:

$$\lambda_j = \lambda_{\mathrm{pm}} + \lambda_{\mathrm{ji}} \tag{5.7}$$

where λ_{ji} is the contribute given by the self and mutual inductance, respectively L_{jj} and M_{jk}. For instance, for the phase a the following expression can be written:

$$\lambda_{\mathrm{a}i} = L_{\mathrm{aa}} i_{\mathrm{a}} + M_{\mathrm{ab}} i_{\mathrm{b}} + M_{\mathrm{ac}} i_{\mathrm{c}} + M_{\mathrm{ad}} i_{\mathrm{d}} + M_{\mathrm{ae}} i_{\mathrm{e}} \tag{5.8}$$

Given the star connection of the machine, it follows that the summation of the five currents equals zero $i_{\mathrm{a}} + i_{\mathrm{b}} + i_{\mathrm{c}} + i_{\mathrm{d}} + i_{\mathrm{e}} = 0$. It is reasonable to assume that the mutual and self inductance are equal for every phase, given the motor's isotropic nature, therefore $L_{jj} = L_{\mathrm{s}}$ and $M_{jk} = M$. Moreover it is possible to rearrange $\lambda_{\mathrm{a}i}$ as:

$$\lambda_{\mathrm{a}i} = (L_{\mathrm{s}} - M) i_{\mathrm{a}} \tag{5.9}$$

Adopting a matrix notation of the expressions in (5.6), the 5-phase system is represented as:

$$\mathbf{V_s} = \mathbf{R_s} \cdot \mathbf{I_s} + \frac{d\boldsymbol{\Lambda}_\mathbf{s}}{dt} \tag{5.10}$$

where flux matrix Λ_s is equal to:

$$\boldsymbol{\Lambda}_\mathbf{s} = \mathbf{L_{ss}} \cdot \mathbf{I_s} \tag{5.11}$$

The vector of currents, voltages and fluxes are represented as:

$$\mathbf{I_s} = [i_{\mathrm{as}}, i_{\mathrm{bs}}, i_{\mathrm{cs}}, i_{\mathrm{ds}}, i_{\mathrm{es}}] \tag{5.12}$$

$$\mathbf{V_s} = [v_{\mathrm{as}}, v_{\mathrm{bs}}, v_{\mathrm{cs}}, v_{\mathrm{ds}}, v_{\mathrm{es}}] \tag{5.13}$$

$$\boldsymbol{\Lambda}_\mathbf{s} = [\lambda_{\mathrm{as}}, \lambda_{\mathrm{bs}}, \lambda_{\mathrm{cs}}, \lambda_{\mathrm{ds}}, \lambda_{\mathrm{es}}] \tag{5.14}$$

The matrix $\mathbf{R_s}$ is a $n \times n$ diagonal matrix containing the values of each phases. Since it is reasonable to assume that the phase resistance R_j is uniform across all phases, leading to the simplification where $R_j = R_{\mathrm{s}}$ for every phase, the resistance matrix can be written as:

$$\mathbf{R_s} = \begin{bmatrix} R_{\mathrm{s}} & 0 & 0 & 0 & 0 \\ 0 & R_{\mathrm{s}} & 0 & 0 & 0 \\ 0 & 0 & R_{\mathrm{s}} & 0 & 0 \\ 0 & 0 & 0 & R_{\mathrm{s}} & 0 \\ 0 & 0 & 0 & 0 & R_{\mathrm{s}} \end{bmatrix} \tag{5.15}$$

Due to conservation of energy, $\mathbf{L_{ss}}$ is a symmetrical matrix:

$$\mathbf{L_{ss}} = \begin{bmatrix} L_{\mathrm{aa}} & M_{\mathrm{ab}} & M_{\mathrm{ac}} & M_{\mathrm{ad}} & M_{\mathrm{ae}} \\ M_{\mathrm{ba}} & L_{\mathrm{bb}} & M_{\mathrm{bc}} & M_{\mathrm{bd}} & M_{\mathrm{be}} \\ M_{\mathrm{ca}} & M_{\mathrm{cb}} & L_{\mathrm{cc}} & M_{\mathrm{cd}} & M_{\mathrm{ce}} \\ M_{\mathrm{da}} & M_{\mathrm{db}} & M_{\mathrm{dc}} & L_{\mathrm{dd}} & M_{\mathrm{de}} \\ M_{\mathrm{ea}} & M_{\mathrm{eb}} & M_{\mathrm{ec}} & M_{\mathrm{ed}} & L_{\mathrm{ee}} \end{bmatrix} \tag{5.16}$$

Adopting the same logic used to obtain (5.9), it becomes feasible to reformulate the inductance matrix as:

$$\mathbf{L_{ss}} = \begin{bmatrix} L_\mathrm{s} & M & M & M & M \\ M & L_\mathrm{s} & M & M & M \\ M & M & L_\mathrm{s} & M & M \\ M & M & M & L_\mathrm{s} & M \\ M & M & M & M & L_\mathrm{s} \end{bmatrix} \tag{5.17}$$

When modeling the concentrated winding machine and the FSCW machine, both the fundamental and third harmonic components of the winding functions are considered. Therefore, it is possible to express the Fourier series of the winding function for phase j as [41]:

$$N_j(\varphi) = \frac{4}{\pi}\frac{N_\mathrm{s}}{2p}\left(\cos(\varphi) - \frac{1}{3}\cos(3\varphi)\right) = N_{\mathrm{s},1} + N_{\mathrm{s},3} \tag{5.18}$$

The self L_s and mutual M inductances of the stator winding phases can be computed by using the corresponding winding functions as:

$$L_\mathrm{s} = \frac{\mu_0 r l}{g}\pi N_{\mathrm{s},1}^2 + \frac{\mu_0 r l}{g}\pi N_{\mathrm{s},3}^2 = L_{\mathrm{s},1} + L_{\mathrm{s},3} \tag{5.19}$$

$$M = \cos\left(\frac{4\pi}{5}\right) L_{\mathrm{s},1} + \cos\left(3\frac{4\pi}{5}\right) L_{\mathrm{s},3} \tag{5.20}$$

5.2.1 Transformation

Applying the general Clarke transformation to a five-phase machine enables the conversion of quantities from the stator reference s frame to the orthogonal $\alpha - \beta$ reference frame. This transformation facilitates a more compact representation of the system's variables and simplifies the analysis and control of the machine.

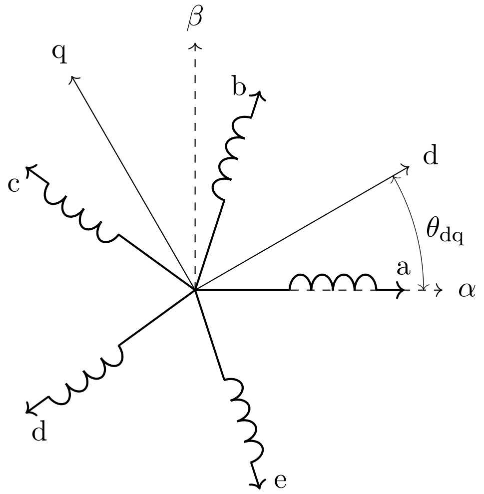

Figure 5.2 – $\alpha - \beta$ and d – q reference frame

In Fig. 5.2, the simplified model of a five-phase machine is depicted alongside the $\alpha - \beta$ and $\mathrm{d} - \mathrm{q}$ reference frames. It is important to note that, since the analyzed machine has five phases, the Clark transformation produces a five-dimensional orthogonal space. Therefore, for simplicity, only a two-dimensional representation of the five-dimensional orthogonal space is considered.

The specific Clark matrix for a symmetrical five-phase system is [32]:

$$\mathbf{C} = \frac{2}{5} \begin{bmatrix} 1 & \cos(\gamma) & \cos(2\gamma) & \cos(3\gamma) & \cos(4\gamma) \\ 0 & \sin(\gamma) & \sin(2\gamma) & \sin(3\gamma) & \sin(4\gamma) \\ 1 & \cos(3\gamma) & \cos(6\gamma) & \cos(9\gamma) & \cos(12\gamma) \\ 0 & \sin(3\gamma) & \sin(6\gamma) & \sin(9\gamma) & \sin(12\gamma) \\ \frac{1}{2} & \frac{1}{2} & \frac{1}{2} & \frac{1}{2} & \frac{1}{2} \end{bmatrix} \tag{5.21}$$

where $\gamma = \frac{2\pi}{5}$ is the displacement in radians between the phases. Since the Clark matrix is orthogonal, it is possible to evaluate the inverse of the matrix as:

$$\mathbf{C}^{-1} = \frac{2}{5}\mathbf{C}^{T} \tag{5.22}$$

Evaluating the inverse of a matrix as the transposed original matrix leads to a simplification in the control algorithm and lower computational cost. Indeed, it is well known that computing the inverse of a matrix is computationally expensive and may introduce numerical instability, particularly for large matrices.

Applying the Clark matrix transformation to the current vector in the stator reference frame s yields the following transformed current vector:

$$\begin{bmatrix} v_{\alpha} \\ v_{\beta} \\ v_{x} \\ v_{y} \\ v_{0} \end{bmatrix} = \frac{2}{5} \begin{bmatrix} 1 & \cos(\gamma) & \cos(2\gamma) & \cos(3\gamma) & \cos(4\gamma) \\ 0 & \sin(\gamma) & \sin(2\gamma) & \sin(3\gamma) & \sin(4\gamma) \\ 1 & \cos(3\gamma) & \cos(6\gamma) & \cos(9\gamma) & \cos(12\gamma) \\ 0 & \sin(3\gamma) & \sin(6\gamma) & \sin(9\gamma) & \sin(12\gamma) \\ \frac{1}{2} & \frac{1}{2} & \frac{1}{2} & \frac{1}{2} & \frac{1}{2} \end{bmatrix} \begin{bmatrix} v_{\mathrm{as}} \\ v_{\mathrm{bs}} \\ v_{\mathrm{cs}} \\ v_{\mathrm{ds}} \\ v_{\mathrm{es}} \end{bmatrix} \tag{5.23}$$

After that is possible to define the Park or $\mathrm{d} - \mathrm{q}$ matrix as:

$$\mathbf{P} = \begin{bmatrix} \cos(\theta_{\mathrm{dq}}) & \sin(\theta_{\mathrm{dq}}) & 0 & 0 & 0 \\ -\sin(\theta_{\mathrm{dq}}) & \cos(\theta_{\mathrm{dq}}) & 0 & 0 & 0 \\ 0 & 0 & \cos(3\theta_{\mathrm{dq}}) & \sin(3\theta_{\mathrm{dq}}) & 0 \\ 0 & 0 & -\sin(3\theta_{\mathrm{dq}}) & \cos(3\theta_{\mathrm{dq}}) & 0 \\ 0 & 0 & 0 & 0 & 1 \end{bmatrix} \tag{5.24}$$

where θ_{dq} the angle of rotation between the $\alpha - \beta$ reference frame and $\mathrm{d} - \mathrm{q}$ reference frame, as depicted previously in fig. 5.2.

The matrix product of the Clark and Park transformations results in a matrix that converts quantities from the stator reference frame (s) to the $\mathrm{d} - \mathrm{q}$ frame. This transformation is defined as [41]:

$$\mathbf{T} = \frac{2}{5} \begin{bmatrix} \cos(\theta_{\mathrm{dq}}) & \cos(\theta_{\mathrm{dq}} - \gamma) & \cos(\theta_{\mathrm{dq}} - 2\gamma) & \cos(\theta_{\mathrm{dq}} - 3\gamma) & \cos(\theta_{\mathrm{dq}} - 4\gamma) \\ -\sin(\theta_{\mathrm{dq}}) & -\sin(\theta_{\mathrm{dq}} - \gamma) & -\sin(\theta_{\mathrm{dq}} - 2\gamma) & -\sin(\theta_{\mathrm{dq}} - 3\gamma) & -\sin(\theta_{\mathrm{dq}} - 4\gamma) \\ \cos(3(\theta_{\mathrm{dq}})) & \cos(3(\theta_{\mathrm{dq}} - \gamma)) & \cos(3(\theta_{\mathrm{dq}} - 2\gamma)) & \cos(3(\theta_{\mathrm{dq}} - 3\gamma)) & \cos(3(\theta_{\mathrm{dq}} - 4\gamma)) \\ -\sin(3(\theta_{\mathrm{dq}})) & -\sin(3(\theta_{\mathrm{dq}} - \gamma)) & -\sin(3(\theta_{\mathrm{dq}} - 2\gamma)) & \sin(3(\theta_{\mathrm{dq}} - 3\gamma)) & -\sin(3(\theta_{\mathrm{dq}} - 4\gamma)) \\ \frac{1}{2} & \frac{1}{2} & \frac{1}{2} & \frac{1}{2} & \frac{1}{2} \end{bmatrix} \tag{5.25}$$

Applying the Clark-Park matrix transformation, also known as the dq transformation, to the current vector in the stator reference frame (s) yields the following transformed current vector:

$$\begin{bmatrix} v_{\mathrm{d}} \\ v_{\mathrm{q}} \\ v_{\mathrm{d3}} \\ v_{\mathrm{q3}} \\ v_0 \end{bmatrix} = \mathbf{T} \begin{bmatrix} v_{\mathrm{as}} \\ v_{\mathrm{bs}} \\ v_{\mathrm{cs}} \\ v_{\mathrm{ds}} \\ v_{\mathrm{es}} \end{bmatrix} \tag{5.26}$$

Where v_{d} and v_{q} represent the voltages of the fundamental harmonic in the $\mathrm{d}-\mathrm{q}$ reference frame, while v_{d3} and v_{q3} denote the voltages of the third harmonic.

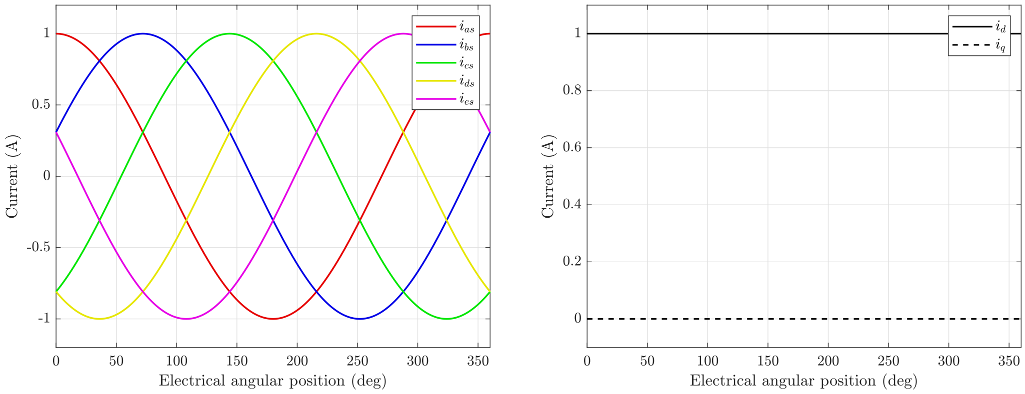

(a) Current in stationary reference frame **(b)** Current in rotating reference frame dq

Figure 5.3 – Current in healthy case

By considering only perfect sinusoidal operation and thus taking into account only the fundamental component of the flux and current, it is possible to derive the torque in the dq reference frame as follows [33]:

$$T_{\mathrm{dq}} = \frac{5}{2} p \left(\lambda_{\mathrm{d}} i_{\mathrm{q}} - \lambda_{\mathrm{q}} i_{\mathrm{d}}\right) \tag{5.27}$$

with λ_{d} and λ_{q} equal to:

$$\begin{cases} \lambda_{\mathrm{d}} = \lambda_{\mathrm{pm}} + L_{\mathrm{d}} i_{\mathrm{d}} \\ \lambda_{\mathrm{q}} = L_{\mathrm{q}} i_{\mathrm{q}} \end{cases} \tag{5.28}$$

Since the machine is a surface permanent magnet motor, $\lambda_{\mathrm{d}} = \lambda_{\mathrm{pm}}$ while $\lambda_{\mathrm{q}} = 0$, and the control in Maximum Torque Per Ampere (MTPA) gives $i_{\mathrm{d}} = 0$ and $i_{\mathrm{q}} = i_{\mathrm{n}}$ the expression (5.27) becomes [33]:

$$T_{\mathrm{dq}} = \frac{5}{2} p \lambda_{\mathrm{pm}} i_{\mathrm{n}} \tag{5.29}$$

If in the expression (5.27) the third harmonic of the flux and current is also considered, then it yiedls:

$$T_{\mathrm{dq}} = T_{\mathrm{dq1}} + T_{\mathrm{dq3}} = \frac{5}{2} p \left(\lambda_{\mathrm{pm},1} i_{\mathrm{q},1} + \lambda_{\mathrm{pm},3} i_{\mathrm{q},3}\right) \tag{5.30}$$

Therefore, from a theoretical perspective, if the value of the first harmonic current remains unchanged, the addition of the third harmonic component leads to an increase in torque.

5.3 Fault modeling

In electrical drives, various types of faults can occur, including both inverter and machine faults. Among these, the most prevalent are short circuit and open circuit faults. Short-circuit faults can manifest in phases, in inverter switches, or inter-turns within the machine while open-circuit faults may involve inverter switches, phases, or lines within the system [20], as depicted in fig. 5.4 .

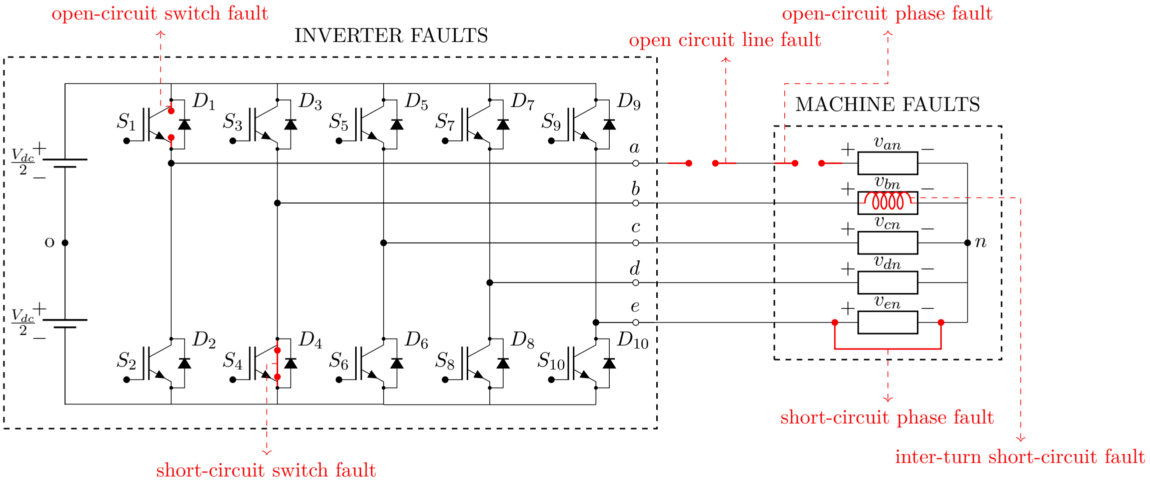

Figure 5.4 – Fault types in a five-phase drive [20]

The primary cause of electrical faults in industrial drives is often attributed to power electronics failures, which are mostly unpredictable [15]. Nonetheless, early detection of certain machine faults, such as damaged connections or inter-turn winding faults, can be achieved by observing the resulting unbalanced stator resistances. These imbalances can be identified in the initial stages using diagnostic methods, allowing for detection before they evolve into eventual open- or short-circuit faults [50].

In the thesis, only open-circuit faults (OCF) are studied. This is because, aside from power failures in power electronics, open circuits in windings are the most common and frequent faults [15]. However, it is important to note that in the case of short-circuit faults, fault-tolerant is achievable only if the machine is designed with a modular structure [4, 6] or with tooth coil winding arrangement [13]. This is due to the fact that it is necessary to have limited or zero mutual coupling between phases in order to prevent the propagation of faults to healthy phases.

When OCF occours, post-fault operation of multiphase drives is subject to certain limits to preserve system integrity. During normal operation, stator currents maintain steady-state RMS values, defined by the rated value of the drive ($I_{\mathrm{n}}^{\mathrm{pre}}$). However, after the loss of n phases due to open-circuit faults (OCF), the RMS value and waveform of stator currents can become heterogeneous. Two different approaches exist to limit post-fault currents [20]:

- *limit 1*: Post-fault currents are limited to their pre-fault RMS rated values ($I_{\mathrm{n}}^{\mathrm{post}} = I_{\mathrm{n}}^{\mathrm{pre}}$). This ensures safety by preventing device ratings from being exceeded and reducing thermal stress after the fault;

- *limit 2*: Post-fault currents can exceed pre-fault RMS rated values ($I^{\text{post}} > I^{\text{pre}}$) while maintaining pre-fault copper losses ($P_{\text{Cu}}^{\text{post}} = P_{\text{Cu}}^{\text{pre}}$). Although this allows for higher torque production, it may increase thermal stress and pose risks to motor insulation. For instance, in a five-phase motor, after an open-circuit fault occurs in one phase, the current must be increased by a factor of 1.382 to maintain the same torque output as under nominal conditions [28, 40].

The decision to adopt *limit 1*, which maintains post-fault currents at pre-fault RMS rated values, serves to enhance the operational safety of the machine. This choice prioritizes the longevity and reliability of the system by minimizing the risks associated with electrical overstress and thermal damage.

5.3.1 One-phase open-circuit fault

In this section the modeling of a generic five-phase machine under a one-phase open-circuit fault is analyzed. For simplicity permanent open-fault in the a-phase is considered, therefore the current in a-phase is considered to be zero $i_{\text{a}} = 0$.

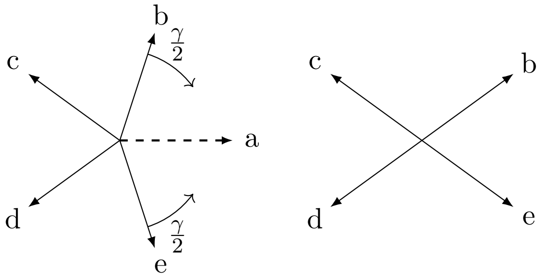

Figure 5.5 – Open-circuit fault in phase-a

With only four out of five phases capable of producing an effective MMF across the machine, the modeling and spatial distribution of the phases must be adjusted according to the type of fault. Consequently, the following constraints are established: [13]:

- each intact phase maintains identical current amplitude;
- the principle of symmetry has to be preserved after the fault;
- the total sum of currents in the remaining healthy phases must be zero.

In [13], the approach of injecting a third time-harmonic current is proposed to further reduce the fourth-order torque harmonic to zero. However, it's noteworthy that this additional current harmonic contributes to torque harmonics of both second and fourth orders, necessitating a corresponding adjustment in the fundamental current harmonic. In this study, the aforementioned method is not employed. Instead, a Reduced-Order Transformation Matrix is introduced, facilitating a simpler control approach for the motor.

In the specific case of the a-phase fault, the remaining healthy phases must be symmetrical with respect to the faulted phase. Therefore, since only the fundamental harmonic of flux-density distribution is considered [13], phases B and E are shifted of $\gamma/2$ for symmetrical purposes, as depicted in Fig. 5.5. The same principle applies even when faults occur in phases other than a-phase.

Since only the fundamental harmonic of flux-density distribution is considered, the components contributing to electromechanical energy conversion are mapped onto the $\alpha - \beta$ plane. Conversely, the components with no contribution to the torque production are distributed into the zero-sequence subspace, defined as a sub-space orthogonal to the torque-producing subspace [51]. Therefore, it is possible to simplify the Clarke and Park transformations and express the stator phase currents as functions of the direct i_{d} and quadrature i_{q} currents, resulting:

$$\begin{bmatrix} i_{\mathrm{as}} \\ i_{\mathrm{bs}} \\ i_{\mathrm{cs}} \\ i_{\mathrm{ds}} \\ i_{\mathrm{es}} \end{bmatrix} = \begin{bmatrix} 1 & 0 \\ \cos(\gamma) & \sin(\gamma) \\ \cos(2\gamma) & \sin(2\gamma) \\ \cos(3\gamma) & \sin(3\gamma) \\ \cos(4\gamma) & \sin(4\gamma) \end{bmatrix} \begin{bmatrix} \cos(\theta_{\mathrm{dq}}) & -\sin(\theta_{\mathrm{dq}}) \\ \sin(\theta_{\mathrm{dq}}) & \cos(\theta_{\mathrm{dq}}) \end{bmatrix} \begin{bmatrix} i_{\mathrm{d}}^* \\ i_{\mathrm{q}}^* \end{bmatrix} \tag{5.31}$$

where $\gamma = 2\pi/5$ for a five-phase machine, while θ_{dq} is the angle of rotation between the $\alpha - \beta$ reference frame and $\mathrm{d} - \mathrm{q}$ reference frame.

As previously explained, since there has to be a mirror principle in when the faults occurs [21], the currents in the healthy phases should be sinusoidal, and they are inter-related based on their spatial symmetry about the fault phase. Therefore, the current behavior of the remaining healthy phases can be expressed as follows:

$$\begin{cases} i_{\mathrm{bs}} &= I\cos(\theta_{\mathrm{dq}} - \gamma/2) \\ i_{\mathrm{cs}} &= I\cos(\theta_{\mathrm{dq}}) \\ i_{\mathrm{ds}} &= I\cos(\theta_{\mathrm{dq}}) \\ i_{\mathrm{es}} &= I\cos(\theta_{\mathrm{dq}} + \gamma/2) \end{cases} \tag{5.32}$$

From equation (5.32) it is evident that during fault-tolerant operation, the phasors of c-phase and d-phase remain unchanged, while those of b-phase and e-phase are shift by $-\gamma/2$ and $\gamma/2$, respectively. Using normal decoupling transformation matrices results in coupling currents. Hence, to achieve Field-Oriented Control (FOC) during fault-tolerant operation, the transformation matrices need to be redefined.

When an open-circuit fault occurs, the corresponding phase current becomes zero, reducing the motor's degrees of freedom to three. Two degrees of freedom can be allocated to a subspace defined as $\alpha - \beta$, while the remaining degree goes to another subspace defined as z. These sub-spaces must be orthogonal, and their bases must also be orthogonal to each other. The variable in the z subspace is termed the generalized zero-sequence variable. It is possible therefore to build an the following reduced-order transformation matrix [51]:

$$\mathbf{C}_{\mathrm{post}} = \begin{bmatrix} \frac{\cos(0.5\gamma)}{2.618} & \frac{\sin(0.5\gamma)}{1.381} & \frac{\sin(\gamma)}{3.618} & \frac{1}{4} \\ \frac{\cos(2\gamma)}{2.618} & \frac{\sin(2\gamma)}{1.381} & \frac{\sin(4\gamma)}{3.618} & \frac{1}{4} \\ \frac{\cos(3\gamma)}{2.618} & \frac{\sin(3\gamma)}{1.381} & \frac{\sin(6\gamma)}{3.618} & \frac{1}{4} \\ \frac{\cos(4.5\gamma)}{2.618} & \frac{\sin(4.5\gamma)}{1.381} & \frac{\sin(9\gamma)}{3.618} & \frac{1}{4} \end{bmatrix} \tag{5.33}$$

$$\mathbf{C}_{\text{post}} = \begin{bmatrix} \frac{\cos(0.5\gamma)}{2.618} & \frac{\cos(2\gamma)}{2.618} & \frac{\cos(3\gamma)}{2.618} & \frac{\cos(4.5\gamma)}{2.618} \\ \frac{\sin(0.5\gamma)}{1.381} & \frac{\sin(2\gamma)}{1.381} & \frac{\sin(3\gamma)}{1.381} & \frac{\sin(4.5\gamma)}{1.381} \\ \frac{\sin(\gamma)}{3.618} & \frac{\sin(4\gamma)}{3.618} & \frac{\sin(6\gamma)}{3.618} & \frac{\sin(9\gamma)}{3.618} \\ \frac{1}{4} & \frac{1}{4} & \frac{1}{4} & \frac{1}{4} \end{bmatrix} \tag{5.34}$$

while the inverse transformation matrix is equal to:

$$\mathbf{C}_{\text{post}}^{-1} = \begin{bmatrix} \cos(0.5\gamma) & \sin(0.5\gamma) & \sin(\gamma) & 1 \\ \cos(2\gamma) & \sin(2\gamma) & \sin(4\gamma) & 1 \\ \cos(3\gamma) & \sin(3\gamma) & \sin(6\gamma) & 1 \\ \cos(4.5\gamma) & \sin(4.5\gamma) & \sin(9\gamma) & 1 \end{bmatrix} \tag{5.35}$$

The Park matrix is then reduced to a 4 × 4 matrix, therefore yielding:

$$\mathbf{P} = \begin{bmatrix} \cos(\theta_{\text{dq}}) & \sin(\theta_{\text{dq}}) & 0 & 0 \\ -\sin(\theta_{\text{dq}}) & \cos(\theta_{\text{dq}}) & 0 & 0 \\ 0 & 0 & 1 & 0 \\ 0 & 0 & 0 & 1 \end{bmatrix} \tag{5.36}$$

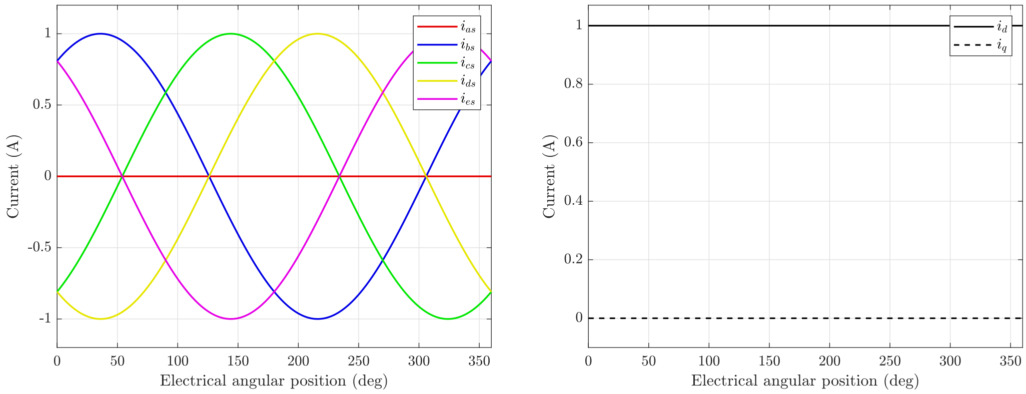

(a) Current in stationary reference frame **(b)** Current in rotating reference frame dq

Figure 5.6 – Open-circuit fault in phase-a

5.3.2 Open-circuit fault of two nonadjacent phases

When the motor experiences double-phase faults, it is reduced to having only two degrees of freedom, which can be mapped in $\alpha - \beta$ space using the transformation matrix. Let's now assume that the nonadjacent-phase open-circuit faults occur in phase-b and phase-e. As previously discussed in section in 5.3.1, in order to achieve disturbance-free operation, the healthy phase currents must adhere to specific constraints [16].

Therefore, for the specific case of nonadjacent-phase open-circuit faults occurring in phase-b and phase-e, the current in phase-c and phase-d should mirror each other with respect to the

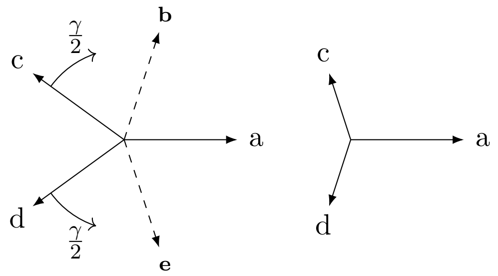

Figure 5.7 – Open-circuit fault in phase-b and phase-e

axis of phase-a. Thus, it is necessary to implement a phase shift of $-\gamma/2$ for phase-b and $\gamma/2$ for phase-d, as illustrated Fig. 5.7. In addition, the sum of healthy phase currents should be zero due to the star-connected windings.

Therefore, it is possible to express the current behavior of the remaining healthy phases as [16]:

$$\begin{cases} i_{\mathrm{as}} = I\left(i_{\mathrm{d}}\cos(\theta_{\mathrm{dq}}) + i_{\mathrm{q}}\sin(\theta_{\mathrm{dq}})\right) \\ i_{\mathrm{cs}} = 0.618 \cdot I\left(i_{\mathrm{d}}\cos(\theta_{\mathrm{dq}} - 1.5\gamma) + i_{\mathrm{q}}\sin(\theta_{\mathrm{dq}} - 1.5\gamma)\right) \\ i_{\mathrm{ds}} = 0.618 \cdot I\left(i_{\mathrm{d}}\cos(\theta_{\mathrm{dq}} + 1.5\gamma) + i_{\mathrm{q}}\sin(\theta_{\mathrm{dq}} + 1.5\gamma)\right) \end{cases} \tag{5.37}$$

where the coefficient 0.618 is evaluated from [13]:

$$-\frac{1}{2}\cos\left(\gamma - \frac{4\pi}{5}\right). \tag{5.38}$$

It is notable that phase-c and phase-d currents have the same amplitudes, but reduced since multiplied by 0.618. While phase-a current remains in the same position and its amplitude enlarges to 1.382 times.

Therefore, from equation (5.37), it is possible to express the Clark transformation as [16]:

$$\mathbf{C}_{\mathrm{post}} = \begin{bmatrix} 1.079\cos(0) & 1.746\cos(1.5\gamma) & 1.746\cos(-1.5\gamma) \\ 1.079\sin(0) & 0.553\sin(1.5\gamma) & 0.553\sin(-1.5\gamma) \\ \frac{1}{3} & \frac{1}{3} & \frac{1}{3} \end{bmatrix} \tag{5.39}$$

While the inverse matrix transformation is as follows:

$$\mathbf{C}_{\mathrm{post}}^{-1} = \begin{bmatrix} 0.618\cos(0) & 0.618\sin(0) & 1 \\ \cos(1.5\gamma) & \sin(1.5\gamma) & 1 \\ \cos(-1.5\gamma) & \sin(-1.5\gamma) & 1 \end{bmatrix} \tag{5.40}$$

Also here we can see that the inverse of the inverse original matrix $\mathbf{C}_{\mathrm{post}}^{-1}$ is not equal to the original matrix $\mathbf{C}_{\mathrm{post}}$.

The Park matrix is then reduced to a 3×3 matrix, therefore it is equal to:

$$\mathbf{P} = \begin{bmatrix} \cos(\theta_{\mathrm{dq}}) & \sin(\theta_{\mathrm{dq}}) & 0 \\ -\sin(\theta_{\mathrm{dq}}) & \cos(\theta_{\mathrm{dq}}) & 0 \\ 0 & 0 & 1 \end{bmatrix} \tag{5.41}$$

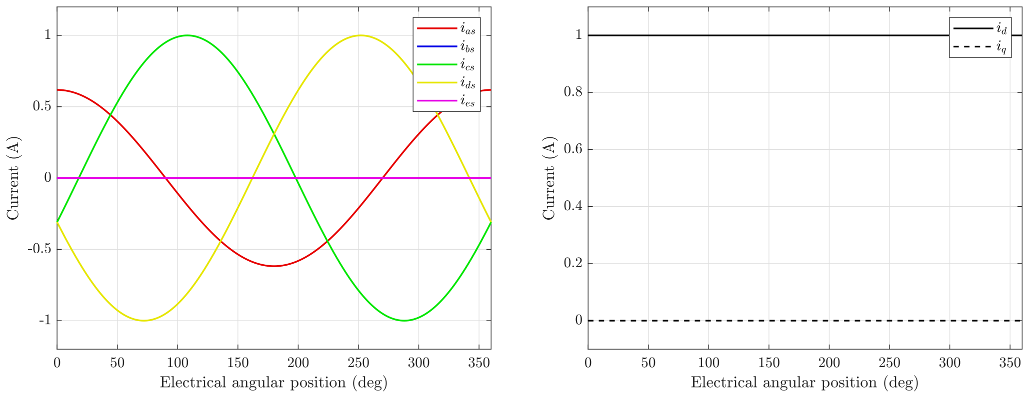

(a) Current in stationary reference frame **(b)** Current in rotating reference frame dq

Figure 5.8 – Open-circuit fault in phase-b and phase-e

5.3.3 Open-circuit fault of two adjacent phases

In this section the adjacent-phase open-circuit faults is assumed to occur in phase-c and phase-d. In order to achieve the disturbance-free operation, the healthy phase currents should in phase-b and phase-e need to satisfy the mirror symmetry principle with respect to the axis of phase-a.

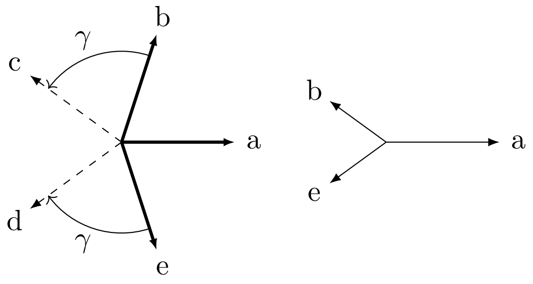

Figure 5.9 – Open-circuit fault in phase-c and phase-d

Therefore, it is necessary to implement a phase shift of γ for phase-b and γ for phase-e, as illustrated Fig. 5.9. In addition, the sum of healthy phase currents should be zero due to the star-connected windings.

Hence,the current behavior of the remaining healthy phases is equal to [16]:

$$\begin{cases} i_{\mathrm{as}} = I\left(i_{\mathrm{d}}\cos(\theta_{\mathrm{dq}}) + i_{\mathrm{q}}\sin(\theta_{\mathrm{dq}})\right) \\ i_{\mathrm{bs}} = 0.618 \cdot I\left(i_{\mathrm{d}}\cos(\theta_{\mathrm{dq}} + 2\gamma) + i_{\mathrm{q}}\sin(\theta_{\mathrm{dq}} + 2\gamma)\right) \\ i_{\mathrm{es}} = 0.618 \cdot I\left(i_{\mathrm{d}}\cos(\theta_{\mathrm{dq}} - 2\gamma) + i_{\mathrm{q}}\sin(\theta_{\mathrm{dq}} - 2\gamma)\right) \end{cases} \tag{5.42}$$

By rearranging the expression (5.42) it is possible to obtain the Clark transformation matrix:

$$\mathbf{C}_{\mathrm{post}} = \begin{bmatrix} 0.667\cos(0) & 0.412\cos(2\gamma) & 0.412\cos(-2\gamma) \\ 0.667\sin(0) & 2.342\sin(2\gamma) & 2.342\sin(-2\gamma) \\ \frac{1}{3} & \frac{1}{3} & \frac{1}{3} \end{bmatrix} \tag{5.43}$$

While the inverse matrix transformation is as follows:

$$\mathbf{C}_{\text{post}}^{-1} = \begin{bmatrix} \cos(0) & \sin(0) & 1 \\ 0.618\cos(2\gamma) & 0.618\sin(2\gamma) & 1 \\ 0.618\cos(-2\gamma) & 0.618\sin(-2\gamma) & 1 \end{bmatrix} \tag{5.44}$$

The reduced order Park matrix is a 3 × 3 matrix, expressed as follows:

$$C_{\text{post}} = \begin{bmatrix} \cos\theta & \sin\theta & 0 \\ -\sin\theta & \cos\theta & 0 \\ 0 & 0 & 1 \end{bmatrix}$$

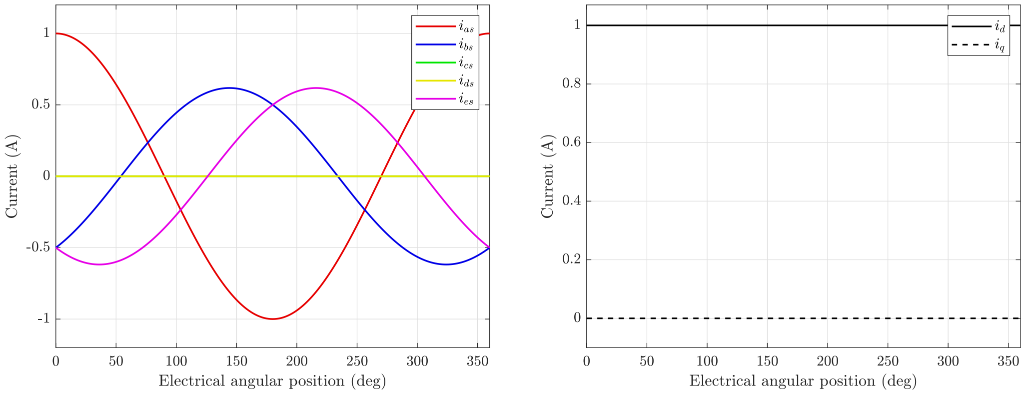

(a) Current in stationary reference frame **(b)** Current in rotating reference frame dq

Figure 5.10 – Open-circuit fault in phase-c and phase-d

5.4 Control

In this section, the Maximum Torque Per Ampere (MTPA) control strategy is employed. MTPA control aims to maximize the torque generated by the motor while minimizing the current drawn from the power supply. This optimization is achieved by adjusting the stator currents to align the resultant magnetic field vector with the rotor flux vector. Specifically, for a surface permanent magnet synchronous motor, this alignment occurs when only the quadrature current is present, leading to $i_\mathrm{q} = i_\mathrm{n}$ and $i_\mathrm{d} = 0$ [33].

5.4.1 Third harmonic injection

For a general m-phase machine, where m is an odd prime number, with a single neutral point in the star-connected stator winding, $(n - 3)$ additional degrees of freedom exit. These degrees of freedom can serve for various purposes like torque enhancement via stator current harmonic injection or multimotor drive systems with independent control having a single inverter supply. It's essential to note that these additional degrees of freedom can be allocated for only one purpose at a time. For instance, if a fault-tolerant strategy is implemented in a five-phase concentrated winding machine utilizing the third stator current harmonic injection, and a fault occurs, the strategy necessitates the discontinuation of the stator current harmonic injection [34].

In this section the utilization of extra degree of freedom for the Third harmonic injection is analyzed (HCI) or (THI). The main principle behind this method is to increase the average torque by aligning higher rotor harmonic flux, generated by the permanent magnets, with the corresponding stator harmonic flux induced by the current. By utilizing the expression (5.30), it is possible to derive a general equation (5.45) of the torque for a surface permanent magnet motor.

$$T_\mathrm{dq} = \sum_{\nu=1}^{m-3} T_{\mathrm{dq},\nu} = \sum_{\nu=1}^{m-3} \frac{m}{2} p \lambda_{\mathrm{pm},\nu} i_{\mathrm{q},\nu} \tag{5.45}$$

In a five-phase motor, the torque equation is simplified to (5.30), as only the third harmonic of the current can be injected into the stator winding. The injection of the third harmonic current can thus be represented as the combined influence of both the fundamental harmonic and the third harmonic component of the current. Considering only now a sinusoidal shape of the current, this results in:

$$i(\theta) = I_1 \sin(\theta) + I_3 \sin(\theta) \tag{5.46}$$

where I_1 and I_3 are the peak values of the first and third harmonics, respectively.

Two distinct approaches exist for injecting the third harmonic current into the stator coil: RMS and peak mode. The RMS method ensures that the root mean square (RMS) value of the current during Third Harmonic Injection (THI) remains equal to the nominal value. Consequently, this approach maximizes the torque per joule losses, as the latter remain constant. On the other hand, the peak mode pushes the output inverter current to the highest possible value. As a result, under peak mode, the resulting current during THI is limited to the peak value current experienced during normal operating conditions [29].

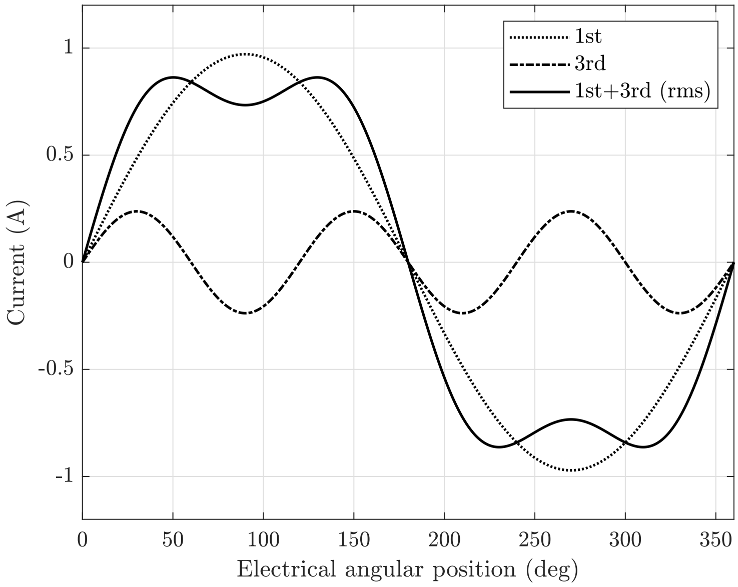

Figure 5.11 – Current under THI rms mode

During both modes, the ratio a between the first and the third harmonic current is constant and is equal to the ratio between the respective induced electromotive force [47].

$$r_3 = \frac{I_3}{I_1} = \frac{E_3}{E_1} = \frac{k_{\mathrm{w},3p} B_{\mathrm{g},3}}{k_{\mathrm{w},p} B_{\mathrm{g},1}} \tag{5.47}$$

This is done in order to maximize the torque density [48]. For the specific case of the 20-slot 18-pole FSCW with double layer the ratio is equal to $a = 0.2447$. While for the distributed winding the ratio is equal to $a = 1/3$.

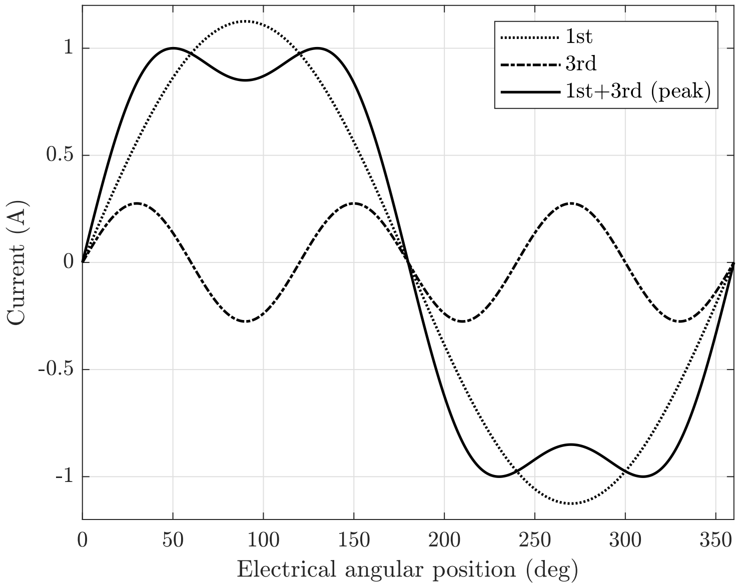

Figure 5.12 – Current under THI peak mode

In the RMS mode, the rms current can be expressed as:

$$I_\mathrm{n} = \sqrt{I^2_\mathrm{rms,1} + I^2_\mathrm{rms,3}} = \sqrt{I^2_\mathrm{rms,1} + r_3^2 I^2_\mathrm{rms,1}} \tag{5.48}$$

Thus, by defining the peak value of the first harmonic as:

$$I_1 = r_1 I_\mathrm{n} \tag{5.49}$$

we can determine the ratio between the peak of the first harmonic current and the total peak current r_1, from the equation (5.48), as:

$$r_1 = \frac{1}{\sqrt{1 + r_3^2}} \tag{5.50}$$

For the FSCW machine, this calculation yields $r_1 = 0.9713$, while for the distributed winding machine, $r_1 = 0.9487$. In a general form, considering only the sinusoidal component, the current distribution is defined as:

$$i(\theta) = r_1 I_\mathrm{peak} \sin(\theta) + r_1 r_3 I_\mathrm{peak} \sin(\theta) \tag{5.51}$$

When evaluating the ratios r_1 and r_3 during peak mode, a different approach is employed. The method involves finding the maximum of the current $i(\theta)$ as a function of r_1, while r_3 is set to the respective value, as described previously. The objective is to ensure that the peak of the combined first and third harmonic current waveform is equal to peak value during normal conditions $I_\mathrm{peak} = \sqrt{2} I_\mathrm{n}$. Therefore, it is possible to express the following functions:

$$i(\theta) = r_1 \sin(\theta) + r_1 r_3 \sin(\theta) < 1 \tag{5.52}$$

Due to the trigonometric nature of the function, an analytical solution for the maximum value of r_1 may not be feasible. Therefore, a numerical approach is necessary to search for the maximum value of r_1 within a specified range. With this iterative approach, the ratio of the first harmonic is equal to $r_1 = 1.126$ for the FSCW machine, while $r_1 = 1.061$ for the distributed winding machine.

It is noteworthy to emphasize that the RMS mode ensures consistent joule losses, given the absence of variation in the rms value of the current. Conversely, the peak mode substantially increases the peak value of the first harmonic current, consequently leading to an expected increase in torque [29].

6 Simulation

The machine is analyzed using Finite Element Method Magnetics (FEMM) in quasi-steady-state operation, with current supplied by imposing the current vector in a synchronous $\mathrm{d}-\mathrm{q}$ reference frame with the rotor. Due to planar symmetry, a 2D geometry was implemented. Consequently, the electromagnetic problem is of 2D magnetostatic type.

Finite Element Method Magnetics (FEMM) is a finite element package for solving 2D planar and axisymmetric problems in low frequency magnetics and electrostatics. The software utilizes the Finite Element Method (FEM), a numerical technique used to solve partial differential equations governing physical phenomena. In the context of electric motor simulation, FEM method discretizes the motor geometry into small elements, allowing for the numerical solution of Maxwell's equations within each element. This approach enables to accurately capture the electromagnetic fields generated within the motor, including flux distribution and torque production.

In this chapter, simulations are conducted for various winding configurations of the Fractional-Slot Concentrated Winding (FSCW) motor. Specifically, simulations are performed for FSCW motors with 1-layer, 2-layer, and 4-layer windings. Additionally, an analysis of the concentrated winding configuration is included in the study.

Emphasis is primarily placed on the analysis and simulation of the FSCW 4-layer winding configuration throughout this chapter. Consequently, unless explicitly stated otherwise, all analyses and simulations presented herein pertain specifically to the FSCW 4-layer winding.

6.1 Simulation steps

In modeling electric motors with the Finite Element Method (FEMM), several key steps are involved, such as: geometry definition, material properties assignment, mesh generation, boundary condition specification, solver configuration, and analysis with post-processing.

Geometry definition

The motor geometry, including the stator, rotor, windings, and other components is defined with the geometrical specifications evaluated in Chapter 4. The geometry serves as the basis for creating the finite element mesh.

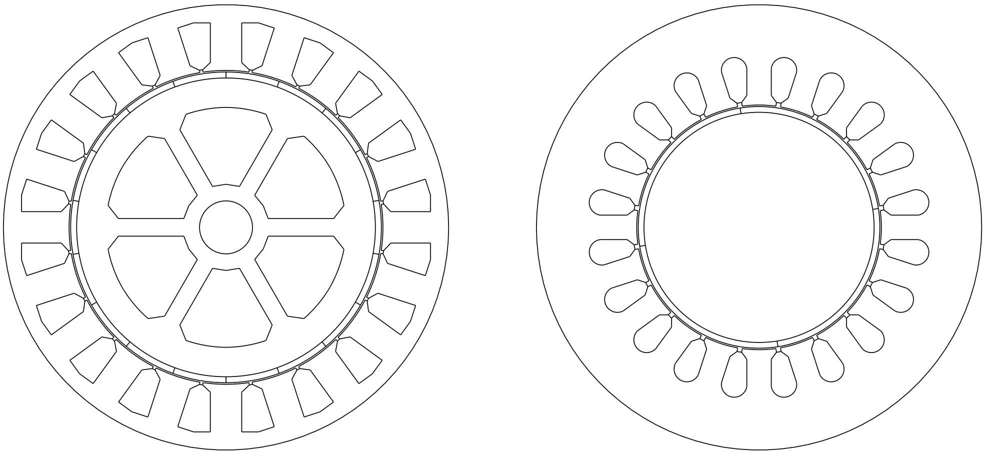

(a) 20-slot 18-pole, five-phase machine **(b)** 20-slot 4-pole, five-phase machine

Figure 6.1 – Motor geometry

Material properties

The allocation of material properties to the various components of the motor, such as magnetic permeability, conductivity, and losses is essential for the simulation. These properties govern the electromagnetic behavior of the materials and are critical for accurate simulation results. Specifically, the following materials have been defined:

- *Air* from FEMM material library;
- *Cu* with electrical resistivity ρ_{Cu} at $T_{\text{work}} = 120\,^{\circ}\text{C}$;
- *N42H* with electrical resistivity ρ_{pm} and coercivity field H_{cB} at $T_{\text{work}} = 120\,^{\circ}\text{C}$;
- *M-19 Steel* Iron from FEMM material library, with electrical resistivity ρ_{Fe} at $T_{\text{work}} = 120\,^{\circ}\text{C}$ and a thickness of 0.36 mm.

Mesh generation

FEMM automatically generates a finite element mesh based on the motor geometry, discretizing the domain into small elements. Since the density and quality of the mesh can significantly impact the accuracy and computational efficiency of the simulation, mesh valued across the analyzed domain have manually selected:

- *Air at air gap*: mesh size of 0.25;
- *Cu in the slot*: mesh size of 3;
- *Permanent magnets*: mesh size of 1;
- *Stator and rotor steel*: mesh size of 2.5.

Since the highest field gradients take place in the air gap, the mesh was predominantly refined in the this region [11].

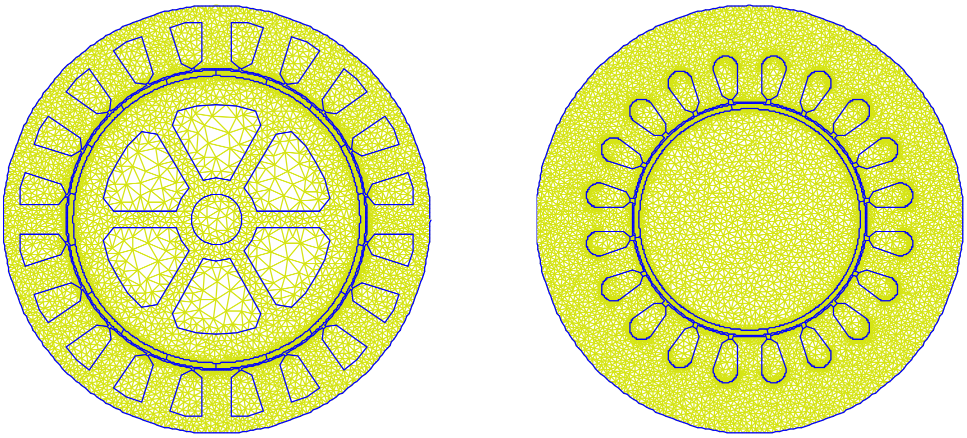

(a) 20-slot 18-pole, five-phase machine **(b)** 20-slot 4-pole, five-phase machine

Figure 6.2 – Mesh density

Boundary conditions

The specification of boundary conditions is crucial to model the external influences on the motor. These boundary conditions play a crucial role in simulating realistic operating conditions. Specifically, in order to achieve tangential induction at the outer edge of the rotor, homogeneous Dirichlet boundary conditions $A_\text{z} = 0$ is imposed along the the external circumference of the motor [11].

Solver configuration

The FEMM solver settings are configured, including convergence criteria, time-stepping parameters and other simulation-specific parameters. During the simulation, the AC Newton solver with solving step of 10^{-8} has been utilized.

Analysis and post-processing

The simulation and analyze of the results utilizes post-processing tools provided by FEMM, including visualization of magnetic flux density distributions, calculation of torque and power output, and evaluation of efficiency and losses.

6.1.1 Computation on the solved structure

Once the field problem is solved, the z-axis component of the magnetic vector potential $A_\text{z}(x, y)$ is known in each point within the domain. Therefore it is possible to evaluate the magnetic flux and the induced EMF. Particular care has to be kept to the coil distribution in the stator slots.

Magnetic flux

The magnetic flux associated with the j-th phase stator winding is given by:

$$\Lambda_{j,\mathrm{s}} = 2pL_{\mathrm{Fe}}\frac{n_{\mathrm{c}}}{n_{\mathrm{pp}}}\sum_{q=1}^{Q} k_{jq}\frac{1}{S_{\mathrm{slot}}}\int\limits_{S_{\mathrm{slot}}} A_{\mathrm{z}}\,\mathrm{d}S \tag{6.1}$$

where $L_{\mathrm{Fe}} = L_{\mathrm{stk}}k_{\mathrm{pack}}$ is the active length of the rotor, n_{c} and n_{pp} are the number of conductors in the slot and the number of parallel path, respectively. The number of slots is Q while the number of poles is $2p$. Finally, k_{jq} is the coefficient that considers whether the conductors in the q-th slot belongs to the j-th phase and their orientation.

The coefficient k_{jq} varies depending on the winding type and on the orientation of the coil. For a single-layer winding k_{jq} is equal to:

- $k_{jq} = 0$: if the coil side in the q-th slot does not belong to the j-th phase;
- $k_{jq} = +1$: if the coil side in the q-th slot belongs to the j-th phase and its orientation is positive with respect to the z-axis direction ($\odot$);
- $k_{jq} = -1$: if the coil side in the q-th slot belongs to the j-th phase and its orientation is negative with respect to the z-axis direction ($\otimes$).

For a double-layer winding k_{jq} is equal to:

- $k_{jq} = 0$: if the coil sides in the q-th slot do not belong to the j-th phase;
- $k_{jq} = +0.5$: if only one coil side in the q-th slot belongs to the j-th phase and its orientation is positive with respect to the z-axis direction;
- $k_{jq} = -0.5$: if only one coil side in the q-th slot belongs to the j-th phase and its orientation is negative with respect to the z-axis direction;
- $k_{jq} = +1$: if both coil sides in the q-th slot belong to the j-th phase and their orientation is positive with respect to the z-axis direction;
- $k_{jq} = -1$: if both coil sides in the q-th slot belong to the j-th phase and their orientation is negative with respect to the z-axis direction.

For a four-layer winding k_{jq} is equal to:

- $k_{jq} = 0$: if the four coil sides in the q-th slot do not belong to the j-th phase;
- $k_{jq} = +0.25$: if only one coil side in the q-th slot belongs to the j-th phase and its orientation is positive with respect to the z-axis direction;
- $k_{jq} = -0.25$: if only one coil side in the q-th slot belongs to the j-th phase and its orientation is negative with respect to the z-axis direction;
- $k_{jq} = +0.5$: if two coil sides in the q-th slot belong to the j-th phase and their orientation is positive with respect to the z-axis direction;
- $k_{jq} = -0.5$: if two coil sides in the q-th slot belong to the j-th phase and their orientation is negative with respect to the z-axis direction;

- $k_{jq} = +0.75$: if three coil sides in the q-th slot belong to the j-th phase and their orientation is positive with respect to the z-axis direction;
- $k_{jq} = -0.75$: if three coil sides in the q-th slot belong to the j-th phase and their orientation is negative with respect to the z-axis direction;
- $k_{jq} = +1$: if all four coil sides in the q-th slot belong to the j-th phase and their orientation is positive with respect to the z-axis direction;
- $k_{jq} = -1$: if all four coil sides in the q-th slot belong to the j-th phase and their orientation is negative with respect to the z-axis direction.

It is advantageous to construct the slot matrix $\mathbf{k}_{\text{slot}}$ in order to depict the winding arrangement and the corresponding values of k_{jq}. This matrix serves as a convenient representation of the winding configuration and facilitates the calculation of magnetic flux linkage during the simulation process.

For instance, the first half of slot matrix $\mathbf{k}_{\text{slot}}$ for a 20-lots and 18-poles five-phase machine having 4-layer winding is:

$$\mathbf{k}_{\text{slot}} = \begin{bmatrix} 0.75 & -0.25 & 0 & 0 & 0 & 0 & 0 & 0 & -0.25 & 0.75 \\ 0 & 0 & 0 & 0 & -0.25 & 0.75 & -0.75 & 0.25 & 0 & 0 \\ -0.25 & 0.75 & -0.75 & 0.25 & 0 & 0 & 0 & 0 & 0 & 0 \\ 0 & 0 & 0 & 0 & 0 & 0 & 0.25 & -0.75 & 0.75 & -0.25 \\ 0 & 0 & 0.25 & -0.75 & 0.75 & -0.25 & 0 & 0 & 0 & 0 \end{bmatrix} \tag{6.2}$$

Induced EMF

For a synchronous machine, the permanent magnet or excited rotor generates an air-gap magnetic flux that links with the stator winding. The movement of the rotor induces an electromotive force (EMF) in the stator windings proportional to the rate of change of the flux linkage. It is possible to define the induce EMF in the stator winding of the generic j-th phase as product between the rotational speed $\omega_{\text{m}}^{\text{e}}$ and the peak magnetic flux Λ_j:

$$E_{j,\text{s}} = \frac{1}{\sqrt{2}} \omega_{\text{m}}^{\text{e}} \Lambda_{j,\text{s}} \tag{6.3}$$

By rotating the rotor of a fixed step and solving the corresponding field equations, the magnetic flux distribution can be precisely determined, enabling the mapping of induced electromotive force [11].

Torque

The torque calculation involves integrating Maxwell's stress tensor along a surface containing the rotor. Due to the two-dimensional nature of the problem, this integration simplifies to integrating the stress tensor along a line, denoted as l_{g}, positioned in the middle of the air-gap.

The obtained result is then multiplied by the active length of the rotor, L_{Fe}. Considering a $2p$ poles machine, the torque is expressed as:

$$T = \frac{D_{\mathrm{s}} - g}{2} \frac{L_{\mathrm{Fe}}}{\mu_0} 2p \int\limits_{l_{\mathrm{g}}} B_{\mathrm{r}} B_{\vartheta} \, \mathrm{d}l \tag{6.4}$$

Here, B_{r} represents the radial component of the flux density (normal to the line l_{g}), B_{ϑ} denotes the azimuthal component of the flux density (tangential to the line l_{g}), D_{s} is the inner stator diameter, g is the air gap length and μ_0 denote the vacuum magnetic permeability. Since the simulation has been carried out on whole motor domain, the number of poles $2p$ is utilized.

Due to numerical considerations inherent in the finite element method, the torque calculation may vary based on the integration line's position and the number of integration points chosen. To enhance accuracy, instead of directly integrating along l_{g}, it's preferable to compute the average torque value over the entire air-gap surface S_{g}. This leads to the torque formula:

$$T = \frac{L_{\mathrm{Fe}}}{\mu_0 g} 2p \int\limits_{l_{\mathrm{g}}} r B_{\mathrm{r}} B_{\vartheta} \, \mathrm{d}l \tag{6.5}$$

where, r represents a dummy radius variable used in the integration process.

Alternative methods for calculating the torque using the finite element method are outlined in [11].

6.1.2 No load simulation

To compute the no-load flux linkage, the permanent magnet is magnetized using the *B-H* curve, therefore H_{cB}, while the stator winding is open-circuited, hence a null conductivity is assumed. Stator and rotor laminations are characterized by the *B-H* curve of the magnetic material used in the simulation, in this case *M-19 Steel.* [11]. In Fig. 6.3 the *B-H* non-linear curve of the *M-19 Steel* is depicted.

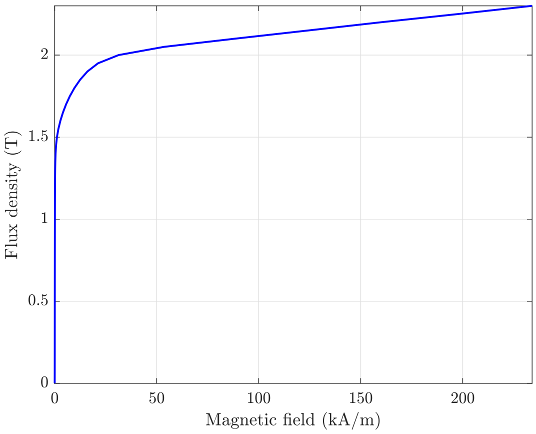

Figure 6.3 – *B-H* curve *M-19 Steel*

Initially, it is necessary to identify the initial position of the d-axis of the synchronous reference system and evaluating the mechanical angle, measured with respect to the positive horizontal semi-axis, at which the flux linked to phase a is maximum. This occurs when the d-axis aligns with the $\alpha = \mathrm{a}$ axis of the stator-fixed reference system.

After the new reference frame d is identified, an open-circuit simulation is carried out by rotating the rotor for an entire pole pitch $\vartheta_\mathrm{m} = 360°/p$. The simulation step in electrical angle is equal to $\vartheta_\mathrm{m}^\mathrm{e} = 1°$, therefore $\vartheta_\mathrm{m} = 1°/p$.

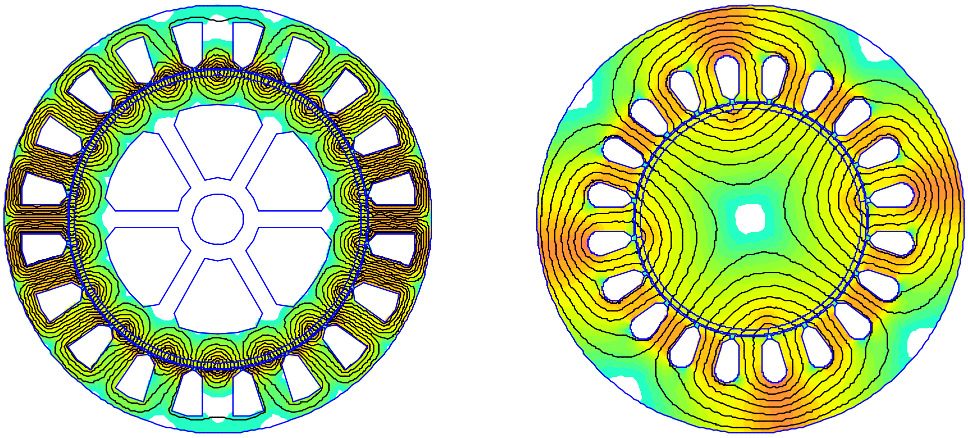

(a) FSCW 20-slot 18-pole **(b)** Concentrated winding 20-slot 4-pole

Figure 6.4 – No load simulation flux lines for different five-phase machines

Using the expressions (6.1) and (6.3) it is possible to map the magnetic flux distribution and the induced EMF, respectively.

It is possible to determine the fluxes linked with the five phases, as depicted in Fig. 6.5a. These fluxes exhibit a sinusoidal shape with a peak value of $\Lambda = 0.469\,\mathrm{Vs}$, in alignment with the analytically estimated fundamental value of $\Lambda_\mathrm{pm} = 0.463\,\mathrm{Vs}$. By applying the abcde/dq transformation, it is possible to derive the fluxes linkage in the synchronous reference frame, Fig. 6.5a. According to the theory, since the analyzed machine is a surface-mounted permanent magnet motor, only the d-axis of the flux is present Λ_d, which coincides with the magnet's flux Λ_pm.

In reality the d-flux and q-flux experience residual oscillation with the dominant harmonic being the 20-th order, as depicted in Fig. 6.5b. For the d-axis, the residual oscillation around the mean value amounts to approximately 0.04%, therefore negligible.

During no-load operation, the only torque contribution originates from cogging torque caused by the interaction between the permanent magnets and the stator teeth, as depicted in Fig. 6.7a. This torque naturally does not contribute to the continuous motion of the machine, given its zero mean value according to simulation results.

Subsequently, the analysis computes the radial force acting on the rotor due to the attraction between the permanent magnets and the ferromagnetic core. Its estimated average value of $F_\mathrm{avg} = 1.003\,\mathrm{Nm}$ is obtained from results.

Finally, the distribution of the air-gap flux density along the entire circumference is evaluated, as depicted in Fig. 6.8a. The air gap flux density is expressed as a function of the mechanical

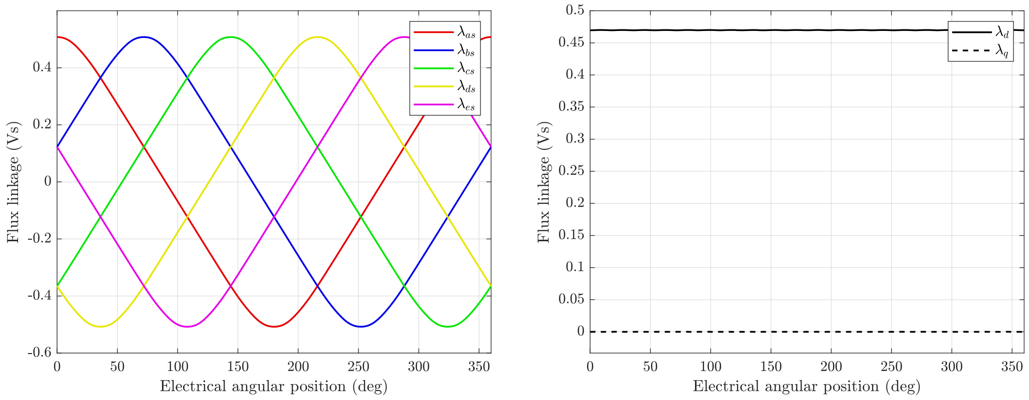

(a) Flux linkage distribution **(b)** Flux linkage in d − q reference frame

Figure 6.5 – No load simulation results

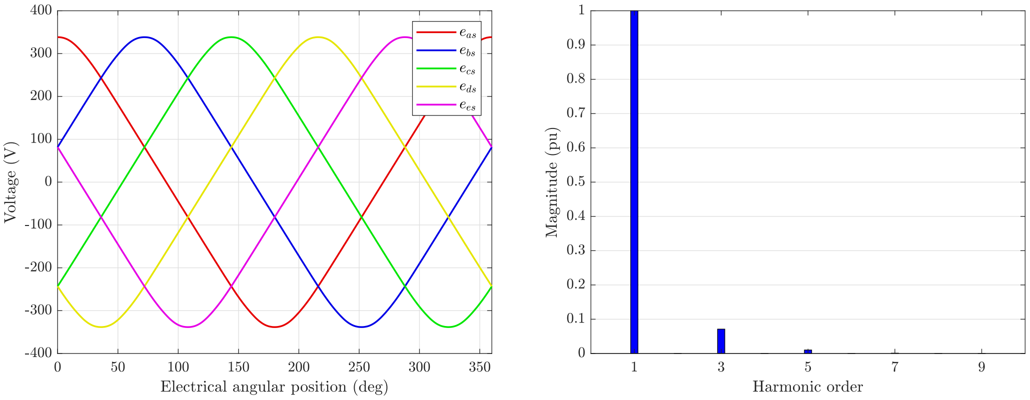

(a) Induced EMF distribution **(b)** Fourier analysis of single phase

Figure 6.6 – No load simulation results

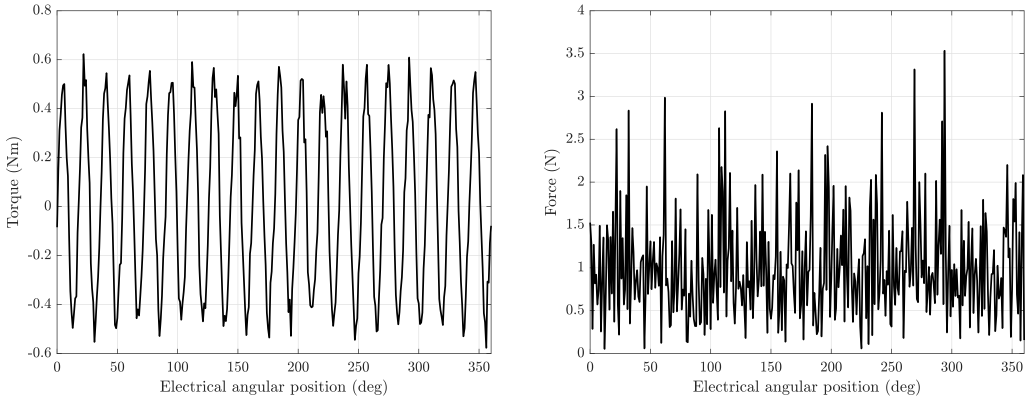

(a) Cogging torque **(b)** Radial force

Figure 6.7 – No load simulation results

angle θ_m measured relative to the positive horizontal semi-axis, and with a configuration having angular position of $\theta_\mathrm{m} = 0°$. The results reveal a slightly distorted square wave, due to the small slot opening w_so of the analyzed FSCW machine [3]. Furthermore, it is noteworthy that only odd prime harmonics of the fundamental wave $\nu = p$ (1,3,5) are present in the harmonic content, fig. 6.8b. This observation aligns with theoretical expectations, given the rectangular shape of the PM's magnetic flux waveform.

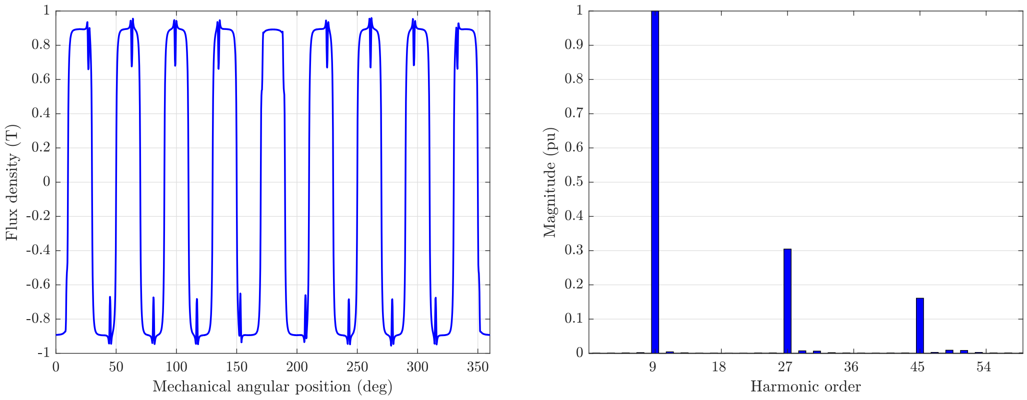

(a) Radial air gap flux density distribution **(b)** Fourier analysis of air gap flux density

Figure 6.8 – No load simulation results

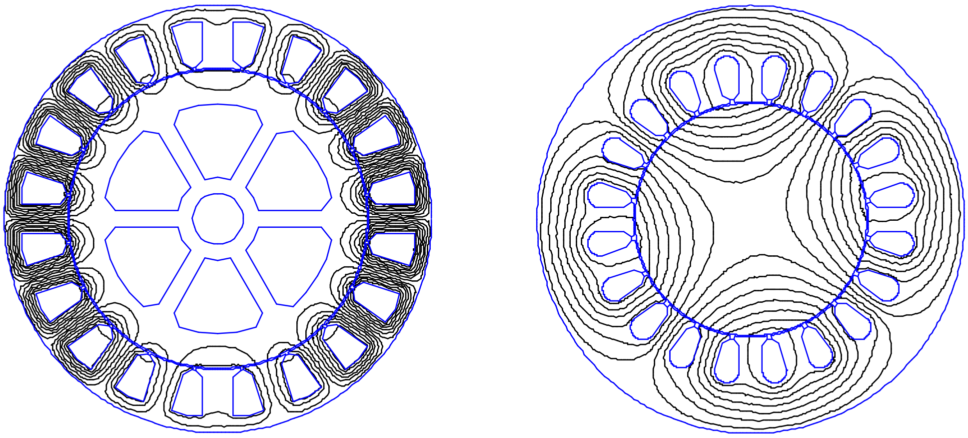

(a) FSCW 20-slot 18-pole **(b)** Concentrated winding 20-slot 4-pole

Figure 6.9 – Stator flux lines for different five-phase machines under 1st harmonic

Upon observation of Fig. 6.10a and 6.10b, it becomes evident that, in the Fractional Slot Concentrated Winding configuration, the flux generated by the 3rd harmonic current produces a 7 pole pair flux, differently from the intended 27 pole pairs. In contrast, this phenomenon is not observed in the concentrated winding machine, where the 3rd harmonic current generates a 2 pole pair flux. Consequently, this different results in superior torque enhancement during Third Harmonic Injection (THI).

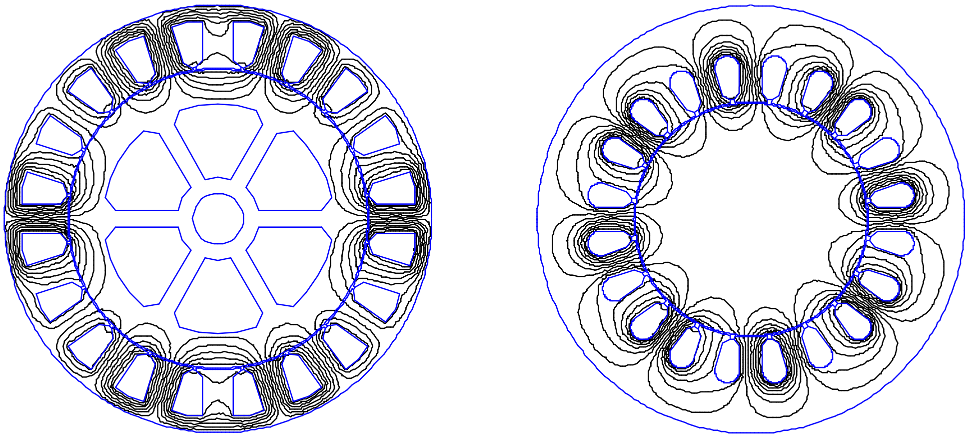

(a) FSCW 20-slot 18-pole **(b)** Concentrated winding 20-slot 4-pole

Figure 6.10 – Stator flux lines for different five-phase machines under 3rd harmonic

6.1.3 Harmonic content in the air gap

To analyze the harmonic content of the air gap flux density produced by the stator windings, and consequently the MMF, a new simulation has been conducted. The procedure follows the same steps outlined in 6.1.1. The test is performed for a single step angle, specifically at $\theta_\mathrm{m} = 0°$, similarly to the air gap flux density distribution test under no load conditions.

The harmonic content analysis is conducted considering different harmonic components in the stator current: specifically, the 1-st harmonic or fundamental, the 3-rd, and the combination of 1-st and 3-rd harmonics.

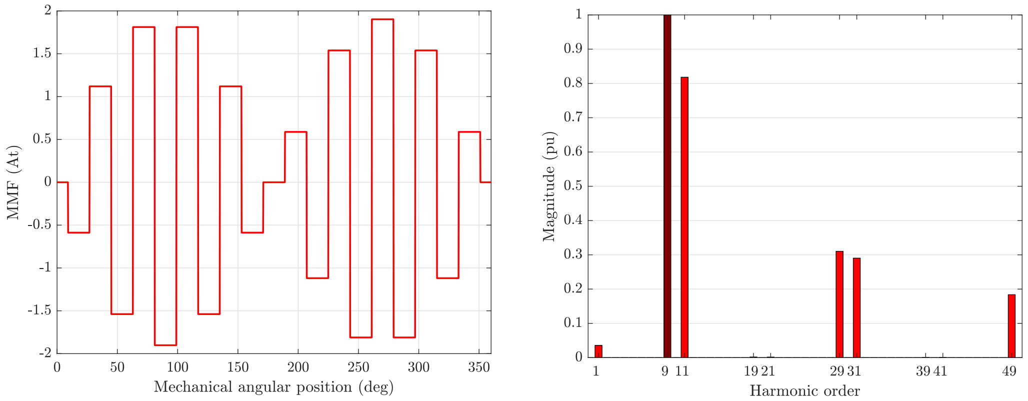

(a) MMF distribution **(b)** Fourier analysis

Figure 6.11 – Harmonic content in the air gap, 1st harmonic current

The obtained results are subsequently compared to theoretical results evaluated in Section 3.1, as depicted in Fig. 6.12 and 6.11. From the results, it is possible to notice a nearly perfect alignment between the theoretical-analytical results and the experimental ones. This observation is crucial as it verifies the reliability of the general matrix-based approach described in Section 3.1.3.

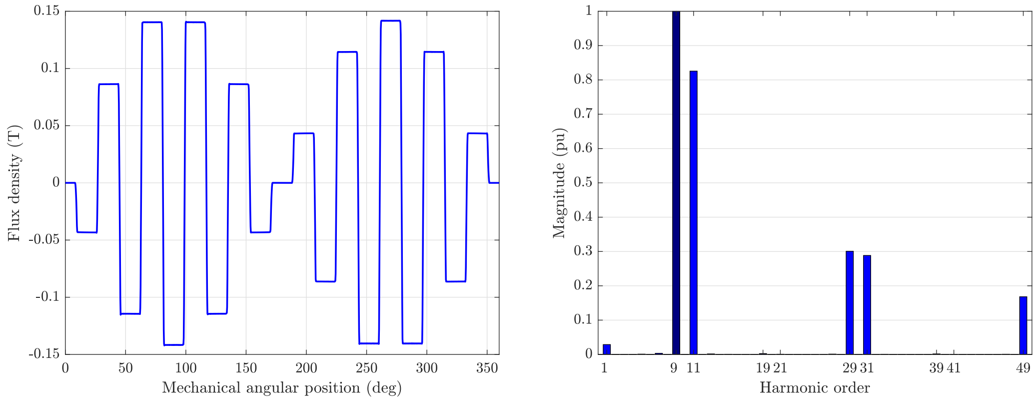

(a) Air gap flux density distribution **(b)** Fourier analysis

Figure 6.12 – No load simulation results, 1st harmonic current

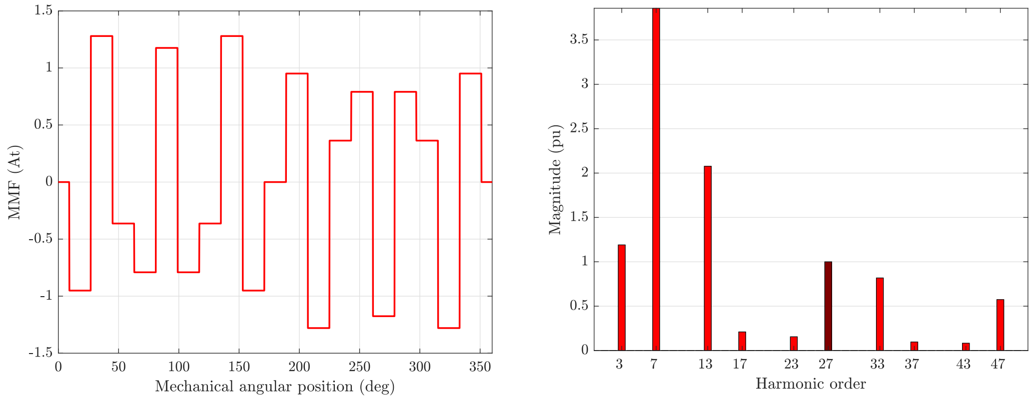

(a) MMF distribution **(b)** Fourier analysis

Figure 6.13 – No load analytical results, 3rd harmonic current

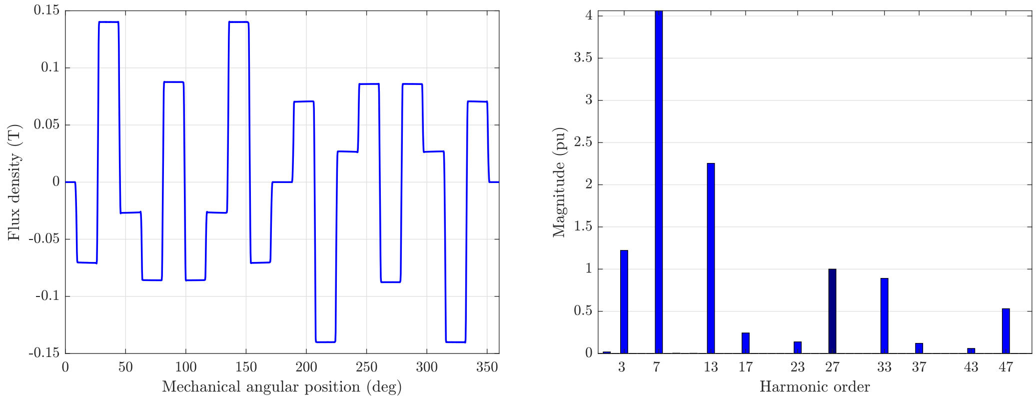

(a) Air gap flux density distribution **(b)** Fourier analysis

Figure 6.14 – No load simulation results, 3rd harmonic current

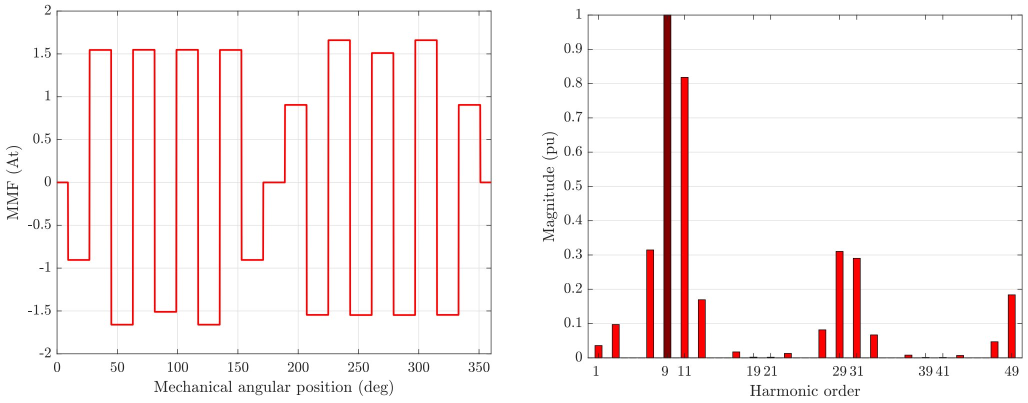

(a) MMF distribution **(b)** Fourier analysis

Figure 6.15 – No load analytical results, 3rd harmonic current

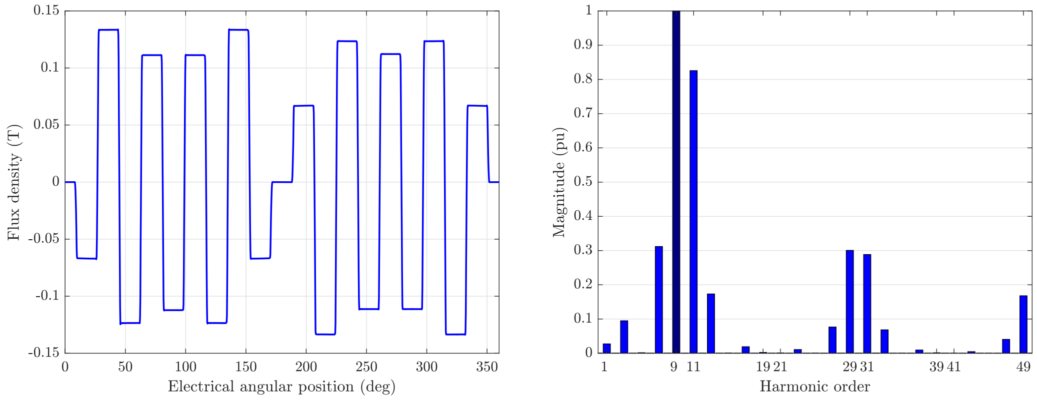

(a) Air gap flux density distribution **(b)** Fourier analysis

Figure 6.16 – No load simulation results, 3rd harmonic current

6.1.4 Mapping

To determine the electrical angle corresponding to maximum torque production, the rotor is rotated by a fixed step for an entire pole pitch (τ_p), while the stator currents remain constant over time. This study enables to evaluated the torque produced by the machine as a function of the rotor position, as showed in Fig. 6.17. It can be observed that the maximum torque occurs when the electrical angle is equal to $\theta_{\mathrm{m}}^{\mathrm{e}} = 90°$. This aligns with theory, as injecting quadrature current i_{q} enables the motor to achieve maximum torque.

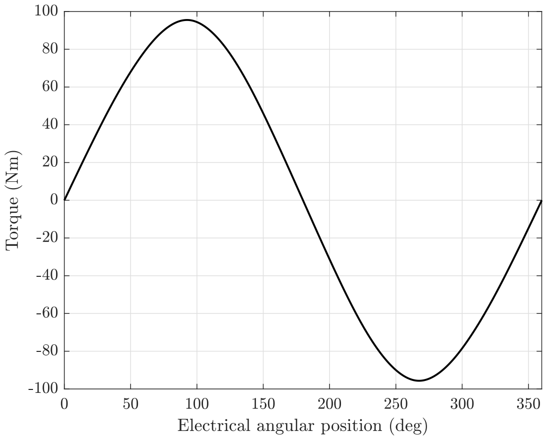

Figure 6.17 – Mapping of the Torque

6.1.5 Results under MTPA

Once the maximum torque is determined, the behavior of the machine under Maximum Torque Per Ampere (MTPA) conditions can be assessed. This study allows for the calculation of the average torque value over one full electrical rotation of the rotor. Additionally, the oscillation of torque, known as torque ripple, can be computed. The average torque under nominal healthy condition is equal to $T_{\text{avg}} = 95.3\,\text{Nm}$, therefore almost identical to the analytical value used in sec. 4.2.3.

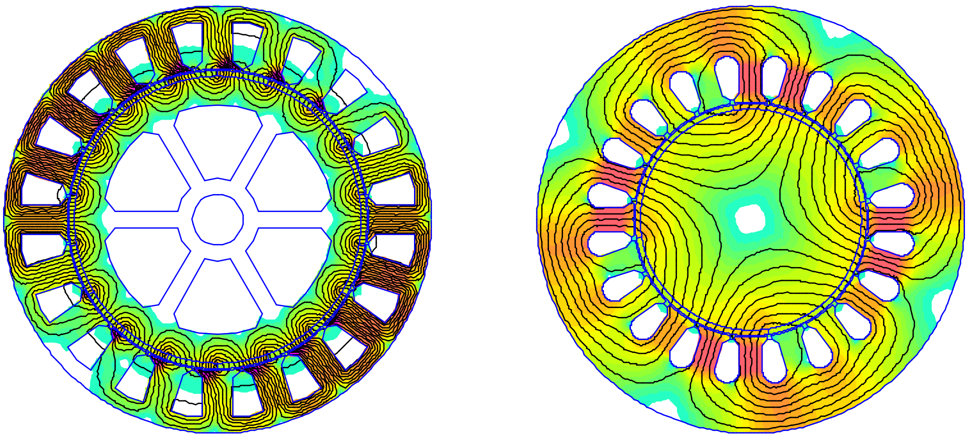

(a) FSCW 20-slot 18-pole **(b)** Concentrated winding 20-slot 4-pole

Figure 6.18 – MTPA simulation flux lines for different five-phase machines

In the case of a non-saturated machine, the torque ripple is directly influenced by the harmonic content of the machine winding. This is because non-main harmonic waves produces by the stator winding interact with the permanent magnet flux at different speeds compared to the fundamental frequency. The torque ripple, displayed in fig. 6.20, has an oscillating behaviour with a dominant harmonic of the 20-th order. The torque ripple is calculated to be $\tau = 1.31\%$ of the average torque T_{avg}. The low torque ripple is attributed to the utilization of the 4-layer winding configuration, which significantly restricts its harmonic content.

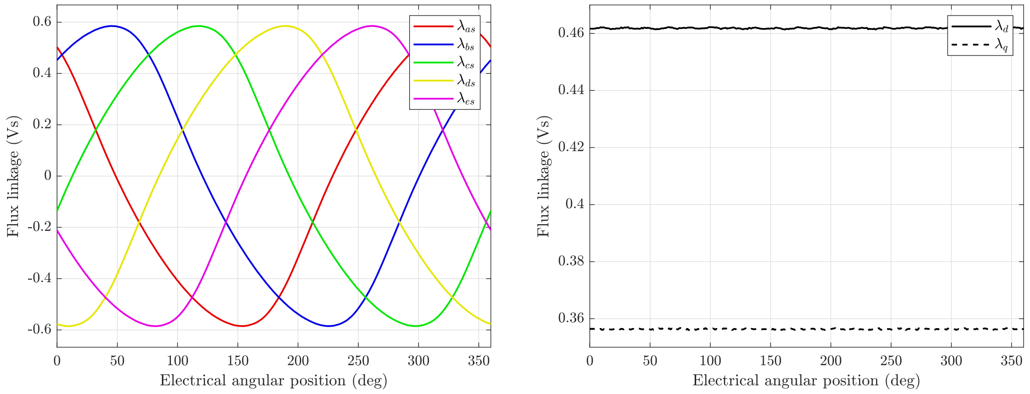

(a) Air gap flux density distribution **(b)** Fourier analysis

Figure 6.19 – MTPA simulation results

In Fig. 6.19a, the flux linkage of the machine is depicted. Unlike the sinusoidal distribution observed during the no-load test, the flux distribution is non-sinusoidal. This occurs due to the interaction between the armature winding and the magnetic field generated by the rotor, resulting in the induction of an electromotive force (EMF) within the armature winding itself. Finally, the fluxes in the $d - q$ reference frame are evaluate via matrix transformation, Fig. 6.19b.

The MTPA test was also conducted for FSCW machines with both 2-layer and 1-layer winding configurations. From Fig. 6.20, it is evident that as the number of layers increases, the torque ripple decreases while the average torque increases. Indeed the torque ripple for FSCW with single-layer and double-layer is $\tau = 2.95\%$ and $\tau = 1.88\%$, respectively. The Table 6.1 is provided for a comprehensive comparison between different winding typologies for the FSCW machine. From the table, it is evident that the torque ripple between the concentrated and FSCW machines exhibits a considerable difference. Specifically, the concentrated winding configuration demonstrates higher torque ripple.

Configuration	**Average torque (Nm)**	**Torque ripple (%)**
4L FSCW	95.28	1.31
2L FSCW	93.67	1.88
1L FSCW	90.05	2.95
Concentrated	91.07	14.67

Table 6.1 – Comparison of torque and torque ripple results with different winding configurations

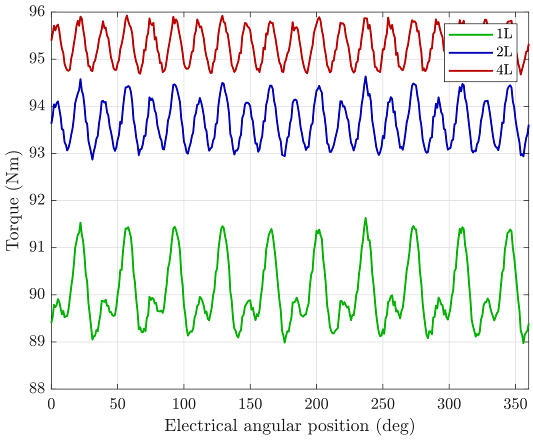

Figure 6.20 – Torque of FSCW machine with different number of layers

6.1.6 Results under THI

As explained in Section 5.4, it is possible to enhance the torque by injecting third harmonic current into the stator windings over time. Two possible modes of THI are available: rms and peak. Therefore, two separate simulations are then carried out to evaluate the increase in the average torque value under MTPA condition. It is observed that the increase due to peak third harmonic injection yields a higher torque value compared to the nominal case and to the rms THI case. This is because the injection of third harmonic allows for an increase in the fundamental current value, upon which the torque depends, although they come at the cost of higher RMS value and therefore higher losses (+15.9% for FSCW motor while +9.2% for concentrated winding motor).

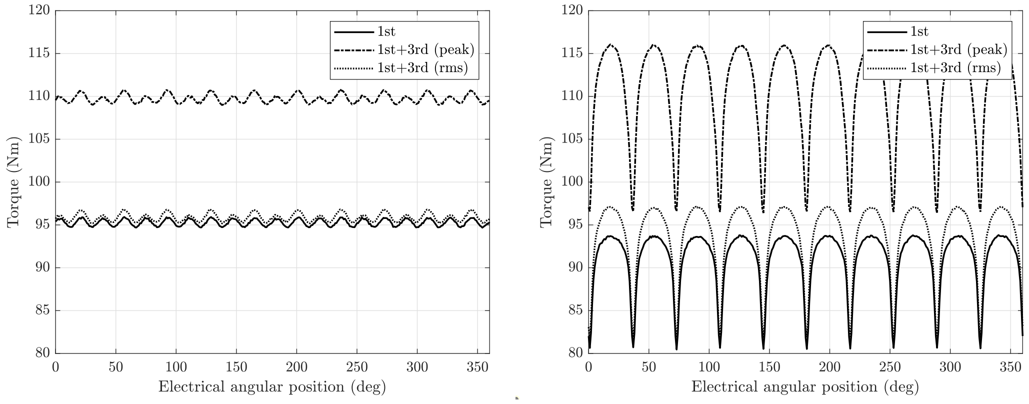

(a) 20-slot 18-pole, FSCW 4-layer winding machine

(b) 20-slot 4-pole, 1-layer concentrated winding machine

Figure 6.21 – Torque under THI

The average torque value under rms mode is $T_{\text{avg,rms}} = 95.88\,\text{Nm}$ (a +0.6% increment), whereas under the peak mode, it is $T_{\text{avg,peak}} = 109.74\,\text{Nm}$ (a +15.2% increment) under peak mode. Consequently, for the purpose of torque enhancement, the peak mode demonstrates significant advantages, as depicted in Fig. 6.21a.

Regarding torque ripple, it is noticeable that it increases in both cases of THI, as there is an increment in the harmonic content of the stator flux. Indeed, in both modes, there is a torque ripple with a dominant harmonic of the 10-th order, while the 20-th order is also present. The torque ripple under rms mode is $\Delta\tau = 1.75\%$, while under peak mode is $\Delta\tau = 1.68\%$. However, despite this increase, the absolute value of the torque ripple remains very low.

Overall, neither the peak nor rms modes are deemed viable solutions for enhancing the torque in FSCW machine. While the rms mode fails to substantially increase the torque, the peak mode, although effective in boosting the torque, results in elevated losses and even higher harmonic content.

A more effective solution would involve solely increasing the fundamental component of the current, although this approach would not be considered torque enhancement per se.

However, the aforementioned observations do not entirely hold true for a machine with a concentrated winding configuration. Indeed, by observing the results in the Fig. 6.21b, a substantial increase in torque can be noticed. The average value of torque under nominal, rms and peak mode are $T_{\text{avg}} = 91.07\,\text{Nm}$, $T_{\text{avg,rms}} = 93.65\,\text{Nm}$ and $T_{\text{avg,peak}} = 110.99\,\text{Nm}$ respectively. Hence there is an increase of +2.83% under rms mode, and +21.87% under peak mode. A more substantial increase in torque is observed, as the third harmonic in the concentrated winding is capable of producing a magnetic field with a dominant harmonic three times the fundamental $\nu = 3p$, unlike in the FSCW, as depicted in Fig. 6.10a and 6.10b.

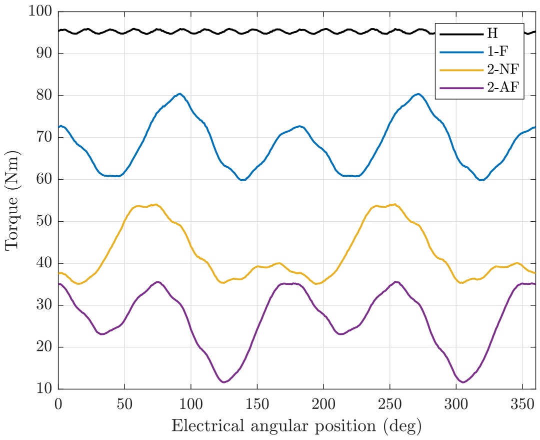

Figure 6.22 – Torque under healthy and faulty cases

It is important to underline that, even in this case, there is an increase in the torque ripple. However, the torque ripple is greater in relative value due to the concentrated winding's higher harmonic content. Moreover, contrarily to the FSCW, the concentrated winding configuration does not have number of poles close to the number of slots. Nevertheless, the concentrated winding machine under THI demonstrates considerable greater performance although, some of the drawbacks associated with THI persist.

Configuration	Average torque (Nm)	Torque ripple %
4L FSCW (peak)	109.74	1.68
Concentrated (peak)	111	17.76
4L FSCW (rms)	95.88	1.75
Concentrated (rms)	93.65	16.48

Table 6.2 – Torque comparison under THI

The reults of the simulation for the MTPA control strategy under THI are summerised in Table 6.2.

6.1.7 Results under faulty conditions

In Section 5.3, a comprehensive model analysis has been carried out for three different faulty conditions: one-phase open-circuit fault, open-circuit fault of two nonadjacent phases, open-circuit of two adjacent phases.

Subsequently, simulations are conducted to analyze the steady-state behavior of the torque for the 4-layer FSCW motor under each of these faulty cases, in order to evaluate the average torque and torque oscillation. Then a comparison with the nominal case has been conducted, as depicted in Fig. 6.22.

From the results depicted in figure 6.22, it can be observed that the developed torque decreases from the nominal value for the different fault scenarios. This is attributed to the control strategy employed, which aims to maintain a peak current equal to the nominal value. It can indeed be demonstrated that when a fault occurs, it is possible to achieve an average torque value equal to the nominal value by increasing the current.

Regarding the torque ripple, it is observed that it increases considerably in the case of a fault, while it worsens drastically when two faults occur. This is due to the fact that the motor is controlled to create an optimized flux shape with the remaining healthy phases, without however being able to produce a flux waveform equal to that of the nominal case without faults. The torque ripple is therefore attributed to the introduction of harmonics by the remaining healthy phases, caused by a shifting in the spatial arrangement of the phases themselves.

In conclusion, it can be stated that the motor control under faulty conditions has good performance, however, its operation may be considered acceptable only for short periods of time. This is due to the persistent presence of torque ripple, which remains constant or may worsen with an increase in current, aiming to reach the nominal torque value.

The simulation results are summarized in the Table 6.3.

Configuration	**Average torque (Nm)**	**Torque ripple %**
4L FSCW (1F)	68.43	30.16
4L FSCW (2NAF)	42.34	44.98
4L FSCW (2AF)	26.48	90.63

Table 6.3 – Torque comparison under faulty conditions

6.2 Losses

Various types of losses contribute to the dissipation of energy during the operation of electric motors, thereby decreasing motor efficiency. This section focuses on the evaluation of copper losses and core losses, excluding mechanical losses attributed to ventilation or friction from the analysis.

6.2.1 Copper losses

Copper losses in electric motors refer to the dissipation of energy in the form of heat due to the inherently presence of electrical resistance in the motor conductor windings. Indeed, when an electric current flows through a conductor, it interacts with the lattice structure of the material, resulting in collisions between electrons and lattice atoms. These collisions hinder the flow of electrons, therefore creating an electrical resistance. According to Ohm's law, the resistance R causes a dissipation of electrical energy proportional to the square of the current I^2 flowing through the conductor, as described by the following formula:

$$P = RI^2 \tag{6.6}$$

The dissipated energy is primarily manifested as thermal energy due to the increased kinetic energy of the lattice atoms and charge carriers. This phenomenon, known as Joule heating, leads to a rise in temperature within the conductor, contributing to the conversion of electrical energy into thermal energy.

Minimizing copper losses is therefore essential for improving the efficiency of electrical machines, as less power is wasted as heat and more power is converted into useful mechanical power.

The Joule power losses of the coils and their corresponding resistances are determined using classical analytical relationships, since the coils are modeled as equivalent conducting bars and the simulations are carried out with stationary current (steady-state simulation) [11]. The non-uniform current distribution in the winding due to the source frequency is evaluated with the rotating losses, although it is almost negligible due to the small conductor diameter d_c employed in the machine winding.

In order to evaluate analytically the copper losses, it is crucial to calculate the length of the end winding l_ew. In this work half turn of the end-winding is modelled using a rectangular shape featuring curved edges, therefore the following geometrical equation is used for the evaluation of the end winding length [52]:

$$l_\mathrm{ew} = 2\tau_c - 4r_\mathrm{end} + 2\pi r_\mathrm{end} + 4l_\mathrm{ex} \tag{6.7}$$

where τ_c represents the average coil pitch, r_end the radius of the rounded corners and l_ex the distance from the end section of the motor to the rounded corners.

In the case of a four-layer FSCW, the calculation of τ_c utilizes the same expression as that for the two-layer FSCW [52]. This is because the average coil length of the first and second layers in the four-layer FSCW is equivalent to the coil length of the two-layer winding. The equation is as follows:

$$\tau_\mathrm{c} = \frac{2\pi r_\mathrm{coil}}{Q} - \frac{w_\mathrm{s}}{2} = 22.5\,\mathrm{mm} \tag{6.8}$$

where w_s represents the distance between two teeth at the midpoint of the tooth height, and it is equal to:

$$w_\mathrm{s} = \frac{\pi(D_\mathrm{s} + h_\mathrm{s})}{20} - w_\mathrm{t} = 12.9\,\mathrm{mm} \tag{6.9}$$

and the radius of the center of the coils r_coil is calculated as:

$$r_\mathrm{coil} = \frac{D_\mathrm{s}}{2} + \frac{h_\mathrm{s}}{2} = 92.125\,\mathrm{mm} \tag{6.10}$$

Given the absence of specific parameters, it is presumed that $l_\mathrm{ex} = w_\mathrm{s}/2 = 6.45\,\mathrm{mm}$ and $r_\mathrm{end} = w_\mathrm{s}/2 = 6.45\,\mathrm{mm}$. Therefore the equation (6.7) becomes:

$$l_\mathrm{ew} = 2\tau_c + 2\pi r_\mathrm{end} = 85.5\,\mathrm{mm} \tag{6.11}$$

Therefore, for the FSCW the the total length of the windings l_c is given:

$$l_\mathrm{c} = l_\mathrm{stk} + l_\mathrm{ew} = 150\,\mathrm{mm} \tag{6.12}$$

The stator winding material chosen is copper (Cu), with a corresponding resistivity at the operating temperature $T_{\mathrm{work}} = 120\,^{\circ}\mathrm{C}$ equal to:

$$\rho_{\mathrm{Cu}} = \rho^{*}_{\mathrm{Cu}}(1 + \alpha \Delta T) = 0.0252\,\frac{\Omega\,\mathrm{mm}^2}{\mathrm{m}} \tag{6.13}$$

where $\rho^{*}_{\mathrm{Cu}} = 0.018$ is the copper resistivity at the reference temperature of $T^{*} = 20\,^{\circ}\mathrm{C}$ and $\alpha = 0.004\,\mathrm{K}^{-1}$ is the temperature coefficient of the material

The stator winding resistance is:

$$R_{\mathrm{s}} = \rho_{\mathrm{Cu}} \frac{l_{\mathrm{c}} N_{\mathrm{s}}}{S_{\mathrm{c_{eq}}}} = 2.46\,\Omega \tag{6.14}$$

with $S_{\mathrm{c_{eq}}} = S_{\mathrm{c}} n_{\mathrm{pp}}$. The copper loss are equal to:

$$P_{\mathrm{Joule}} = 5 R_{\mathrm{s}} I_{\mathrm{n}}^2 = 517.4\,\mathrm{W} \tag{6.15}$$

Regarding the 20-slot 4-pole concentrated winding machine, the following expression is used for evaluating the end-winding length [9]:

$$l_{\mathrm{ew}} = 1.6\tau_{\mathrm{p}} = 2.5\frac{D_{\mathrm{s}}}{p} = 162.5\,\mathrm{mm} \tag{6.16}$$

The total length of the windings l_{c} is equal to:

$$l_{\mathrm{c}} = l_{\mathrm{stk}} + l_{\mathrm{ew}} = 422.5\,\mathrm{mm} \tag{6.17}$$

The corresponding stator winding resistance is:

$$R_{\mathrm{s}} = \rho_{\mathrm{Cu}} \frac{l_{\mathrm{c}} N_{\mathrm{s}}}{S_{\mathrm{c_{eq}}}} = 1.88\,\Omega \tag{6.18}$$

with $N_{\mathrm{s}} = 304$ and $S_{\mathrm{c_{eq}}} = 1.723\,\mathrm{mm}^2$ The copper loss are equal to:

$$P_{\mathrm{Joule}} = 5 R_{\mathrm{s}} I_{\mathrm{n}}^2 = 574.3\,\mathrm{W} \tag{6.19}$$

6.2.2 Core losses

Traditionally, core losses in electrical machines are determined by post-processing the magnetic field solution, employing either empirical equations or statistical laws. Notably, various methods are utilized for predicting these losses, with the famous Steinmetz formula from the early twentieth century standing out as a prominent example [45]. The Steinmetz equation provides a simplified but reasonably accurate empirical equation for estimating core losses in electrical machines, especially in situations where detailed magnetic field analysis is impractical or computationally expensive. Although the Steinmetz equation is extensively utilized, it may not comprehensively account for all complexities of core loss behavior in every instance. Therefore, a more accurate empirical method is employed to evaluate machine losses, the so called "Traditional Technique" [19]. In essence, it’s a more precise version of the Steinmetz method.

The total power loss, P_{Fe}, per unit volume dissipated in a ferromagnetic strip lamination, with thickness t, conductivity σ, and periodically magnetized with fundamental frequency f, can then be expressed as the sum of hysteresis loss P_{h}, classical eddy-current loss P_{e}, and excess loss P_{ex}.

$$P_{\mathrm{Fe}} = P_{\mathrm{h}} + P_{\mathrm{cl}} + P_{\mathrm{ex}} = \sum_{\nu=1}^{\nu_{\max}} \left(c_{\mathrm{h}} \nu f_{\mathrm{s}} B_{\mathrm{m}}^2 + c_{\mathrm{cl}} (\nu f_s B_{\mathrm{m}})^2 + c_{\mathrm{ex}} (\nu f_s B_{\mathrm{m}})^{1.5} \right) \tag{6.20}$$

Where B_{m} denotes the amplitude of the ν-th harmonic of the flux density waveform obtained through the time-stepping Finite Element Method (FEM) solution, and $\nu_{\max}$ represents the total number of harmonics considered. Given that the simulation is conducted as a 2D magneto static problem, the field is assumed to be two-dimensional, therefore independent of the coordinate parallel to the machine's shaft (z-direction). Consequently, B_{m} represents the magnitude of the flux density, defined as $B_{\mathrm{m}} = \sqrt{B_{\mathrm{x}}^2 + B_{\mathrm{y}}^2}$.

The classical eddy-current term P_{cl} is derived from Maxwell's equations under the assumption of a uniform flux distribution in the z-direction, hence:

$$c_{\mathrm{cl}} = \sigma \pi^2 d_{\mathrm{c}}^2 / 6 \tag{6.21}$$

where d_{c} and σ are, respectively, the diameter and electrical conductivity of the conductor. Through measurements conducted with Epstein frames, core rings, or single-sheet tester setups, it is possible to determined experimentally the coefficients c_{h} and c_{ex}.

From equation (6.20), it can be observed that the total losses exhibit a dependence approximately proportional to the square of the magnetic flux density B^2. Since the flux concentration is inversely proportional to the stacking factor k_{pack}, it is expected that the flux concentration would result in an increase in losses within the lamination by a factor of $1/(k_{\mathrm{pack}})^2$. However, the decrease in iron per unit volume is directly proportional to the stacking factor k_{pack}, since there's less iron available to generate losses. This effect introduces a compensating factor of k_{pack}. Thus, to incorporate the stacking factor into the loss calculation, the loss formula is simply divided by the stacking factor. During the simulation a stacking factor $k_{\mathrm{pack}} = 0.98$ is assumed.

As the rotor moves past the stator, the time depended flux predicted by the finite element model exhibit a non-sinusoidal behavior due to the inclusion of all effects of the motor's geometry. If the stator steel is characterized only by linear material properties, the losses can be systematically decomposed into elements occurring at different frequencies, which are then combined together to derive the total loss. Despite the non-linearity of the material properties, a commonly employed approximation technique for estimating core losses involves decomposing these losses into multiple components occurring at various time harmonics, as expressed in the equation (6.20).

In addition to core losses, a magnet loss model is introduced to evaluate the iron losses related to the permanent magnets. Magnet loss computation follows the methodology described in [31]. This approach involves neglecting the reaction field of the eddy currents. The current density J_{pm} within the magnet's cross-section is expressed as:

$$J_{\mathrm{pm}} = -\sigma_{\mathrm{pm}} \frac{\mathrm{d}A}{\mathrm{d}t} + J_{\mathrm{c}} \tag{6.22}$$

Here, J_c represents a constraint current density chosen to ensure the total current within the cross-section of each magnet equals zero, and σ_{pm} denotes the electrical conductivity of the permanent magnet material. The loss is subsequently obtained by integrating J_c^2/σ_{pm} over the volume of each magnet.

Following a similar approach to core losses, it proves advantageous within the computational script to decompose the magnetic vector potential A into a series of harmonics. The losses are computed for each harmonic individually and then summed to determine the total loss. At each harmonic, the current density J_{pm} can be represented as:

$$J_{pm} = -\sigma_{pm} j\omega A + J_c \tag{6.23}$$

In order to perform the computation of the total losses, the centroid location and size of each element within a laminated region are recorded. As the rotor's position changes, the finite element mesh is altered. However, the element centroids from the original mesh remain fixed points in the lamination geometry, where the field is assessed in each incremental analysis, regardless of remeshing. Subsequently, the flux density is evaluated at every stored element centroid for each rotor position, effectively establishing a history of flux density versus time for every element within the laminated regions. Special attention is required for points situated within the rotor. The initial centroid positions need to be rotated by the same angle as the rotor to ensure that the rotor field is consistently evaluated at the same points in successive runs. Additionally, the resulting field evaluations must be rotated to ensure that the field at rotor points is consistently represented within the same rotor-fixed reference frame.

Moreover, careful consideration is given to evaluating performance across a sufficiently broad range of angles. Notably, fractional slot concentrated windings, such as the one examined in this work, exhibit sub-harmonics with significant magnitude. Consequently, a wide angle range must be considered to capture the effects of winding sub-harmonics on rotor losses. Specifically, for the 20-slot 18-pole FSCW machine, the losses must be assessed over a 360° rotor motion. This ensures that the rotor magnets are fully exposed to the complete stator winding waveform, encompassing even the lowest sub-harmonic of 1-st order.

Once finite element runs have been executed over a suitably large arc, MATLAB's built-in Fast Fourier Transform (FFT) function is employed to convert the essentially time series of flux densities at each element centroid into amplitudes of various harmonics of flux density. The contributions from all harmonics for all elements are then summed to obtain the total core and proximity effect losses [37].

6.2.3 Core loss data

In the model it has been used the steel $M-19$ with a layer thickness of $t = 0.36\,\text{mm}$, therefore having a gauge equals to 29 ($0.014''$). From [37], it is possible to extract an approximation fit of the data for 29-gauge $M-19$ from 50Hz to 600 Hz. Therefore the coefficients c_h and c_{ex} for the formula (6.20) are equal to:

$$c_h = 143\,\frac{\text{W}}{\text{m}^3\,\text{T}^2\,\text{Hz}} \tag{6.24}$$

$$c_{\mathrm{ex}} = 0.53\,\frac{\mathrm{W}}{\mathrm{m^3\,T^2\,Hz^2}} \tag{6.25}$$

It is assumed that the magnet's orientation direction is axially, therefore it is possible to evaluate the resistivity of the magnet ρ_{pm} at the working temperature T_{work} with the following second-order polynomial fitting curve [44]:

$$\rho_{\mathrm{pm}} = c \cdot (T(^\circ\mathrm{C}))^2 + b \cdot (T(^\circ\mathrm{C})) + a = 1.653\,\frac{\Omega\,\mathrm{mm^2}}{\mathrm{m}} \tag{6.26}$$

For the NdFeB magnet used in the simulation, a concentration of Dysprosium less than 4% is assumed. Therefore the coefficient values of the polynomial fitting curve are: $a = 1.520$, $b = 1.765 \cdot 10^{-3}$, $c = -5.468 \cdot 10^{-3}$.

Given that core and magnet losses are dependent on the machine velocity, they have been evaluated for various speeds, ranging from $n_{\mathrm{min}} = 100\,\mathrm{rpm}$ to the maximum achievable speed n_{max}, as depicted in Fig. 6.23a and in fig. 6.23b.

Flux weakening operation

Flux weakening, also known as field weakening, is a technique employed in the control of electric motors, particularly in variable speed applications. The objective of flux weakening is to extend the speed range of the motor beyond its base speed n_{b} by reducing the magnetic flux in the motor's magnetic circuit, therefore along the d-axis.

The maximum mechanical speed during flux weakening operation is:

$$\omega_{\mathrm{max}} = \frac{V_{\mathrm{N}}}{(\Lambda_{\mathrm{pm}} - L_{\mathrm{d}} I_{\mathrm{n}})\,p} \tag{6.27}$$

To calculate the direct-axis inductance L_{d} and quadrature-axis inductance L_{q} inductances of the machine, the magnets are deactivated and replaced with air. The analyse is performed considering only the direct component of the current i_{d}. Given the surface permanent magnet nature of the machine, the rotor exhibits isotropy, thus resulting in L_{d} and L_{q} being equal.

The direct-axis inductance is calculated using the method of linked fluxes, despite the existence of several other calculation methods [11].

$$L'_{\mathrm{d}} = \frac{\Lambda_{\mathrm{d}}}{I_{\mathrm{d}}} = 45.25\,\mathrm{mH} \tag{6.28}$$

It is also possible to evaluate the leakage inductance relative to the end winding is calculated as [9]:

$$L_{\sigma_{\mathrm{ew}}} = \mu_0 l_{\mathrm{ew}} n_{\mathrm{cs}}^2 q^2 2p\lambda_{\mathrm{ew}} = 0.016\,\mathrm{mH} \tag{6.29}$$

with $\lambda_{\mathrm{ew}} = 0.35$. It is possible to observe the the leakage inductance relative to the end winding is almost negligible.

The total inductance on d-axis is therefore equal to:

$$L_{\mathrm{d}} = L'_{\mathrm{d}} + L_{\sigma_{\mathrm{ew}}} = 45.25\,\mathrm{mH} \tag{6.30}$$

The maximum speed is:

$$\omega_{\mathrm{max}} = \frac{V_{\mathrm{N}}}{(\Lambda_{\mathrm{pm}} - L_{\mathrm{d}} I_{\mathrm{n}})\, p} = 664.73\,\mathrm{rad/s} \tag{6.31}$$

$$n_{\mathrm{max}} \approx 6300\,\mathrm{rpm} \tag{6.32}$$

Regarding the concentrated winding machine, the end winding leakage inductance is equal to:

$$L_{\sigma_{\mathrm{ew}}} = \mu_0 l_{\mathrm{ew}} n_{\mathrm{cs}}^2 q^2 2p \lambda_{\mathrm{ew}} = 1.65\,\mathrm{mH} \tag{6.33}$$

With $n_{\mathrm{cs}} = 76$. The inductance on d-axis is equal to:

$$L'_{\mathrm{d}} = \frac{\Lambda_{\mathrm{d}}}{I_{\mathrm{d}}} = 88.12\,\mathrm{mH} \tag{6.34}$$

Therefore the total inductance on d-axis is:

$$L_{\mathrm{d}} = L'_{\mathrm{d}} + L_{\sigma_{\mathrm{ew}}} = 89.77\,\mathrm{mH} \tag{6.35}$$

The maximum mechanical speed during flux weakening operation is:

$$\omega_{\mathrm{max}} = \frac{1}{p} \frac{V_{\mathrm{N}}}{\Lambda_{\mathrm{pm}} - L_{\mathrm{d}} I_{\mathrm{n}}} = 135.2\,\mathrm{rad/s} \tag{6.36}$$

with $\Lambda_{\mathrm{pm}} = 2.02\,\mathrm{Vs}$ the permanent magnet flux. The maximum speed in rpm is:

$$n_{\mathrm{max}} \approx 1300\,\mathrm{rpm} \tag{6.37}$$

From the values of the maximum speed, it is possible to observe that the FSCW machine has better flux weakening properties [7].

6.2.4 Total losses and performances

Once the core losses for different speed values are evaluated and the joule losses are also known, the efficiency of the two simulated and compared machines, namely the FSCW 20-slot 18-pole, five-phase machine and the concentrated winding 20-slot 4-pole, five-phase machine, can be assessed.

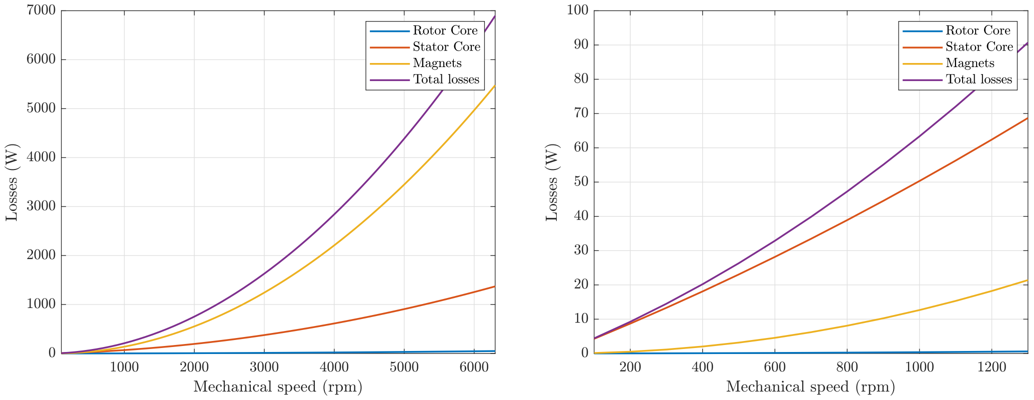

(a) FSCW 20-slot 18-pole **(b)** Concentrated winding 20-slot 4-pole

Figure 6.23 – Rotating losses as a function of the mechanical speed

In Figure 6.24, the core and joule losses for the nominal speed $n = 1000\,\text{rpm}$ are depicted. Although the joule losses are slightly lower in the FSCW machine, the presence of high rotor losses is more than three times higher than that in the concentrated machine. Overall, therefore, the FSCW machine is slightly less efficient than its concentrated counterpart (92.7% vs. 93.6%). The lower joule losses of the FSCW machine are attributed to the reduced end-windings, although the advantages in this regard seem almost negligible.

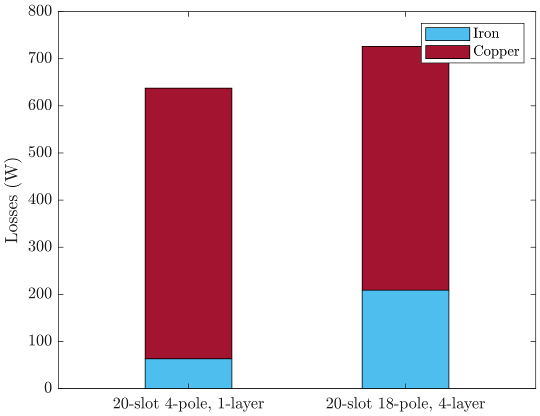

Figure 6.24 – Total losses comparison

It is important to note that in the evaluation of efficiency, mechanical losses have been neglected, as no straightforward method exists to evaluate these losses.

Additionally, it is possible to graphically visualize the core losses across the machine domain for the two motors, as depicted in Fig. 6.25a and Fig. 6.25b. As expected, according to [37], the permanent magnets exhibit the highest loss density. This is attributed to the high resistivity of permanent magnets, particularly at the operating temperature of $T_{\mathrm{work}} = 120\,^{\circ}\mathrm{C}$.

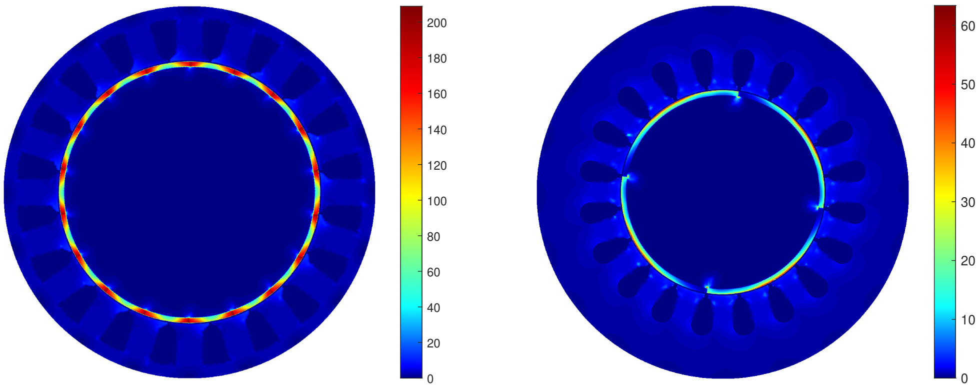

(a) FSCW 20-slot 18-pole **(b)** Concentrated winding 20-slot 4-pole

Figure 6.25 – Rotating losses as a function of the mechanical speed

7 Conclusion

A comprehensive experimental and theoretical analysis was conducted, focusing primarily on Fractional Slot Concentrated Winding (FSCW) machines as a solution for fault-tolerant applications. Various winding typologies, including single, double, and 4-layer windings, were studied extensively. It was observed that the 4-layer winding, when applicable, yielded superior performance compared to the other two configurations, primarily due to lower MMF harmonic content. This translated into higher average torque and lower torque ripple, consistent with theoretical expectations and simulation results.

Furthermore, the FSCW machine was compared with a distributed winding machine to assess its overall performance, including under Third Harmonic Injection (THI). The results validated the theoretical studies, demonstrating that THI can indeed improve torque performance. However, it was observed that while the distributed winding machine exhibited increased performance under THI compared to FSCW, the overall effectiveness of the THI strategy was questioned. This is because although THI led to a slight increase in torque, it also resulted in higher MMF harmonic content, leading to significant worsening of torque ripple.

The primary objective of the thesis was to design a motor suitable for a fault-tolerant test bench. To achieve this goal, an experimental analysis was conducted, focusing on three different open-phase fault scenarios: one-phase open-circuit fault, open-circuit fault of two nonadjacent phases, and open-circuit fault of two adjacent phases.

During the fault analysis, the current limit was set to the pre-fault value to enable a fair comparison, as it ensured that the joule losses remained constant. The results revealed a deterioration in motor performance as the severity of the faults increased, particularly evident in the significantly higher torque ripple observed due to the absence of one or more phases. Despite these challenges, the motors demonstrated resilience to faults, albeit with reduced performance levels compared to normal operating conditions.

Lastly, it is noteworthy to highlight that the concentrated winding machine exhibited slightly higher efficiency than its FSCW counterpart, especially during THI operation. This can be attributed to the concentrated winding machine having lower iron losses, attributed to its better MMF harmonic content and the absence of sub-harmonics. However, when comparing the machines, it becomes apparent that the power density of the FSCW is significantly higher, approximately 4.4 times greater. This substantial advantage of the FSCW underscores its viability not only for fault-tolerant applications but also for scenarios where high power density is crucial, such as in applications where the volume of the machine is a limiting factor.

Furthermore, with the adoption of the 4-layer winding configuration, the FSCW demonstrated higher average torque and lower torque ripple, further emphasizing its superior performance in various operating conditions.

7.1 Possible further development

Further development opportunities for the FSCW include exploring the adoption of a V-shaped Interior Permanent Magnet (IPM) or a hybrid reluctance rotor configuration. This advancement has the potential to yield higher performance levels, including increased power rating, enhanced torque output due to saliency effects, and improved overall efficiency. Additionally, such rotor configurations could mitigate eddy current losses in the permanent magnets and reduce iron losses under open-circuit fault conditions. Moreover, a reduction in the air gap could be achieved, contributing to improved motor performance [17, 22].

Since it has been demonstrated that increasing the number of layers from 4 to 6 yields almost negligible benefits [35], attention can be redirected towards other areas for development. One such area involves the implementation of specialized winding arrangements aimed at further reducing harmonic content, thereby promoting smoother operation and minimizing torque ripple. A notable example is the special three-layer winding, studied in [18]. Additionally, configurations involving an increased number of slots, such as the dual winding approach [2], or variations in the number of turns per slot [46], present promising avenues for further research and development. These approaches hold potential for significantly reducing harmonic content and improving the overall performance of electric machines, particularly in terms of torque quality and efficiency.

Another potential improvement involves implementing multiphase motors with a higher number of phases. By increasing the number of phases beyond three, it becomes possible to utilize higher-order harmonic currents for torque enhancement. This approach can lead to lower torque ripple and reduced joule losses, resulting in better power distribution across the machine [34].

Finally, an extensive study could be conducted on fault-tolerant applications, as the current analysis in this work has focused solely on open-circuit faults. Therefore, there is potential for further research into machine modeling and control strategies for short-circuit faults as well. This comprehensive investigation could provide valuable insights into enhancing the robustness and reliability of multiphase during different types of faults [13, 16].

Regarding concentrated winding configurations, it is also possible to increase the number of phases and utilize distributed winding arrangements instead. This approach ensures better MMF harmonic content, as distributed winding allows for the reduction of non-main harmonic waves.

8 Acknowledgements

Five and a half years ago, I embarked on a journey filled with experiences, both in terms of knowledge and personal growth. This journey has been nothing short of remarkable, not solely for the knowledge gained or the milestones that I have might achieved, but for the extraordinary people I've had the privilege to meet, interact with, and share experiences alongside.

During this journey, I have always been supported and helped by my family, who enabled me to fully dedicate myself to my studies while providing unwavering support. Therefore, I would like to express my gratitude to my father, Giovanni, for imparting numerous life lessons and always being there to answer my questions and satisfy my curiosity. Additionally, I want to thank my sister, Maria Elena, for sharing with me a beautiful childhood filled with fantastic memories, for helping me through difficult times along my journey, and for her contagious laugh, always present during the meals. However, I want to give special thanks to my mother, Fiorina, who from the moment I was born, believed in me and my abilities against all odds and adversities. Throughout these twenty-four years, she has been my rock and my source of inspiration. Her unwavering support and boundless love have been the guiding force behind my achievements.

I would like to thank Pietro, Daniele, Leonardo, Edoardo, Francesco, Jacopo, Niccolò, Matteo, and Simone for their spontaneity, for welcoming me into their family like a brother, and for the evenings spent together playing, drinking, and having fun. Thanks to them, I have experienced beautiful and unforgettable moments. In addition, I would like to thank the friends from the extended group, who brought vitality to the original group, significantly shaping it and allowing for healthy growth and maturation. Therefore I thank: Angela, Sofia, Clara, Gabriela, Giorgia, Emma, Roberta, Francesca, Giacomo, Tommaso, Michele, and Pietro. I need also to thank Lorenzo, my brother, who has grown up with and togheter we shared a lot of moments.

During the universty I had the opportunity of knowing

A Appendix

A.1 Fractional slot concentrated winding factor

A.1.1 Winding factor table for three-phase winding system

$Q\backslash 2p$	2	4	6	8	10	12	14	16	18	20	22	24	26	28	30
3	0.866	0.866	*	0.866	0.866	*	0.866	0.866	*	0.866	0.866	*	0.866	0.866	*
6	-	0.866	*	0.866	1.7321	*	1.7321	0.866	*	0.866	1.7321	*	1.7321	0.866	*
9	-	0.6169	0.866	0.9452	0.9452	0.866	0.6169	0.4924	*	0.4924	0.6169	0.866	0.9452	0.9452	0.866
12	-	-	*	0.866	0.933	*	0.933	0.866	*	1.7321	0.5	*	0.5	1.7321	*
15	-	-	*	0.7109	0.866	*	0.9514	0.9514	*	0.866	0.7109	*	0.4864	0.2486	*
18	-	-	-	0.6169	0.9452	0.866	1.1595	0.9452	*	0.9452	1.1595	0.866	0.9452	0.6169	1.7321
21	-	-	-	0.5384	0.6501	*	0.866	0.8897	*	0.9531	0.9531	*	0.8897	0.866	*
24	-	-	-	-	0.583	*	0.7598	0.866	*	0.933	0.9495	*	0.9495	0.933	*
27	-	-	-	-	0.525	0.6169	0.695	0.7664	0.866	0.8773	0.9153	0.9452	0.9539	0.9539	0.9452
30	-	-	-	-	-	*	0.7525	0.7109	*	0.866	1.0274	*	1.1001	0.9514	*

Table A.1 – Winding factor $k_{w,p}$ for three-phase system with double-layer

$Q\backslash 2p$	2	4	6	8	10	12	14	16	18	20	22	24	26	28	30
3	*	*	*	*	*	*	*	*	*	*	*	*	*	*	*
6	-	*	*	*	*	*	*	*	*	*	*	*	*	*	*
9	-	0.5343	*	0.8186	0.8186	*	0.5343	*	*	*	0.5343	*	0.8186	0.8186	*
12	-	-	*	*	0.9012	*	0.9012	*	*	*	0.9659	*	0.9659	*	*
15	-	-	*	0.6762	*	*	0.9049	0.9049	*	*	0.6762	*	*	0.7567	*
18	-	-	-	0.5343	0.9309	*	*	0.8186	*	0.8186	*	*	0.9309	0.5343	*
21	-	-	-	0.5249	0.6338	*	*	0.8674	*	0.9293	0.9293	*	0.8674	*	*
24	-	-	-	-	0.578	*	0.7533	*	*	0.9012	0.9413	*	0.9413	0.9012	*
27	-	-	-	-	0.5171	0.5343	0.6844	0.7548	*	0.864	0.9014	0.8186	0.9394	0.9394	0.8186
30	-	-	-	-	-	*	0.7484	0.6762	*	*	*	*	*	0.9049	*

Table A.2 – Winding factor $k_{w,p}$ for three-phase system with 4-layer

A.1.2 Winding factor table for five-phase winding system

$Q\backslash 2p$	2	4	6	8	10	12	14	16	18	20	22	24	26	28
5	0.5878	0.9511	0.9511	0.5878	*	0.5878	0.9511	0.9511	0.5878	*	0.5878	0.9511	0.9511	0.5878
10	-	0.5878	*	0.9511	*	0.9511	*	0.5878	*	*	*	0.5878	*	0.9511
15	-	0.4008	0.5878	0.7323	*	0.9511	0.98	0.98	0.9511	*	0.7323	0.5878	0.4008	0.2561
20	-	-	0.4484	0.5878	*	*	0.88	0.9511	0.9755	*	0.9755	0.9511	0.88	*
25	-	-	0.3623	0.4742	0.5878	0.6738	0.7584	0.8311	0.8906	0.9511	0.9668	0.9823	0.9823	0.9668

Table A.3 – Winding factor $k_{w,p}$ for five-phase system with double-layer

$Q\backslash 2p$	2	4	6	8	10	12	14	16	18	20	22	24	26	28
5	0.9511	0.5878	0.5878	0.9511	*	0.9511	0.5878	0.5878	0.9511	*	0.9511	0.5878	0.5878	0.9511
10	-	0.9511	0.3633	0.5878	*	0.5878	0.3633	0.9511	*	*	*	0.9511	0.3633	0.5878
15	-	0.83	0.9511	0.5129	*	0.5878	0.83	0.83	0.5878	*	0.5129	0.9511	0.83	0.6412
20	-	-	0.88	0.9511	*	0.3633	0.1394	0.5878	0.7939	*	0.7939	0.5878	0.1394	0.3633
25	-	-	0.7813	0.8618	0.9511	0.6653	0.416	0.1082	0.2147	0.5878	0.7291	0.8482	0.8482	0.7291

Table A.4 – Winding factor $k_{w,3p}$ for five-phase system with double-layer

$Q\backslash 2p$	2	4	6	8	10	12	14	16	18	20	22	24	26	28
5	*	*	*	*	*	*	*	*	*	*	*	*	*	*
10	-	*	*	*	*	*	*	*	*	*	*	*	*	*
15	-	0.3812	*	0.6965	*	*	0.9321	0.9321	*	*	0.6965	*	0.3812	0.7794
20	-	-	0.4429	*	*	*	0.8692	*	0.9635	*	0.9635	*	0.8692	*
25	-	-	0.3559	0.4658	*	0.6619	0.745	0.8163	0.8748	*	0.9497	0.9649	0.9649	0.9497

Table A.5 – Winding factor $k_{w,p}$ for five-phase system with 4-layer

$Q\backslash 2p$	2	4	6	8	10	12	14	16	18	20	22	24	26	28
5	*	*	*	*	*	*	*	*	*	*	*	*	*	*
10	-	*	*	*	*	*	*	*	*	*	*	*	*	*
15	-	0.4878	*	0.3015	*	*	0.4878	0.4878	*	*	0.3015	*	0.4878	*
20	-	-	0.7841	*	*	*	0.1242	*	0.7074	*	0.7074	*	0.1242	*
25	-	-	0.6597	0.7276	*	0.5618	0.3512	0.0914	0.1813	*	0.6156	0.7162	0.7162	0.6156

Table A.6 – Winding factor $k_{w,3p}$ for five-phase system with 4-layer

A.1.3 Winding factor table for seven-phase winding system

$Q\backslash 2p$	2	4	6	8	10	12	14	16	18	20	22	24	26	28	30
7	0.4339	0.7818	0.9749	0.9749	0.7818	0.4339	*	0.4339	0.7818	0.9749	0.9749	0.7818	0.4339	*	0.4339
14	-	0.4339	*	0.7818	0.901	0.9749	*	0.9749	0.901	0.7818	0.6235	0.4339	0.3807	*	0.2225
21	-	0.2926	0.4339	0.5591	0.6751	0.7818	*	0.9239	0.9749	0.9898	0.9898	0.9749	0.9239	*	0.7818
28	-	-	0.3282	0.4339	0.5287	*	*	0.7818	0.8414	0.901	0.9379	0.9749	0.9875	*	0.9875

Table A.7 – Winding factor $k_{w,p}$ for seven-phase system with double-layer

$Q\backslash 2p$	2	4	6	8	10	12	14	16	18	20	22	24	26	28	30
7	0.9749	0.4339	0.7818	0.7818	0.4339	0.9749	*	0.9749	0.4339	0.7818	0.7818	0.4339	0.9749	*	0.9749
14	-	0.9749	*	0.4339	0.2225	0.7818	*	0.7818	0.2225	0.4339	0.901	0.9749	0.8827	*	0.6235
21	-	0.7302	0.9749	0.9106	0.7302	0.4339	*	0.4052	0.7818	0.9106	0.9106	0.7818	0.4052	*	0.4339
28	-	-	0.7992	0.9749	0.9379	*	*	0.4339	0.1057	0.2225	0.5022	0.7818	0.8909	*	0.8909

Table A.8 – Winding factor $k_{w,3p}$ for seven-phase system with double-layer

$Q\backslash 2p$	2	4	6	8	10	12	14	16	18	20	22	24	26	28	30
7	0.7818	0.9749	0.4339	0.4339	0.9749	0.7818	*	0.7818	0.9749	0.4339	0.4339	0.9749	0.7818	*	0.7818
14	-	0.7818	0.1931	0.9749	0.6235	0.4339	*	0.4339	0.6235	0.9749	0.2225	0.7818	0.832	*	0.901
21	-	0.8197	0.7818	0.1225	0.4631	0.9749	*	0.2423	0.4339	0.7652	0.7652	0.4339	0.2423	*	0.9749
28	-	-	0.8414	0.7818	0.2797	0.1931	*	0.9749	0.7992	0.6235	0.0948	0.4339	0.7169	*	0.7169

Table A.9 – Winding factor $k_{w,5p}$ for seven-phase system with double-layer

$Q\backslash 2p$	2	4	6	8	10	12	14	16	18	20	22	24	26	28	30
7	*	*	*	*	*	*	*	*	*	*	*	*	*	*	*
14	-	*	*	*	*	*	*	*	*	*	*	*	*	*	*
21	-	0.2852	*	0.5451	0.6582	*	*	0.9008	*	0.965	0.965	*	0.9008	*	*
28	-	-	0.3261	*	0.5254	*	*	*	0.8361	*	0.9321	*	0.9813	*	0.9813

Table A.10 – Winding factor $k_{w,p}$ for seven-phase system with 4-layer

$Q\backslash 2p$	2	4	6	8	10	12	14	16	18	20	22	24	26	28	30
7	*	*	*	*	*	*	*	*	*	*	*	*	*	*	*
14	-	*	*	*	*	*	*	*	*	*	*	*	*	*	*
21	-	0.5709	*	0.7119	0.5709	*	*	0.3168	*	0.7119	0.7119	*	0.3168	*	*
28	-	-	0.7544	*	0.8853	*	*	*	0.0998	*	0.474	*	0.8409	*	0.8409

Table A.11 – Winding factor $k_{w,3p}$ for seven-phase system with 4-layer

$Q\backslash 2p$	2	4	6	8	10	12	14	16	18	20	22	24	26	28	30
7	*	*	*	*	*	*	*	*	*	*	*	*	*	*	*
14	-	*	*	*	*	*	*	*	*	*	*	*	*	*	*
21	-	0.3557	*	0.0532	0.2009	*	*	0.1051	*	0.332	0.332	*	0.1051	*	*
28	-	-	0.7124	*	0.2368	*	*	*	0.6767	*	0.0803	*	0.6071	*	0.6071

Table A.12 – Winding factor $k_{w,5p}$ for seven-phase system with 4-layer

A.2 Sintered neodymium magnets

The sintered neodymium magnets used for the permanent magnet are of the N42H grade. The characteristics of this neodymium magnet have been obtained from the extensive catalog offered on the website of the company *Arnold Magnetic Technologies Corporation*. The datasheet of the N42H magnet is provided on the following page.

N42H

Sintered Neodymium-Iron-Boron Magnets

These are also referred to as "Neo" or NdFeB magnets. They offer a combination of high magnetic output at moderate cost. Please contact Arnold for additional grade information and recommendations for protective coating. Assemblies using these magnets can also be provided.

	Characteristic	Units	min.	nominal	max.
Magnetic Properties	**Br**, Residual Induction	Gauss	12,800	13,000	13,200
		mT	1280	1300	1320
	H$_{cB}$, Coercivity	Oersteds	12,000	12,300	12,600
		kA/m	955	979	1003
	H$_{cJ}$, Intrinsic Coercivity	Oersteds	17,000		
		kA/m	1,353		
	BHmax, Maximum Energy Product	MGOe	40	42	43
		kJ/m^3	318	330	342

	Characteristic	Units	C //	C ⊥
Thermal Properties	Reversible Temperature Coefficients [(1)]			
	of Induction, α(Br)	%/ºC	-0.12	
	of Coercivity, α(Hcj)	%/ºC	-0.57	
	Coefficient of Thermal Expansion [(2)]	ΔL/L per ºCx10^{-6}	7	-1
	Thermal Conductivity	kcal/mhrºC	5.3	5.8
	Specific Heat [(3)]	cal/gºC	0.11	
	Curie Temperature, Tc	ºC	310	
Other Properties	Flexural Strength	psi	41,300	
		MPa	285	
	Density	g/cm^3	7.6	
	Hardness, Vickers	Hv	620	
	Electrical Resistivity, ρ	μΩ • cm	150 // 130 ⊥	

Notes:
(1) Coefficients measured between 20 and 120 ºC
(2) Between 20 and 200 ºC. Values are typical and can vary.
(3) Between 20 and 140 ºC

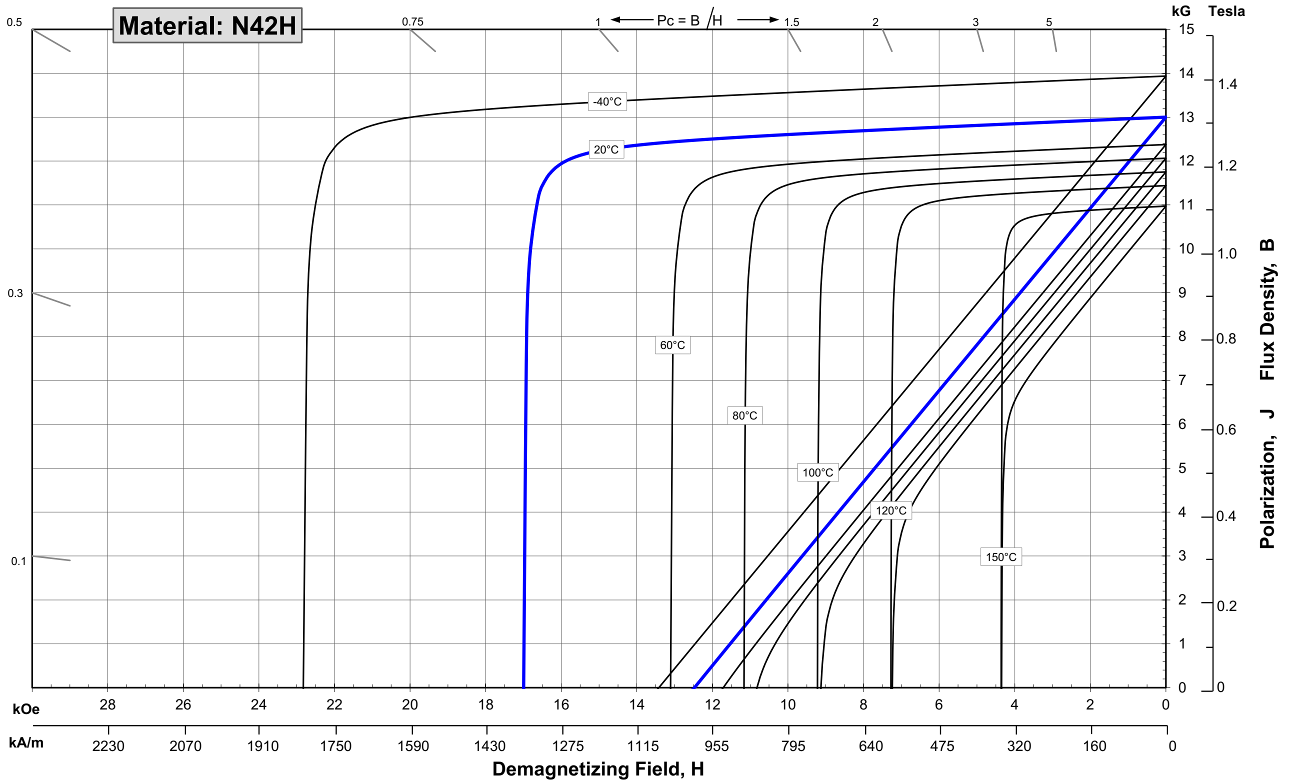

1 kA/m = 12.566 Oe 1 kOe = 79.577 kA/m

Notes The material data and demagnetization curves shown above represent typical properties that may vary due to product shape and size.
Demagnetization curves show nominal Br and minimum Hci.
Magnets can be supplied thermally stabilized or magnetically calibrated to customer specifications.
Additional grades are available. Please contact the factory for information.

Bibliography

[1] Abdel-Khalik, A.: “Five-Phase Modular External Rotor PM Machines with Different Rotor Poles: A Comparative Simulation Study”. In: *Modelling and Simulation in Engineering* 2012 (Sept. 2012). DOI: `10.1155/2012/487203`.

[2] Abdel-Khalik, A. S.; Ahmed, S.; Massoud, A. M.: “Low Space Harmonics Cancelation in Double-Layer Fractional Slot Winding Using Dual Multiphase Winding”. In: *IEEE Transactions on Magnetics* 51.5 (2015), pp. 1–10. DOI: `10.1109/TMAG.2014.2364988`.

[3] Akita, H.; Nakahara, Y.; Miyake, N., ; et al.: “New core structure and manufacturing method for high efficiency of permanent magnet motors”. In: *38th IAS Annual Meeting on Conference Record of the Industry Applications Conference, 2003.* Vol. 1. 2003, 367–372 vol.1. DOI: `10.1109/IAS.2003.1257527`.

[4] Alberti, L.; Bianchi, N.: “Experimental Tests of Dual Three-Phase Induction Motor Under Faulty Operating Condition”. In: *IEEE Transactions on Industrial Electronics - IEEE TRANS IND ELECTRON* 59 (May 2012), pp. 2041–2048. DOI: `10.1109/TIE.2011.2171175`.

[5] Alberti, L.; Bianchi, N.: “Theory and design of fractional-slot multilayer windings”. In: *2011 IEEE Energy Conversion Congress and Exposition.* 2011, pp. 3112–3119. DOI: `10.1109/ECCE.2011.6064188`.

[6] Barcaro, M.; Bianchi, N.; Magnussen, F.: “Faulty Operations of a PM Fractional-Slot Machine With a Dual Three-Phase Winding”. In: *Industrial Electronics, IEEE Transactions on* 58 (Oct. 2011), pp. 3825–3832. DOI: `10.1109/TIE.2010.2087300`.

[7] Barrero, F.; Duran, M. J.: “Recent Advances in the Design, Modeling, and Control of Multiphase Machines—Part I”. In: *IEEE Transactions on Industrial Electronics* 63.1 (2016), pp. 449–458. DOI: `10.1109/TIE.2015.2447733`.

[8] Bianchi, N.; Bolognani, S.: “Design techniques for reducing the cogging torque in surface-mounted PM motors”. In: *IEEE Transactions on Industry Applications* 38.5 (2002), pp. 1259–1265. DOI: `10.1109/TIA.2002.802989`.

[9] Bianchi, N.; Bolognani, S.: *Metodologie di progettazione delle macchine elettriche.* CLEUP, 2001. ISBN: 9788871785295. URL: `https://books.google.de/books?id=lgu6PQAACAAJ`.

[10] Bianchi, N.; Bolognani, S.; Pre, M., ; et al.: “Design considerations for fractional-slot winding configurations of synchronous machines”. In: *IEEE Transactions on Industry Applications* 42.4 (2006), pp. 997–1006. DOI: `10.1109/TIA.2006.876070`.

[11] Bianchi, N.: *Electrical machine analysis using finite elements.* en. Power Electronics and Applications Series. Boca Raton, FL: CRC Press, June 2005.

[12] Bianchi, N.: *Progettazione Macchine Rotanti.* University Lecture. 2020.

[13] Bianchi, N.; Bolognani, S.; Dai Pre, M.: “Strategies for the Fault-Tolerant Current Control of a Five-Phase Permanent-Magnet Motor”. In: *IEEE Transactions on Industry Applications* 43.4 (2007), pp. 960–970. DOI: `10.1109/TIA.2007.900445`.

[14] Binder, A.: *Elektrische Maschinen und Antriebe: Grundlagen, Betriebsverhalten.* Springer-Lehrbuch. Springer Berlin Heidelberg, 2012. ISBN: 9783540718505. URL: `https://books.google.de/books?id=CtRgiWYqnpsC`.

[15] Cao, W.; Mecrow, B. C.; Atkinson, G. J., ; et al.: “Overview of Electric Motor Technologies Used for More Electric Aircraft (MEA)”. In: *IEEE Transactions on Industrial Electronics* 59.9 (2012), pp. 3523–3531. DOI: `10.1109/TIE.2011.2165453`.

[16] Chen, C.; Zhou, H.; Wang, G., ; et al.: “Unified Decoupling Vector Control of Five-Phase Permanent-Magnet Motor With Double-Phase Faults”. In: *IEEE Access* 8 (2020), pp. 152646–152658. DOI: `10.1109/ACCESS.2020.3017541`.

[17] Chen, Y.; Liu, B.: “Design and Analysis of a Five-Phase Fault-Tolerant Permanent Magnet Synchronous Motor for Aerospace Starter-Generator System”. In: *IEEE Access* 7 (2019), pp. 135040–135049. DOI: `10.1109/ACCESS.2019.2941447`.

[18] Cistelecan, M. V.; Ferreira, F. J. T. E.; Popescu, M.: “Three phase tooth-concentrated multiple-layer fractional windings with low space harmonic content”. In: *2010 IEEE Energy Conversion Congress and Exposition.* 2010, pp. 1399–1405. DOI: `10.1109/ECCE.2010.5618267`.

[19] Dlala, E.: “Comparison of Models for Estimating Magnetic Core Losses in Electrical Machines Using the Finite-Element Method”. In: *IEEE Transactions on Magnetics* 45.2 (2009), pp. 716–725. DOI: `10.1109/TMAG.2008.2009878`.

[20] Duran, M. J.; Barrero, F.: “Recent Advances in the Design, Modeling, and Control of Multiphase Machines—Part II”. In: *IEEE Transactions on Industrial Electronics* 63.1 (2016), pp. 459–468. DOI: `10.1109/TIE.2015.2448211`.

[21] Dwari, S.; Parsa, L.: “Fault-Tolerant Control of Five-Phase Permanent-Magnet Motors With Trapezoidal Back EMF”. In: *IEEE Transactions on Industrial Electronics* 58.2 (2011), pp. 476–485. DOI: `10.1109/TIE.2010.2045322`.

[22] Farshadnia, M.: *Advanced Theory of Fractional-Slot Concentrated-Wound Permanent Magnet Synchronous Machines.* Springer Theses. Springer Nature Singapore, 2018. ISBN: 9789811087080. URL: `https://books.google.de/books?id=qH1TDwAAQBAJ`.

[23] Farshadnia, M.; Dutta, R.; Fletcher, J. E., ; et al.: “Analysis of MMF and back-EMF waveforms for fractional-slot concentrated-wound permanent magnet machines”. In: *2014 International Conference on Electrical Machines (ICEM).* 2014, pp. 1976–1982. DOI: `10.1109/ICELMACH.2014.6960455`.

[24] Fireţeanu, V.; Constantin, A.-I.; Dumitru, C.: “Finite Element Analysis of the Performances of the 3-Phase, 5-Phase, 7-Phase and 9-Phase Squirrel-Cage Induction Motors”. In: *2021 12th International Symposium on Advanced Topics in Electrical Engineering (ATEE).* 2021, pp. 1–6. DOI: `10.1109/ATEE52255.2021.9425068`.

[25] Fireţeanu, V.; Dumitru, C.: “Finite Element Analysis of Multiphase Permanent Magnet Synchronous Motors with the Same Stators of Analogue 3-phase, 5-phase, 7-phase and 9-phase Induction Motors”. In: *2021 International Conference on Applied and Theoretical Electricity (ICATE).* 2021, pp. 1–6. DOI: `10.1109/ICATE49685.2021.9465021`.

[26] Fornasiero, E.; Alberti, L.; Bianchi, N., ; et al.: “Considerations on selecting fractional—slot windings”. In: *2010 IEEE Energy Conversion Congress and Exposition.* 2010, pp. 1376–1383. DOI: `10.1109/ECCE.2010.5618269`.

[27] Fornasiero, E.; Bianchi, N.; Bolognani, S.: “Slot Harmonic Impact on Rotor Losses in Fractional-Slot Permanent-Magnet Machines”. In: *IEEE Transactions on Industrial Electronics* 59.6 (2012), pp. 2557–2564. DOI: `10.1109/TIE.2011.2168794`.

[28] Fu, J.-R.; Lipo, T.: “Disturbance-free operation of a multiphase current-regulated motor drive with an opened phase”. In: *IEEE Transactions on Industry Applications* 30.5 (1994), pp. 1267–1274. DOI: `10.1109/28.315238`.

[29] Huang, J.; Zheng, P.; Sui, Y., ; et al.: “Third Harmonic Current Injection in Different Operating Stages of Five-Phase PMSM With Hybrid Single/Double Layer Fractional-Slot Concentrated Winding”. In: *IEEE Access* 9 (2021), pp. 15670–15685. DOI: `10.1109/ACCESS.2021.3052558`.

[30] Huth, G.: “Permanent-magnet-excited AC servo motors in tooth-coil technology”. In: *IEEE Transactions on Energy Conversion* 20.2 (2005), pp. 300–307. DOI: `10.1109/TEC.2005.845537`.

[31] Ishak, D.; Zhu, Z.; Howe, D.: “Eddy-current loss in the rotor magnets of permanent-magnet brushless machines having a fractional number of slots per pole”. In: *IEEE Transactions on Magnetics* 41.9 (2005), pp. 2462–2469. DOI: `10.1109/TMAG.2005.854337`.

[32] Janaszek, M.: “Extended Clarke Transformation for n-phase systems”. In: *Proceedings of Electrotechnical Institute* 63 (Dec. 2016), pp. 5–26. DOI: `10.5604/01.3001.0009.4333`.

[33] Leonhard, W.: *Control of Electrical Drives.* Springer Berlin Heidelberg, 2012. ISBN: 9783642976469. URL: `https://books.google.de/books?id=O_XvCAAAQBAJ`.

[34] Levi, E.: “Multiphase Electric Machines for Variable-Speed Applications”. In: *IEEE Transactions on Industrial Electronics* 55.5 (2008), pp. 1893–1909. DOI: `10.1109/TIE.2008.918488`.

[35] Li, Q.; Fan, T.; Wen, X., ; et al.: “A novel multi-layer winding design method for Fractional-Slot Concentrated-Windings Permanent Magnet Machine”. In: *2014 IEEE Conference and Expo Transportation Electrification Asia-Pacific (ITEC Asia-Pacific).* 2014, pp. 1–5. DOI: `10.1109/ITEC-AP.2014.6940615`.

[36] Magnussen, F.; Sadarangani, C.: “Winding factors and Joule losses of permanent magnet machines with concentrated windings”. In: *IEEE International Electric Machines and Drives Conference, 2003. IEMDC’03.* Vol. 1. 2003, 333–339 vol.1. DOI: `10.1109/IEMDC.2003.1211284`.

[37] Meeker, D.: *Rotating Losses in a Surface Mount Permanent Magnet Motor.* Oct. 2017. URL: `https://www.femm.info/wiki/SPMLoss`.

[38] Müller, G.: *Berechnung Elektrischer Maschinen.* Elektrische Maschine. Wiley-VCH Verlag, 2007. URL: `https://books.google.de/books?id=zGSJrgEACAAJ`.

[39] Ouamara, D.; Dubas, F.; Randi, S., ; et al.: “General calculation of winding factor for multi-phase/-layer electrical machines irrespective of poles number”. In: *Acta Polytechnica* 59 (May 2019). DOI: `10.14311/AP.2019.59.0153`.

[40] Parsa, L.; Toliyat, H.: “Fault-tolerant five-phase permanent magnet motor drives”. In: *Conference Record of the 2004 IEEE Industry Applications Conference, 2004. 39th IAS Annual Meeting.* Vol. 2. 2004, 1048–1054 vol.2. DOI: `10.1109/IAS.2004.1348542`.

[41] Parsa, L.; Toliyat, H.: “Five-phase permanent-magnet motor drives”. In: *IEEE Transactions on Industry Applications* 41.1 (2005), pp. 30–37. DOI: `10.1109/TIA.2004.841021`.

[42] Parsa, L.; Toliyat, H. A.; Goodarzi, A.: “Five-Phase Interior Permanent-Magnet Motors With Low Torque Pulsation”. In: *IEEE Transactions on Industry Applications* 43.1 (2007), pp. 40–46. DOI: `10.1109/TIA.2006.887235`.

[43] Polinder, H.; Hoeijmakers, M.; Scuotto, M.: “Eddy-Current Losses in the Solid Back-Iron of PM Machines for different Concentrated Fractional Pitch Windings”. In: *2007 IEEE International Electric Machines and Drives Conference.* Vol. 1. 2007, pp. 652–657. DOI: `10.1109/IEMDC.2007.382744`.

[44] Ruoho, S.; Haavisto, M.; Takala, E., ; et al.: “Temperature Dependence of Resistivity of Sintered Rare-Earth Permanent-Magnet Materials”. In: *IEEE Transactions on Magnetics* 46.1 (2010), pp. 15–20. DOI: `10.1109/TMAG.2009.2027815`.

[45] Steinmetz, C. P.: “On the law of hysteresis”. In: *Trans. Am. Inst. Electr. Eng.* IX.1 (Jan. 1892), pp. 1–64.

[46] Tang, N.; Brown, I. P.: “Framework and Solution Techniques for Suppressing Electric Machine Winding MMF Space Harmonics by Varying Slot Distribution and Coil Turns”. In: *IEEE Transactions on Magnetics* 54.5 (2018), pp. 1–12. DOI: `10.1109/TMAG.2018.2804897`.

[47] Wang, J.; Qu, R.; Zhou, L.: “Dual-Rotor Multiphase Permanent Magnet Machine With Harmonic Injection to Enhance Torque Density”. In: *IEEE Transactions on Applied Superconductivity* 22.3 (2012), pp. 5202204–5202204. DOI: `10.1109/TASC.2011.2179399`.

[48] Wang, J.; Zhou, L.; Qu, R.: “Harmonic current effect on torque density of a multiphase permanent magnet machine”. In: *2011 International Conference on Electrical Machines and Systems.* 2011, pp. 1–6. DOI: `10.1109/ICEMS.2011.6073674`.

[49] Williamson, S.; Smith, S.: “Pulsating torque and losses in multiphase induction machines”. In: *Conference Record of the 2001 IEEE Industry Applications Conference. 36th IAS Annual Meeting (Cat. No.01CH37248).* Vol. 2. 2001, 1155–1162 vol.2. DOI: `10.1109/IAS.2001.955635`.

[50] Zarri, L.; Mengoni, M.; Gritli, Y., ; et al.: “Detection and Localization of Stator Resistance Dissymmetry Based on Multiple Reference Frame Controllers in Multiphase Induction Motor Drives”. In: *IEEE Trans. Ind. Electron.* 60.8 (2013), pp. 3506–3518. DOI: `10.1109/TIE.2012.2235393`. URL: `https://doi.org/10.1109/TIE.2012.2235393`.

[51] Zhou, H.; Zhao, W.; Liu, G., ; et al.: “Remedial Field-Oriented Control of Five-Phase Fault-Tolerant Permanent-Magnet Motor by Using Reduced-Order Transformation Matrices”. In: *IEEE Transactions on Industrial Electronics* 64.1 (2017), pp. 169–178. DOI: `10.1109/TIE.2016.2599501`.

[52] Zhu, Z.-Q.; Zheng, Y.; Liu, Y., ; et al.: “Effect of End-Winding on Electromagnetic Performance of Fractional Slot and Vernier PM Machines With Different Slot/Pole Number Combinations and Winding Configurations”. In: *IEEE Access* 10 (2022), pp. 49934–49955. DOI: `10.1109/ACCESS.2022.3172323`.